EUROPEAN COMMISSION
5th EURATOM FRAMEWORK PROGRAMME 1998-2002
KEY ACTION : NUCLEAR FISSION

RESEAL-II

A large scale in situ demonstration test for repository sealing In an argillaceous host rock – phase II

CONTRACT N° FIKW-CT-2000-00010

Final report on laboratory tests (WP1)

Edited by: M.V. Villar (CIEMAT) from contributions of:

CEA: C. Imbert, P. Billaud, G. Touzé
CIEMAT: M.V. Villar, M. García-Gutiérrez, M. Mingarro
SCK•CEN: M. Van Geet, N. Maes, M. Aertsens, G. Volckaert

Reporting Period:
September 2000 – May 2005

Dissemination level :
PU: public
RE: restricted to a group specified by the partners of the RESEAL-II project
CO: confidential, only for partners of the RESEAL-II project
M: Management, **S/T**: Scientific/Technical reports, **MT**: Mid-term, **nnn** = number

SCKCEN-ER-1

Table of contents

1 INTRODUCTION

The RESEAL project aims at demonstrating the sealing of a borehole and a shaft in plastic clay on a representative scale. The backfilling and sealing of shafts and galleries is an important part of underground repository designs. Any opening created during the repository construction is a potential preferential pathway for water, gas and radionuclides migration, and has to be effectively sealed afterwards.

Bentonite is widely studied as backfill and sealing material in geological repositories for radioactive waste because of its low permeability and large swelling capacity. The main objective of the project is to demonstrate that a seal of bentonite avoids preferential migration of water, gas and radionuclides along the seal/host rock interface and through the excavation disturbed zone. The project started in 1996 in the frame of the EC specific RTD programme on "Nuclear Fission Safety". It has included the selection and characterisation of sealing materials, the development of the seal installation technique, the monitoring of the horizontal borehole and the shaft sealing tests performed at the HADES Underground Research Facility (URF) in Mol (Belgium) and the modelling of the main processes and phenomena observed during the tests. The first phase of the project ended in October 1999 with the installation of the shaft seal. The second phase of the project (RESEAL II), mainly focussed on the shaft sealing test, is a joint project between SCK•CEN (co-ordinator), ANDRA, CEA, CIEMAT and UPC. The project is financially supported by EC and NIRAS/ONDRAF.

The experimental shaft has a diameter of about 1.4 m and has been filled up with a pellets/powder mixture of FoCa bentonite (Figure 1-1). This powder/pellets mixture has the advantage that it can be easily applied to backfill irregularly shaped volumes and that it is rather cheap to produce in comparison to compacted blocks. It also requires less compaction effort to achieve a given average dry density because of the very dense pellets of the mixture. The pellets have a size of approximately 25 x 25 x 15 mm and a dry density close to 2 g/cm^3. To obtain a high-density granular backfill material, the pellets are mixed with powder of the same clay. A 50/50 weight percent pellets/powder proportion was selected during the first phase of the project. This proportion has been chosen to avoid segregation during installation in the shaft and favour a homogeneous hydration and redistribution of density, although this particular proportion does not grant the highest density (Imbert *et al.* 1999). The first 60 cm of the seal have been compacted by using vibro-compaction techniques to increase the density of the mixture. This resulted in a dry density of 1.6 g/cm^3. The compaction was stopped just below the first instrumented level. From this level the sealing material was installed without further compaction in order to avoid damage to the instruments. The dry density of the material thus installed is 1.4 g/cm^3. Artificial hydration of the seal started in May 2000. Once the seal is saturated, water and gas sealing capacity tests will be carried out, as well as injection of radioactive tracers.

On the other hand, a tracer injection test through the plug (pre-compacted high-density FoCa bentonite blocks) of the borehole sealing test, installed during RESEAL I, is being performed in order to check if there are preferential pathways for radionuclide migration in the borehole seal. The experimental results will allow validating the tracer diffusion models.

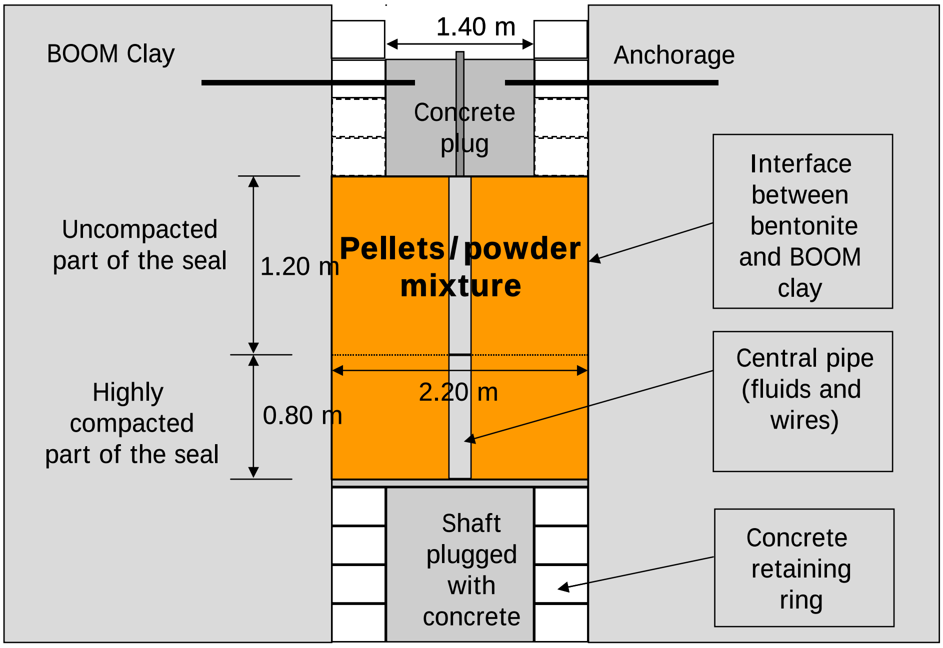

Figure 1-1: Schematic representation of the shaft sealing test at the HADES URF.

The laboratory work to characterise the shaft pellets/powder mixture seal has been carried out by three organisations: CEA (France), SCK·CEN (Belgium) and CIEMAT (Spain). It has been divided in two groups of activities, those aimed at the study of the hydro-mechanical properties of the sealing material, and the activities related to the determination of the migration parameters. To analyse the hydration mechanisms of the pellets/powder mixtures and their coupling with the mechanical behaviour, different infiltration tests with measurement of the swelling pressure have been performed. In addition, since the migration of radionuclides in clays is controlled by diffusion, the determination of radionuclides diffusion coefficients, as well as of their accessible porosity, has been undertaken.

2 MATERIAL

The backfill material in the experimental shaft of the HADES URF test is a mixture of pellets and powder of FoCa clay, which is a Ca-bentonite from the Paris Basin (Fourges-Cahaignes, France). For the RESEAL II Project, a batch of bentonite was delivered as a powder with water content of five percent, henceforth referenced as FoCa-RESEAL. Half of this batch was transformed into pellets by the company Sahut-Conreur at Raismes (France). The dimensions of the pellets are 25x25x12 mm and their average dry density is 1.89 g/cm^3.

The proportion of pellets and powder in the mixture is 50/50 on a dry weight basis, as selected from preliminary tests performed during RESEAL I (Volckaert *et al.* 2000). Both the pellets and the powder were manufactured from the same clay batch, and, at the laboratory, they have water contents of 5 and 6 percent, respectively. The same material has been used for the diffusion tests described below, and it will be called hereafter “RESEAL II mixture”. However, for most of the hydro-mechanical tests, the powder used came from a different batch, called FoCa7, with which CEA had extensively worked in the past. The coloration of the FoCa7 is slightly different from that of the RESEAL II batch, and it was used because it could be useful to have different colorations for the identification of pellets and powder after the hydro-mechanical tests. The water content of the FoCa7 is 12 percent. Later on it was decided to check the influence on the hydro-mechanical behaviour of the water content of the pellets and the powder in the mixture and for that, hydro-mechanical tests have been also performed with the RESEAL II mixture.

The major component of FoCa bentonite is an inter-stratified clay of 50 % beidellite and 50 % kaolinite. It contains also quartz, goethite, hematite, calcite and gypsum. The major exchangeable cations are Ca^{2+} (73.1 meq/100g), Mg^{2+} (6.5 meq/100g), Na^{+} (3.6 meq/100g) and K^{+} (0.8 meq/100g) (Volckaert *et al*. 2000). The density of the solid particles is 2.67 g/cm^3.

The swelling pressure of FoCa clay compacted at different dry densities was measured by CEA during RESEAL I, an exponential relation between both variables being found (Volckaert *et al*. 2000). It was also demonstrated that the swelling pressure of compacted powder was equivalent to the swelling pressure of a pellets/powder mixture of the same dry density. However, the swelling pressure measured in the laboratory tests performed during phase II and in the *in situ* test at the HADES facility in Mol, were lower than expected according to the relation determined formerly. For this reason, new determinations were carried out. CEA performed measurements on FoCa RESEAL compacted at dry density higher than 1.7 g/cm^3. The tests were performed in swelling cells with specimens of 20 mm nominal height saturated with deionised, deaerated water by both faces under a 1-m water column (Imbert *et al*. 2004). CIEMAT carried out tests in oedometers on specimens of 12 mm nominal height flooded with deionised water by the bottom surface. The dry density of the specimens was lower than 1.7 g/cm^3, and both the FoCa RESEAL and the FoCa7 used in the hydro-mechanical tests were tested. A summary of the results obtained is given in Table 2-1, in which it can be observed that the final degrees of saturation are higher than 100 percent. This is because they were computed considering the density of the water as 1.00 g/cm^3, which was shown to be untrue for high plasticity materials (Villar 2000, 2002, Marcial 2003, Villar & Lloret 2004). The swelling pressure values are plotted in Figure 2-1.

According to the tests performed in CIEMAT, the swelling pressure of FoCa7 and FoCa RESEAL is quite the same. In both cases the values are much lower than those determined previously at CEA laboratories for FoCa7. With respect to the FoCa RESEAL batch, the results obtained by the two laboratories for different density intervals are coherent. Hence, a joint correlation relating final dry density (ρ_d, g/cm^3) and swelling pressure upon saturation (P_s, MPa) has been obtained and is plotted in the Figure:

$$P_s = 0.0018\ \rho_d^{\ 15.204} \qquad [1.]$$

Table 2-1: Swelling pressure tests with FoCa clay powder (ρ_d: dry density, w: gravimetric water conten, P_s: swelling pressure, S_r: degree of saturation).

Sample/ laboratory	**Initial ρ_d (g/cm^3)**	**Initial *w* (%)**	**P_s (MPa)**	**Final *w* (%)**	**Final ρ_d (g/cm^3)**	**Final S_r (%)**
RESEAL/CIEMAT	1.32	8.6	0.1	42.4	1.32	111
RESEAL/CIEMAT	1.34	9.6	0.2	40.5	1.35	110
RESEAL/CIEMAT	1.42	8.3	0.5	36.3	1.42	111
RESEAL/CIEMAT	1.46	8.4	0.5	34.7	1.47	113
RESEAL/CIEMAT	1.51	9.2	1.3	29.7	1.51	103
RESEAL/CIEMAT	1.55	9.3	1.2	28.4	1.55	104
RESEAL/CIEMAT	1.61	9.7	2.8	26.9	1.60	107
RESEAL/CIEMAT	1.63	10.4	2.0	26.5	1.62	110
FoCa7/CIEMAT	1.31	10.6	0.2	39.4	1.32	103
FoCa7/CIEMAT	1.41	11.4	0.4	35.7	1.41	107
FoCa7/CIEMAT	1.50	11.5	0.7	31.7	1.50	109
FoCa7/CIEMAT	1.54	12.1	1.2	31.1	1.54	113
FoCa7/CIEMAT	1.61	11.5	3.4	26.8	1.62	110
FoCa7/CEA	1.73	4.8	7.3		1.72	
FoCa7/CEA	1.88	4.8	21.5		1.85	
FoCa7/CEA	1.98	4.8	40.4		1.94	
FoCa7/CEA	2.03	4.8	53.8		1.98	

The pore volume distribution of a FoCa RESEAL pellet was studied by mercury intrusion porosimetry (MIP) after drying it at 105°C (Van Geet *et al*. 2005). The dry density of the pellet was 2.1 g/cm^3. Figure 2-2 shows the apparent pore volume distribution obtained. The pore radius *r* has to be taken as an apparent pore radius. Besides the typical very fine pores of clay, the apparent pore volume distribution of the dried FoCa pellet shows a significant peak of coarser pores, with a mean radius around 6.1 µm.

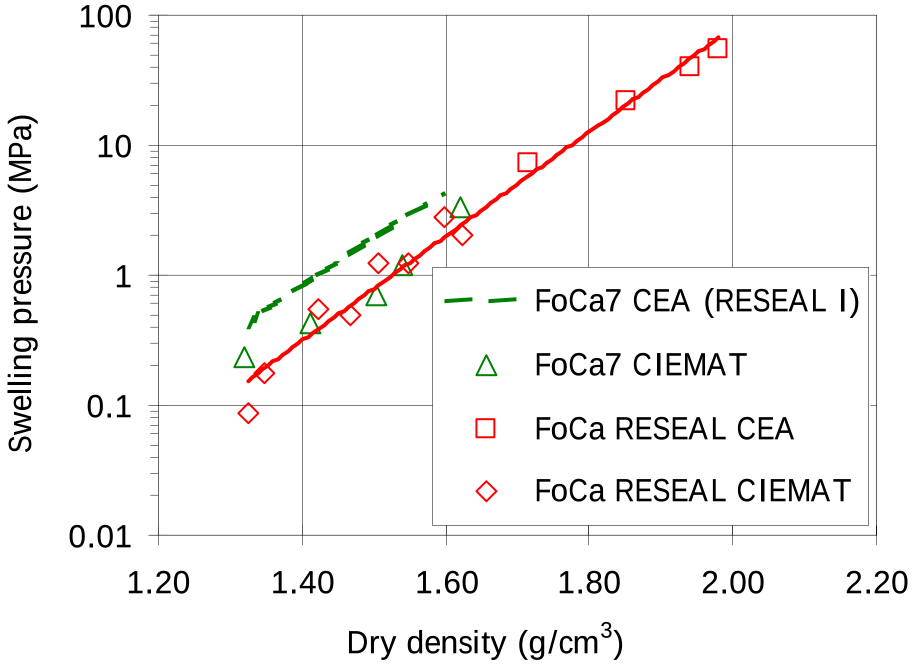

Figure 2-1: Swelling pressure of compacted FoCa clay from different batches determined in different laboratories

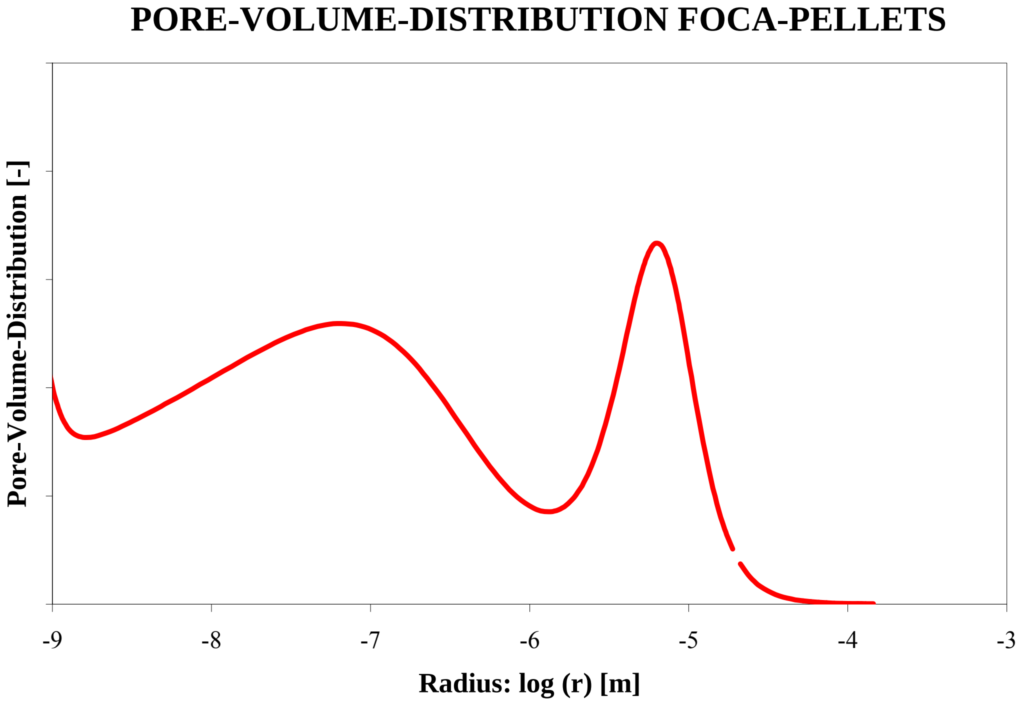

Figure 2-2: Apparent pore volume distribution of a dried FoCa pellet.

3 HYDRO-MECHANICAL PROPERTIES OF SEALING MATERIALS

To analyse the hydration mechanisms of the pellets/powder mixtures and their coupling with the mechanical behaviour, infiltration tests have been performed using three different techniques:

- the oedometer cells with measurement of the swelling pressure (CEA, CIEMAT);
- the double gamma-rays attenuation (CEA); and
- the microfocus X-ray computer tomography (SCK·CEN).

These tests have allowed studying the influence of sample size and dry density on swelling pressure evolution and water absorption, as well as the process of density homogenisation. The range of dry densities tested is related to the dry densities of the seal in the *in situ* shaft sealing test, between 1.3 and 1.6 g/cm^3 (see section Introduction). Furthermore, to better reproduce the *in situ* conditions, only 50/50 pellets/powder mixtures have been analysed. The tests performed provide the modellers with a set of results obtained under well defined boundary conditions.

3.1 Infiltration tests in oedometers (CEA and CIEMAT)

CEA and CIEMAT have performed infiltration tests in oedometric conditions with simultaneous measurement of swelling pressure, water intake and axial deformation. All the tests have been performed with the 50/50 weight percent pellets/powder mixture. The experimental setups and the methodology followed are similar, the major differences being the height and diameter of the specimens, the water intake measurement method and the density of the mixture. The detailed description of the equipments and methods is given in the following sections. The characteristics of the tests performed are summarised in Table 3-1.

Table 3-1: Summary of infiltration tests performed in oedometers.

Reference [1]	**Diameter (cm)**	**Height (cm)**	**Dry density (g/cm^3)**	**Initial *w* pellets (%)**	**Initial *w* powder** [2] **(%)**
RS2A	12	5	1.30	4	12
RS2D	12	10	1.30	5	12
RS2G	12	12	1.30		
RS2J		5	1.45	4	5
MGR7	10	5	1.45	5	12
MGR8	10	10	1.45	5	12
MGR9	10	10	1.45	5	6

Reference [1]	**Diameter (cm)**	**Height (cm)**	**Dry density (g/cm^3)**	**Initial *w* pellets (%)**	**Initial *w* powder** [2] **(%)**
RS2C	12	3	1.60	5	12
RS2K	12	3	1.60		
RS2B	12	5	1.60	4	12
RS2E	12	10	1.60	4	5
RS2F	12	12	1.60	4	5
MGR10 [3]	10	5	1.45		12
MGR11 [3]	10	5	1.60		12

[1] Tests starting by RS performed by CEA, starting by MGR performed by CIEMAT
[2] Water content 12 %: FoCa7
[3] Tests with FoCa7 powder

The geometry of the tests is axisymmetric and presents the boundary conditions shown in Figure 3-1.

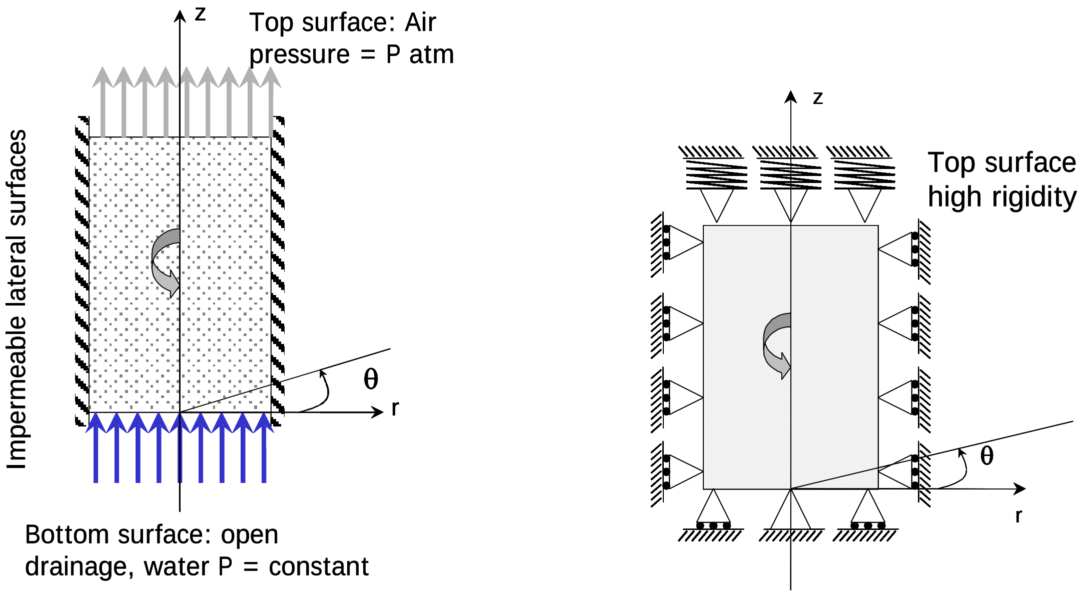

Figure 3-1: Hydraulic (left) and mechanical (right) boundary conditions for the infiltration tests performed in oedometric cells by CEA and CIEMAT.

3.1.1 Tests by CEA

All the tests have been carried out on 50/50 pellets/powder mixtures following the methodology that is described below. The density of the mixtures has been 1.30, 1.45 and 1.60 g/cm^3. The detailed description and analysis of each test is given in Imbert *et al.* (2004).

3.1.1.1 Methodology

The tests have taken place in four stainless steel cells consisting of a cylindrical body of 22.0 or 50.0 cm height, a bottom piston with two water inlets, and a top piston with two outlets for air evacuation (Figure 3-2). The inner diameter of the cylinder is 12.0 cm, which is approximately five times the pellets maximum dimension. The cells are placed in rigid frames that guarantee the constant volume of the sample by hindering the displacement of the pistons. Nevertheless, an external LVDT (linear variable differential transformer) measures the potential axial displacements, whereas a load cell in the upper part of the frame measures the force developed by the specimens.

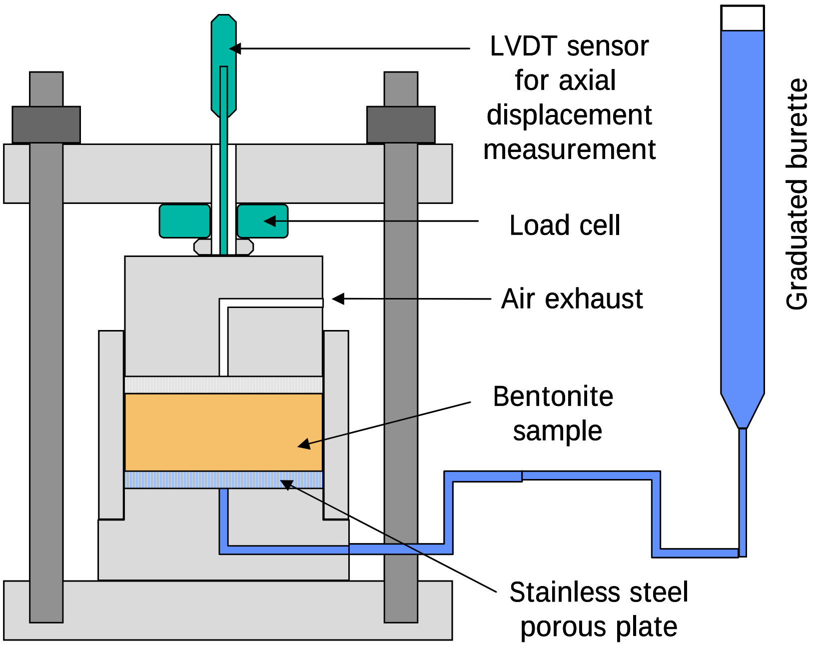

Figure 3-2: Schematic design of the oedometric cells used by CEA.

The specimens are manually manufactured by alternating powder and pellets layers in a 50/50 weight percentage. In this way, dry densities of 1.3 g/cm^3 are reached. To achieve higher dry densities, the mixture is uniaxially compacted directly inside the cell, what results in overconsolidated samples. To attain dry densities of 1.45 and 1.60 g/cm^3, pressures of 1.7 MPa and 9.0 MPa are applied, respectively. The samples are saturated by the bottom face with a 1-m deionised, deaerated water column, while the top outlets remain open to atmosphere and the pressure exerted and the sample vertical strain are measured. The upper part of the water column is a graduated burette that allows the measurement of the water intake. For this, the evaporation loss is taken into account. The temperature of the laboratory is kept at 24±1 °C, and a thermocouple gives the temperature near the cell. All the sensors are connected to a data acquisition system.

At the end of some tests several subsamples have been obtained at different levels, and water content and dry density have been determined in them. The water content has been determined by drying at 105°C and the density by immersion in Kerdane® and measurement of the Archimede's buoyancy.

3.1.1.2 Tests with mixtures of dry density 1.30 g/cm^3

Three tests have been performed by CEA on the 50/50 pellets/powder mixture with dry density 1.30 g/cm^3, the RS2A, RS2D and RS2G, the latter still in progress. In tests RS2A and RS2D, the RESEAL pellets (w=4-5 percent) and the FoCa7 powder (w=12 percent) have been used. The mixture has been saturated under a 1-m water column. The difference among these tests is the height of the specimen. The evolution of swelling pressure in the two finished tests is shown in Figure 3-3. The same pattern is followed in both of them: initially the swelling pressure increases quickly and reaches a peak; from this value it decreases towards a minimum; there is an inflexion and the swelling pressure increases again at a slower rate; eventually a stable value is reached. The difference between these tests comes from the time needed to reach each stage. There is also a small difference in the value of the peak and final pressures. The results are summarised in Table 3-2. The kinetics of the longer sample is slower and the different stages are reached after more infiltration time. The final swelling pressure value is similar to the peak value, whereas in the smaller sample, the final pressure is slightly lower than the peak value.

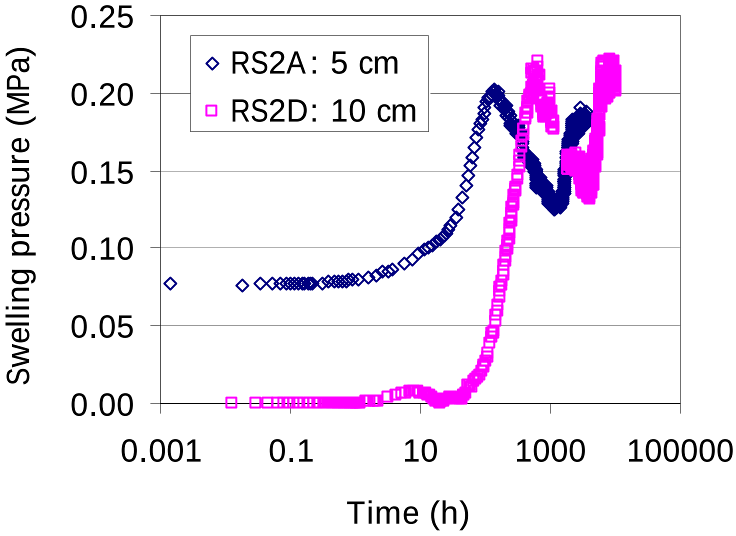

Figure 3-3: Evolution of swelling pressure in mixtures of ρ_d 1.30 g/cm^3.

Table 3-2: Characteristics of the tests performed by CEA on mixtures of ρ_d 1.30g/cm^3.

Test	Height (cm)	Peak P_s (MPa)	Time to peak P_s (h)	S_r at peak P_s (%)	Min P_s (MPa)	Final P_s (MPa)	Time to final P_s (h)	Peak/Final P_s	Time to 100 % S_r (h)	Final S_r (%)	Final/peak time
RS2A	5	0.20	135		0.08	0.19	2200	1.1		105	16
RS2D	10	0.22	633	29	0.13	0.22	6500	1.0		100	10

At the end of the tests several subsamples have been obtained at different levels, and water content and dry density have been determined in them. The final appearance of the block is completely homogeneous, no pellets could be distinguished and the material is very plastic (Figure 3-4). The average values determined are 40.7 percent water content and 1.31 g/cm^3 dry density for test RS2A, and 39.6 percent water content and 1.30 g/cm^3 dry density for test RS2D. The water content is slightly higher on top and bottom of the blocks.

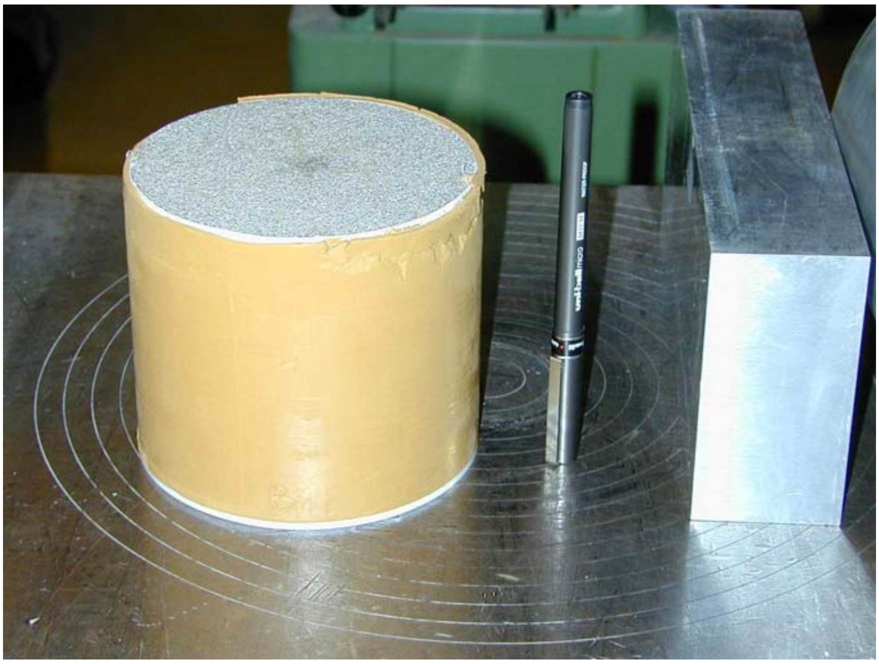

Figure 3-4: Final appearance of the sample of test RS2D (ρ_d 1.30 g/cm^3).

3.1.1.3 Tests with mixtures of dry density 1.45 g/cm^3

A test has been performed by CEA on the 50/50 pellets/powder mixture with dry density 1.45 g/cm^3, the RS2J, with a sample height of 5 cm. The RESEAL pellets and powder (w=5 percent) have been used. The evolution of swelling pressure and water intake is shown in Figure 3-5. The pattern followed is the same described for mixtures of dry density 1.30 g/cm^3, except that the final swelling pressure is noticeably lower than the peak value reached at the beginning. The water intake has been overestimated due to leaks in the hydration system. The results obtained are summarised in Table 3-3.

At the end of the test several subsamples have been taken at different levels, and water content and dry density have been determined in them following the methods described in section 3.1.1.1. The final average water content is 32.5 percent and the dry density 1.46 g/cm^3. Both are quite homogeneous along the sample. The final degree of saturation is 105 percent.

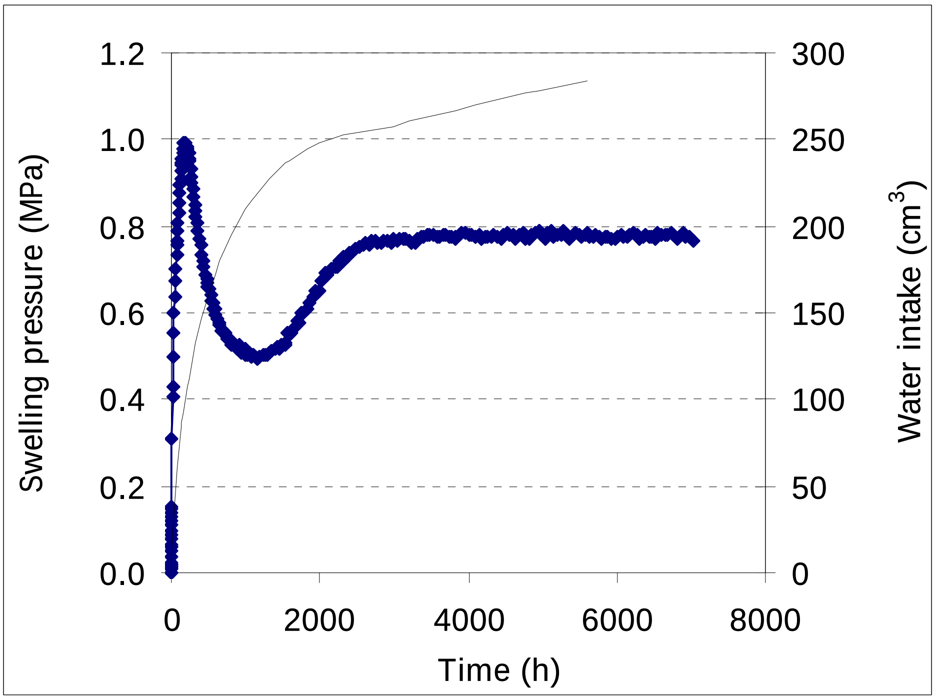

Figure 3-5: Evolution of swelling pressure and water intake in a mixture of ρ_d 1.45 g/cm^3 (test RS2J).

Table 3-3: Characteristics of the test performed by CEA on a mixture of ρ_d 1.45 g/cm^3.

Test	**Height (cm)**	**Peak P_s (MPa)**	**Time to peak P_s (h)**	**S_r at peak P_s (%)**	**Min P_s (MPa)**	**Final P_s (MPa)**	**Time to final P_s (h)**	**Peak/Final P_s**	**Time to 100 % S_r (h)**	**Final S_r (%)**	**Final/peak time**
RS2J	5	1.00	190		0.50	0.80	2700	1.3		105	14

3.1.1.4 Tests with mixtures of dry density 1.60 g/cm^3

Five tests have been performed by CEA on the 50/50 pellets/powder mixture with dry density 1.60 g/cm^3, the RS2C, RS2K, RS2B, RS2E and RS2F. In all these tests the RESEAL pellets and powder (w=5 percent) have been used to prepare the mixture. The difference among these tests is the height of the specimen. The mixtures have been saturated under a 1-m water column pressure, except in test RS2F, in which the pressure has been increased to 0.6 MPa by means of a pump 119 hours after the initiation of the test.

The evolution of swelling pressure in these tests is shown in Figure 3-6, where it can be observed that if follows the pattern seen for lower dry densities: initial quick increase up to a peak value, decrease to a minimum value, and slow recovery of the swelling pressure up to a constant value. In the tests performed for dry density 1.60 g/cm^3, the final swelling pressure value is considerably higher than the initial peak value. The height of the specimen determines the kinetics of the process and the time needed to reach each stage, which is longer the longer the sample. On the other hand, the swelling pressure developed by the 3-cm high samples is noticeably lower than the one obtained in bigger samples. This is attributed to the lack of representativity of such short samples. It is concluded that the minimum height necessary to avoid misleading scale effects is 5 cm (Imbert *et al.* 2004).

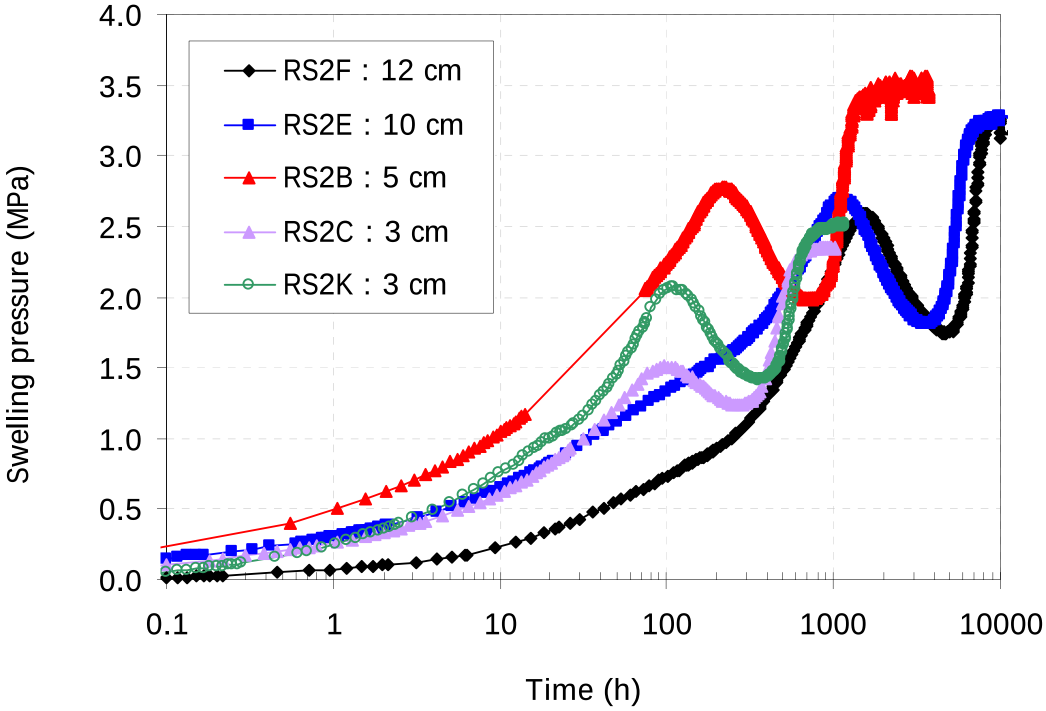

Figure 3-6: Evolution of swelling pressure in mixtures of ρ_d *1.60 g/cm*^{3}.

The water intake has been measured in all the tests. All the curves obtained have a final constant slope that, according to Imbert *et al.* (2004) is a consequence of the evaporation in the hydration circuit. As seen in Figure 3-7, the point in which this constant slope is reached, approximately coincides with the beginning of the stabilisation of swelling pressure. On the other hand, if the water intake is plotted as a function of the square root of time (Figure 3-8), it shows an initial linear pattern with the same slope for all the tests, except RS2F, in which the injection pressure was increased to 0.6 MPa after 119 hours, what results in an increase of the initial slope of the water intake curve. However, the effect of such an increase of the injection pressure (from 0.01 to 0.6 MPa) on the hydration kinetics is not drastic, probably due to the disparity between these pressures and the high initial suction of the bentonite.

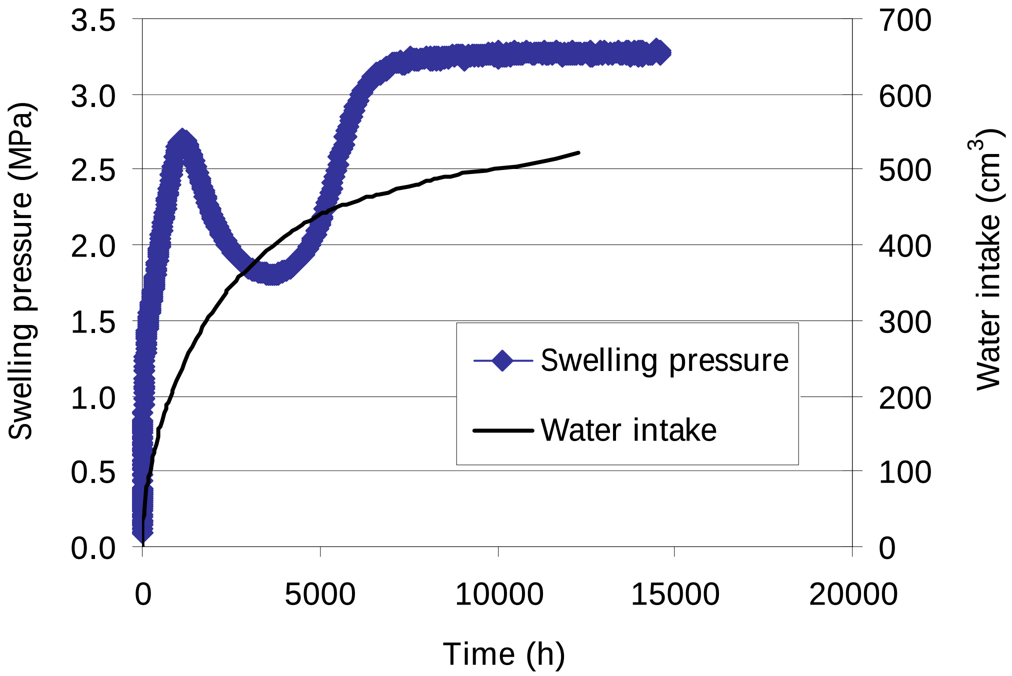

Figure 3-7: Evolution of swelling pressure and water intake in test RS2E (h=10 cm, ρ_d 1.60 g/cm^3).

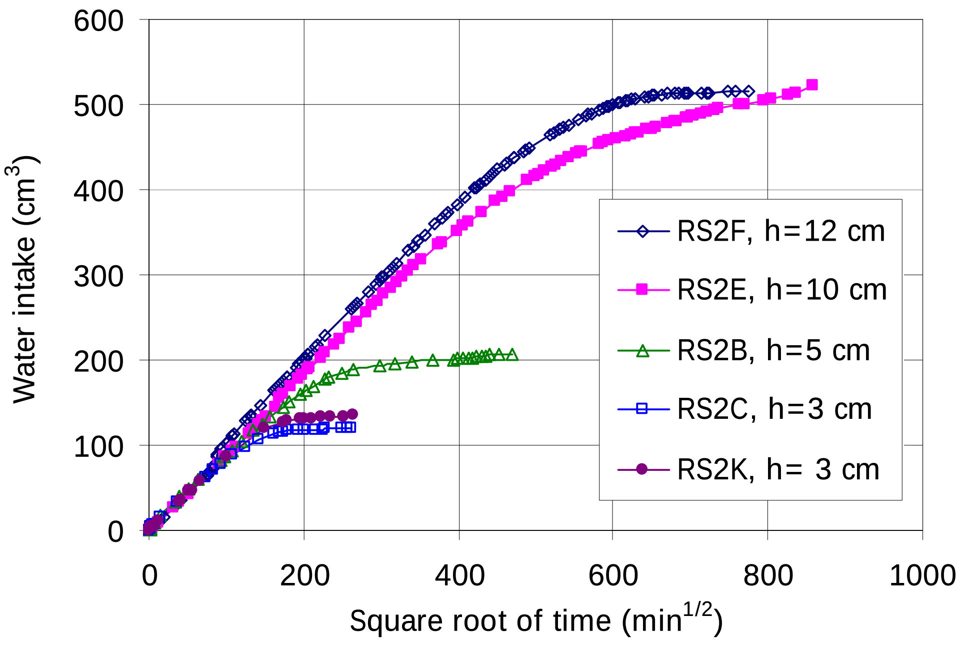

Figure 3-8: Evolution of water intake in mixtures of ρ_d 1.60 g/cm^3.

The results obtained are summarised in Table 3-4. At the end of some of the tests, the blocks were sampled to determine the water content and dry density at different positions (10 or 12). The methods employed are those described in section 3.1.1.1 and the average values obtained are shown in Table 3-5. The lack of homogeneity of the final dry density (between 1.73 and 2.02 g/cm^3), and consequently of the degree of saturation, of test RS2E is noticeable. According to the final measurements, the sample had reached an average final degree of saturation of only 92 percent, what could explain that the final homogenisation was not yet attained.

Table 3-4: Characteristics of the test performed by CEA on mixtures of ρ_d 1.60 g/cm^3.

Test	**Height (cm)**	**Peak P_s (MPa)**	**Time to peak P_s (h)**	**S_r at peak P_s (%)**	**Min P_s (MPa)**	**Final P_s (MPa)**	**Time to final P_s (h)**	**Peak/Final P_s**	**Time to 100 % S_r (h)**	**Final S_r (%)**	**Final/peak time**
RS2C	3	1.51	100	79	1.24	2.36	710	0.6	220	97	7
RS2K	3	2.07	111			2.50	822	0.8			7
RS2B	5	2.77	220	76	1.98	3.56	1550	0.8	600		7
RS2E	10	2.70	1122	71	1.80	3.30	7600	0.8	3072	92	7
RS2F	12	2.71	1560	74	1.70	3.30	8850	0.8	3718	95	6

Table 3-5: Final state of the bentonite obtained by destructive sampling after infiltration tests with mixtures of ρ_d 1.60 g/cm^3.

Test	**Final average w (%)**	**Final average ρ (g/cm^3)**	**Final average ρ_d (g/cm^3)**	**Final average S_r (%)**
RS2C	28.6±0.7	1.98±0.01	1.54±0.01	104±0
RS2E	25.9±0.5	1.92±0.10	1.52±0.07	92±10
RS2F	25.8±0.4			103

3.1.2 Tests by CIEMAT

CIEMAT has carried out tests on 50/50 pellets/powder mixtures compacted to dry density 1.45 g/cm^3, following the methodology that is described below. Two additional tests on compacted FoCa7 powder were performed in order to make out the effect of the presence of pellets on the hydro-mechanical behaviour of the material.

3.1.2.1 Methodology

The tests take place in a cell specially designed to work with pellets/powder mixtures that was already used during the first phase of the project (Figure 3-9). It consists of a cylindrical body with a base and an upper piston that can move in the cylinder. The body has an inner diameter of 10.0 cm and an inner length that may vary between 10 and 5 cm. The top and bottom of the sample are in contact with ceramic porous discs connected to outlets. The cell is placed in a rigid frame that guarantees the constant volume of the sample by hindering the displacement of the piston. Nevertheless, an external LVDT measures the potential axial displacements, whereas a load cell in the upper part of the frame measures the force developed by the specimens. The water intake is measured by an automatic volume change apparatus.

The specimens are manufactured by alternating powder and pellets layers in a 50/50 weight percentage. To attain the dry density of 1.45 g/cm^3 the mixture is compacted in the oedometer cell applying uniaxial pressures of 2.6±0.2 MPa. Test MGR11 was performed with a block obtained from FoCa7 powder compacted to dry density 1.60 g/cm^3 by applying a uniaxial pressure of 11.5 MPa. Once in the oedometer frame, the sample is saturated by the bottom face with a 1-m deionised water column, while the top outlet remains open to atmosphere and the pressure exerted by the clay, the sample deformation and the water intake are measured and automatically recorded. The tests have been performed at laboratory temperature.

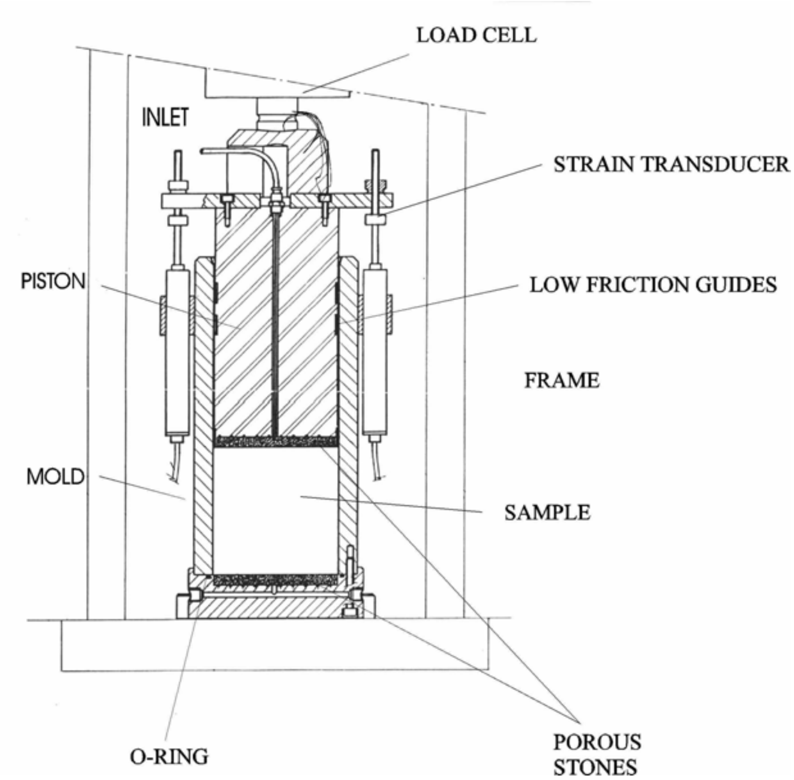

Figure 3-9: Schematic design of the oedometric cell used by CIEMAT.

After dismantling, the blocks were sampled to determine the water content and dry density at different levels. Water content was determined by oven drying at 110°C. To determine dry density, the volume of the specimens was measured by immersing them in a recipient containing mercury and by weighing the mercury displaced.

The analysis of the pore size distribution of some samples has been performed on completion of the tests by mercury intrusion porosimetry. This technique allows the determination of pore size distribution by injecting mercury into the sample at different pressures while controlling the volume intruded. The pressure applied may be related to the minimum pore diameter intruded, taking into account the characteristics of the fluid. The ratio of the volume of mercury intruded (pore volume) to applied pressure (which conditions the minimum pore diameter) allows distribution curves to be obtained establishing the percentage of pores of a size included within a given range. A Poresizer 9320 porosimeter by Micromeritics was used, with a mercury injection pressure range of 7 kPa to 210 MPa, this allowing pore diameters of between approximately 200 and 0.006 µm to be measured. Consequently, the mercury does not intrude the microporosity (pores of a size of less than 0.002 µm, according to the classification of Sing *et al.* 1985). The mercury intrusion method allows access to be gained only to the macroporosity and to part of the mesopores. Before the samples are inserted in the porosimeter, the water is removed from the pores by freeze-drying.

3.1.2.2 Tests with pellets/powder mixtures

CIEMAT has performed tests MGR7, MGR8 and MGR9 with 50/50 weight percent pellets/powder mixtures compacted at dry density of 1.45 g/cm^3. To check the influence of sample height, the thickness of the sample in test MGR7 was 5 cm and in the other tests was of 10 cm. Tests MGR7 and MGR8 were performed with RESEAL II pellets (water content 5 percent) and FoCa7 powder (water content 12 percent), as there is a slight difference in colour between the two FoCa batches and this would help in the final evaluation of the homogenisation of the mixture. In order to check if the difference in water content ratio of the pellets and powder has an influence on the hydro-mechanical behaviour of the mixture, test MGR9 was performed with the RESEAL II pellets and powder mixture (water content at the moment of preparation of the sample 6 percent).

Figure 3-10 shows the evolution of swelling pressure in the three tests. All of them display an initial similar pattern: a quick swelling pressure increase (which is softer and slower in the thicker samples), followed by its decrease. This decrease was ensued by a swelling pressure recovery in test MGR7 and MGR9. Furthermore, the final swelling pressure is lower than the peak pressure in test MGR9 and equal to the peak pressure in test MGR7. The differences between these two tests are the initial water content of the powder, which is lower in test MGR7 (5 *vs*. 12 percent), and the height, which is lower in test MGR7 (5 *vs*. 10 cm). The sudden increase of swelling pressure towards 2800 hours in test MGR7 is due to an increase of the injection pressure to 0.6 MPa, what was achieved by connecting the hydration circuit to a pressure controller. On the other hand, in test MGR8 the swelling pressure almost disappeared after the first peak and did not recover. No explanation has been found for this behaviour, and the test was dismantled before full saturation.

The water intake evolution in these tests is shown in Figure 3-11. After the increase of injection pressure in test MGR7 (2800 hours), the water intake was not further measured. A summary of the results obtained can be found in Table 3-6.

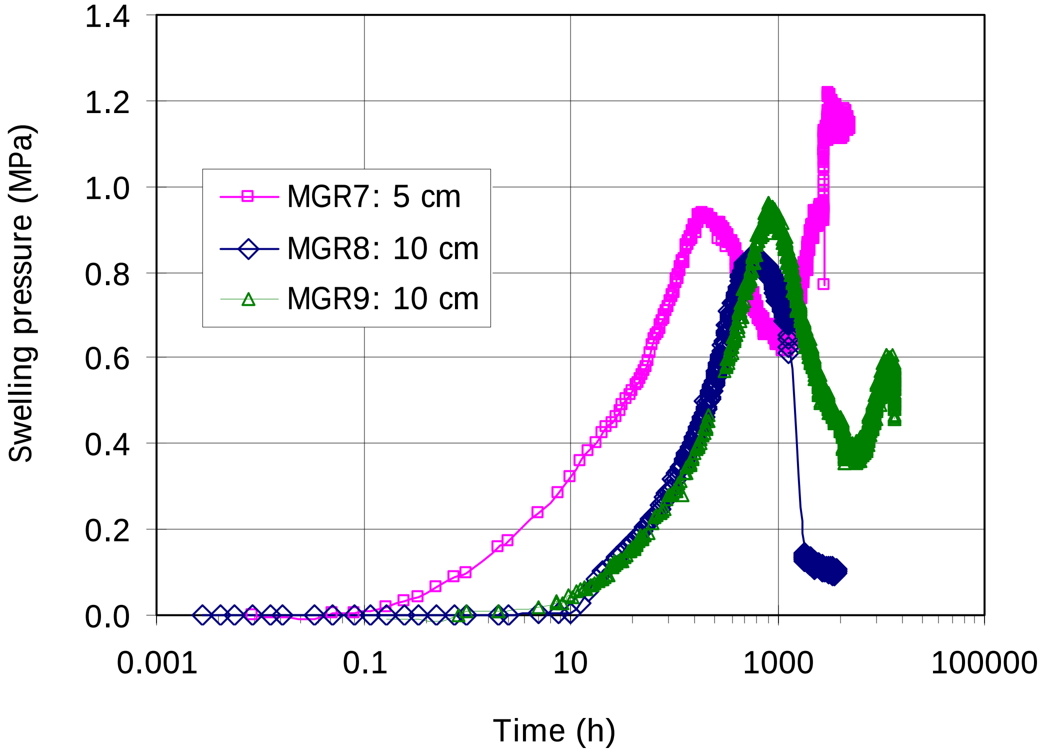

Figure 3-10: Evolution of swelling pressure in mixtures of ρ_d 1.45 g/cm^3.

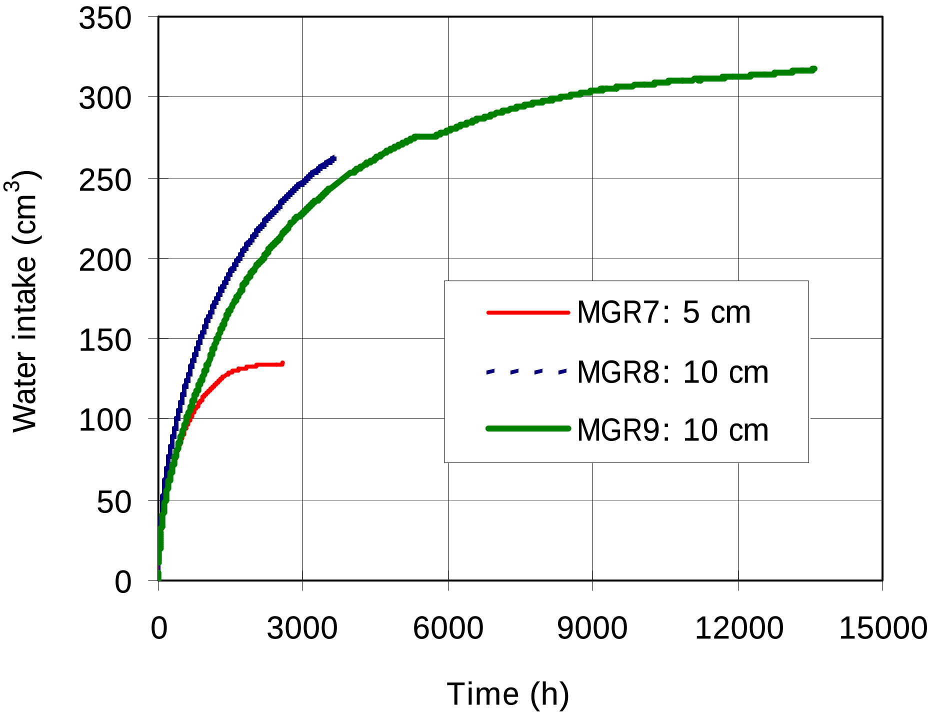

Figure 3-11: Evolution of water intake in mixtures of ρ_d 1.45 g/cm^3.

Table 3-6: Characteristics of the tests performed by CIEMAT on mixtures of dry density 1.45 g/cm^3.

Test	**Height (cm)**	**Peak P_s (MPa)**	**Time to peak P_s (h)**	**S_r at peak P_s (%)**	**Min P_s (MPa)**	**Final P_s (MPa)**	**Time to final P_s (h)**	**Peak/Final P_s**	**Time to 100 % S_r (h)**	**Final S_r (%)**	**Final/peak time**
MGR7	5	0.90	180	57	0.60	0.96	2400	0.9	665	>101	13
MGR8	10	0.83	622	62	0.10					97	
MGR9	10	0.96	813	50	0.40	0.60	11800	1.6	7492	106	15

At the end of the tests the pellets were not appreciable (Figure 3-12), although a detailed inspection allowed distinguishing areas of different coloration in the tests performed with RESEAL pellets and FoCa7 powder (MGR7 and MGR8). After dismantling, the blocks were sampled to determine the water content and dry density at different levels (3 or 4, depending on the height of the block) according to the methods described in section 3.1.2.1. The average values obtained are shown in Table 3-7. It is noticeable the lack of homogeneity of the degree of saturation in test MGR9, what is probably due to the fact that full saturation had not been attained when the test was dismantled.

The external specific surface of four samples from test MGR9 has been determined by nitrogen absorption (single point BET method), and the average values obtained are also given in the Table. The specific surface increases from the hydration surface towards the top of the block (from 65 to 81 m^2/g).

Figure 3-12: Sections obtained by cutting of the block of test MGR9.

Table 3-7: Final state of the bentonite obtained by destructive sampling after infiltration tests with mixtures of ρ_d 1.45 g/cm^3.

Test	Final average *w* (%)	Final average ρ_d (g/cm^3)	Final average S_r (%)	External specific surface (m^2/g)
MGR7	33.1±0.8	1.46±0.02	106±0	
MGR8	30.3±2.9	1.44±0.02	95±7	
MGR9	32.8±0.1	1.44±0.01	103±1	74±7

The analysis of the pore size distribution of four samples of test MGR9 taken at different distances from the hydration surface has been performed by mercury intrusion porosimetry, as described in section 3.1.2.1. Figure 3-13 shows the results in terms of incremental pore volume per gram of sample. Three main families of pores may be appreciated in the four samples: large (diameter higher than 10 µm), medium and small (diameter between 0.2 and 0.006 µm). The same curves are presented in Figure 3-14 expressed in terms of the accumulated percent of pore volume *vs*. the diameter. The percentages have been recalculated according to the percentage of total porosity actually intruded by mercury, which is between 78 percent for the top of the sample and 48 percent for the sample closer to the hydration surface. This means that the volume of pores smaller than 0.006 µm decreases from the hydration surface towards the top. On the contrary, the percentage of pores of medium size (between 0.2 and 10 µm) increases towards the top of the block. This could be attributed to the lack of complete homogenisation pointed above. As well, saturation seems to imply a redistribution of porosity, increasing the percentage of micropores.

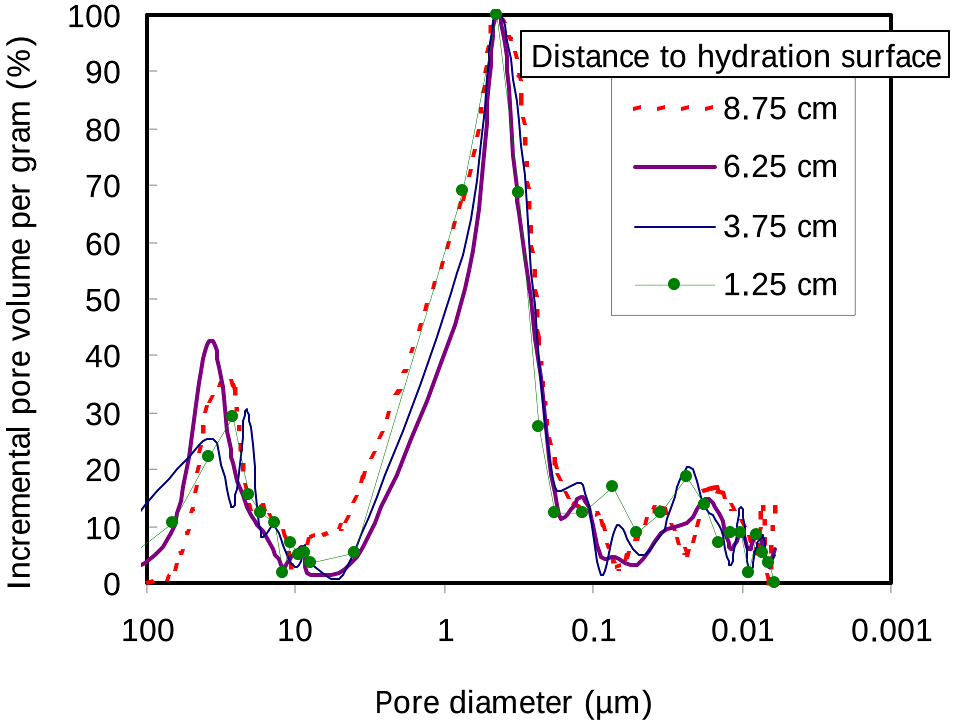

Figure 3-13: Incremental porosimetric curve for samples of test MGR9.

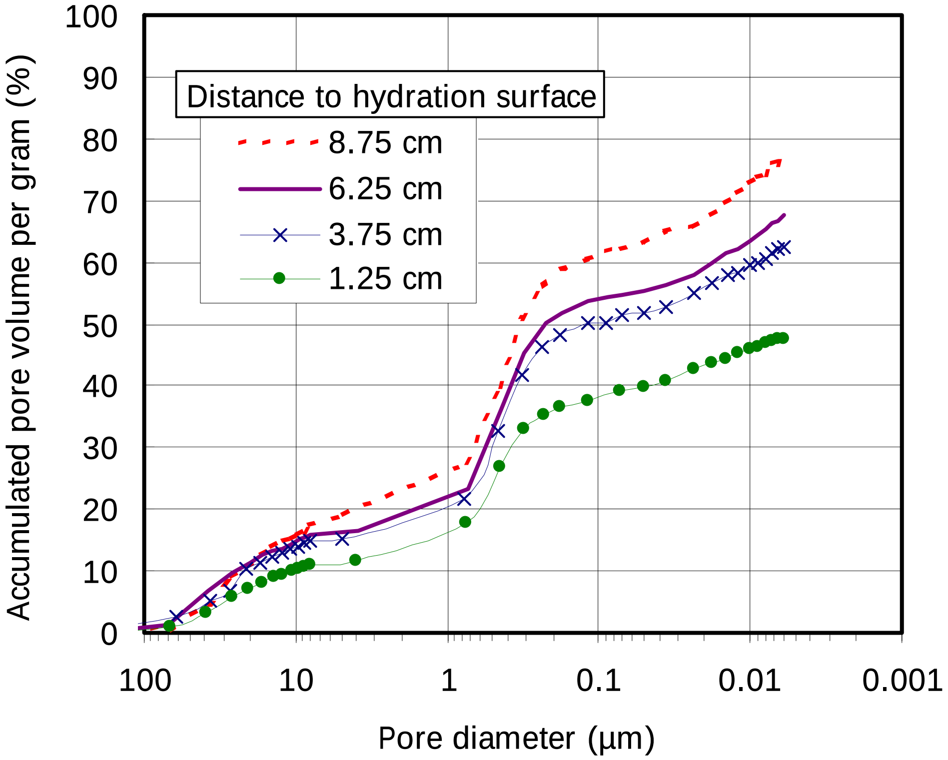

Figure 3-14: Accumulated porosimetric curves for samples of test MGR9. The percentages are recalculated according to the percentage of total porosity actually intruded by mercury.

3.1.2.3 Tests with compacted powder

Two tests have been performed with FoCa7 powder compacted at nominal dry density 1.45 g/cm^3 (MGR10) and 1.60 g/cm^3 (MGR11), with a height of 5 cm. In both tests the swelling pressure development has followed the same pattern observed in the mixtures, with the intermediate phase of swelling pressure decrease. Indeed the swelling pressures reached in each test are quite different, and the relation between the final pressure and the initial peak pressure is also unlike: for the lower dry density the final pressure value is the same than the initial peak, whereas for dry density 1.60 g/cm^3, the final swelling pressure is considerably higher than the initial peak. On the contrary, the kinetics of swelling pressure development in both tests is rather similar, although the final stabilisation of swelling pressure in test MGR11 took more time. The evolution of water intake in these tests is shown in Figure 3-16. As expected, the higher permeability of the low-density sample provoked a quicker water intake, although the time to reach full saturation is analogous in both tests. These results are summarised in Table 3-8.

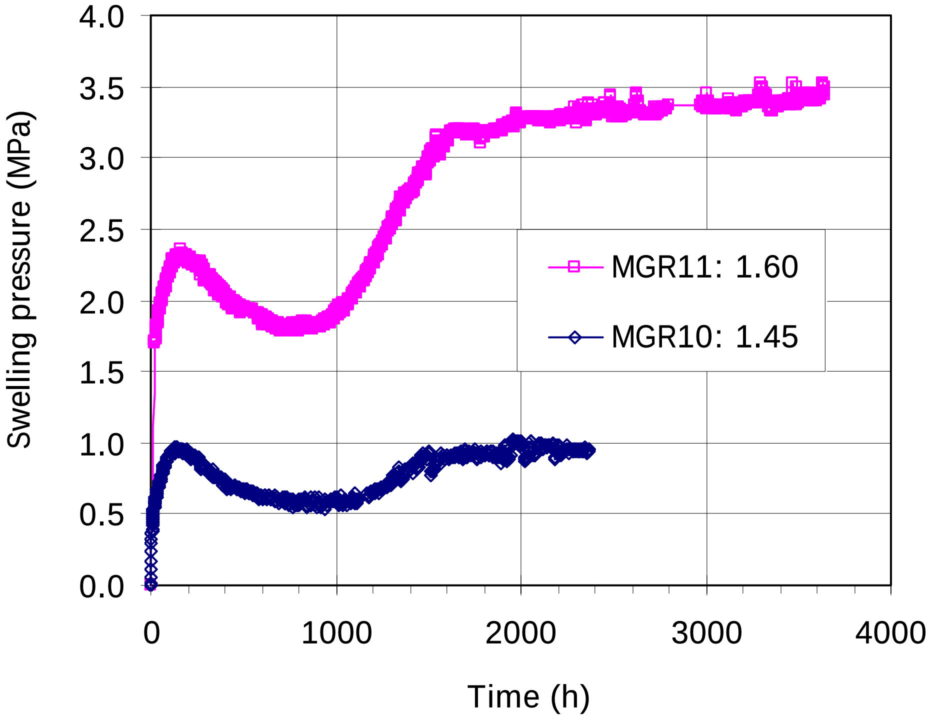

Figure 3-15: Evolution of swelling pressure in infiltration tests with FoCa7 powder compacted at different dry densities (in g/cm^3).

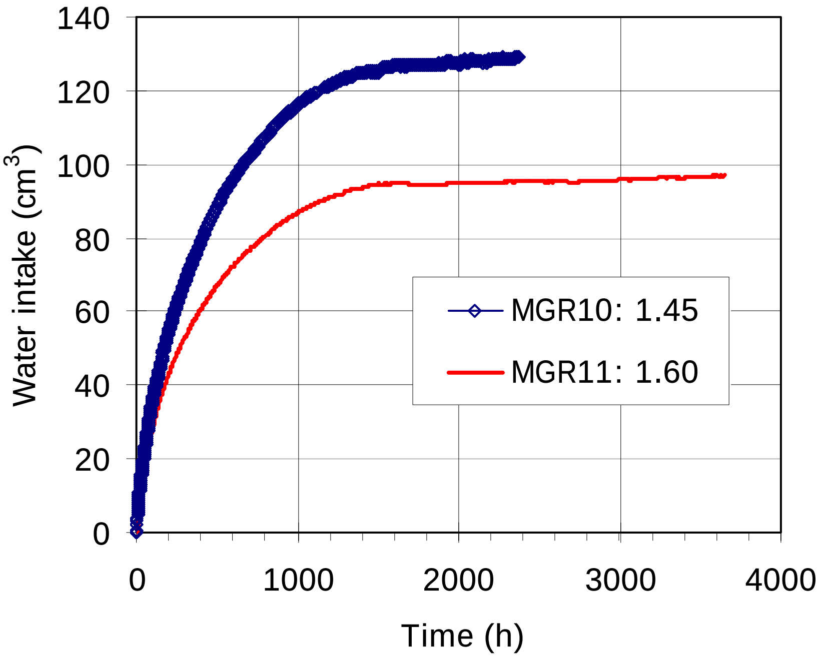

Figure 3-16: Evolution of water intake in infiltration tests with FoCa7 powder compacted at different dry densities (in g/cm^3).

Table 3-8: Characteristics of the tests performed by CIEMAT on compacted FoCa7 (height of the samples: 5 cm).

Test	**ρ_d (g/cm^3)**	**Peak P_s (MPa)**	**Time to peak P_s (h)**	**S_r at peak P_s (%)**	**Min P_s (MPa)**	**Final P_s (MPa)**	**Time to final P_s (h)**	**Peak/Final P_s**	**Time to 100 % S_r (h)**	**Final S_r (%)**	**Final/peak time**
MGR10	1.45	0.97	130	58	0.53	1.0	1950	1.0	2200	104	15
MGR11	1.60	2.35	167	72	1.78	3.4	3000	0.7	2300	107	18

The final analysis of the samples has included the determination of water content and dry density at three different levels following the methodology described in the previous section. The results obtained are shown in Table 3-9. As in the tests performed with mixtures, the final degrees of saturation are higher than 100 percent, especially for the higher density. As it has been explained (section Material), this is because they were computed considering the density of the water as 1.00 g/cm^3, which is incorrect for high plasticity materials.

The external specific surface of three samples from test MGR11 has been determined by nitrogen absorption (single point BET method), and the average values obtained are also given in Table 3-9.

Table 3-9: Final state of the bentonite obtained by destructive sampling after infiltration tests with compacted FoCa7.

Test	**Final average w (%)**	**Final average ρ_d (g/cm^3)**	**Final average S_r (%)**	**External specific surface (m^2/g)**
MGR10	32.4±0.1	1.46±0.01	104±1	
MGR11	27.4±0.1	1.59±0.01	107±1	72±6

3.1.3 Summary and discussion

All the infiltration tests described above have been performed following a common procedure whose characteristics are:

- the material used is a 50/50 weight percent pellets/powder mixture;
- the tests have been performed under constant volume;
- the sample has the shape of a column, with a height higher than 3 cm;
- saturation takes place through the bottom surface under a low injection pressure (0.01 MPa), with air evacuation through the opposite surface; and,
- the dry density is between 1.3 and 1.7 g/cm^3 and the initial water content between 4 and 12 percent.

Under these conditions, the kinetics of swelling pressure development goes along a well defined pattern in which the following phases can be distinguished:

1. quick increase of pressure up to a peak;
2. progressive decrease of swelling pressure down to a minimum value that remains for a certain time;
3. new increase of swelling pressure at a decreasing rate, and;
4. eventual achievement of a stable pressure value.

The variations among the tests are due to the effect of initial height and dry density. Thus, the initial peak is less sharp for the samples of high initial dry density and height. Besides, the relation between the initial peak and the final swelling pressure depends on the dry density of the sample (Figure 3-17, Figure 3-18): for the lower dry densities, the peak value is similar or higher than the final value, whereas for dry density 1.6 g/cm^3, the final swelling pressure value is clearly higher than the peak one. Besides, the time needed to reach the initial peak pressure depends on dry density and height of the sample, increasing with both (Figure 3-19).

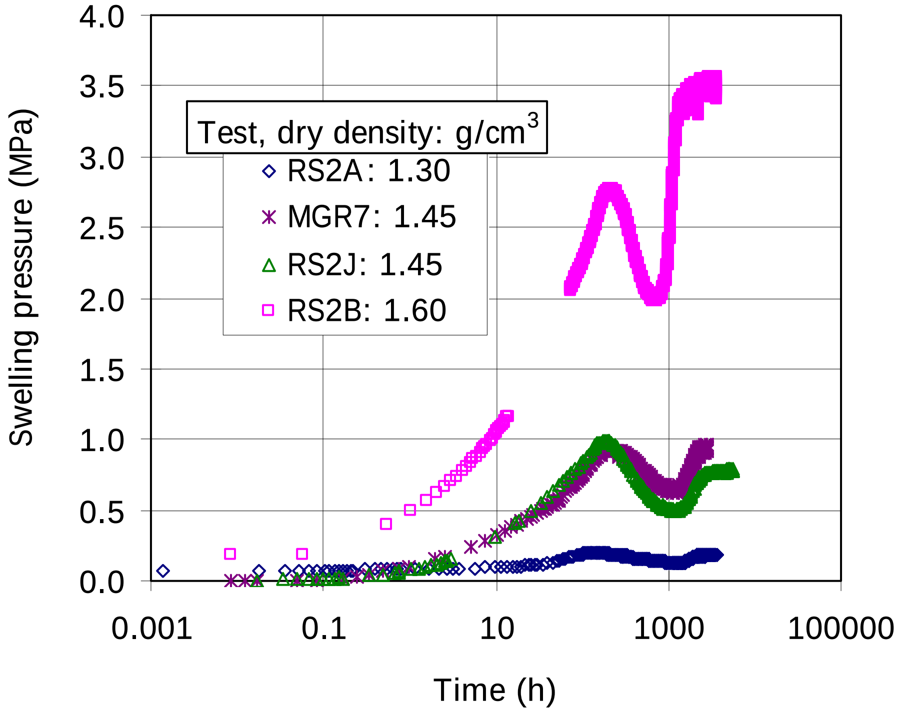

Figure 3-17: Evolution of swelling pressure in infiltration tests with 5-cm height samples of 50/50 pellets/powder mixtures.

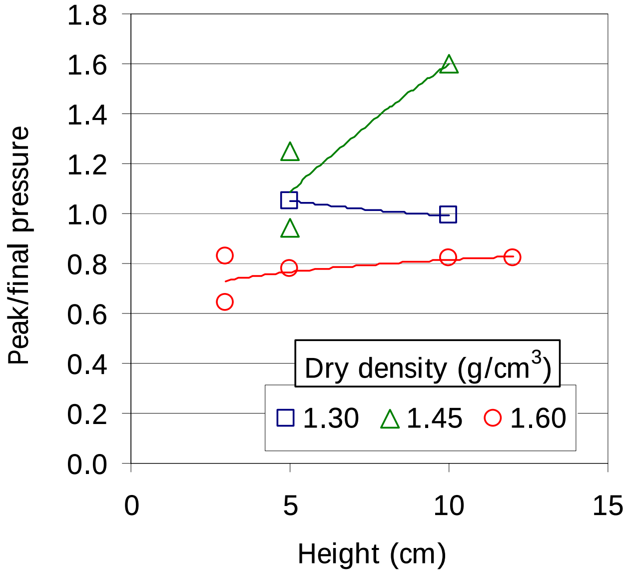

Figure 3-18: Relation between the peak and the final swelling pressures measured in the infiltration tests with mixtures.

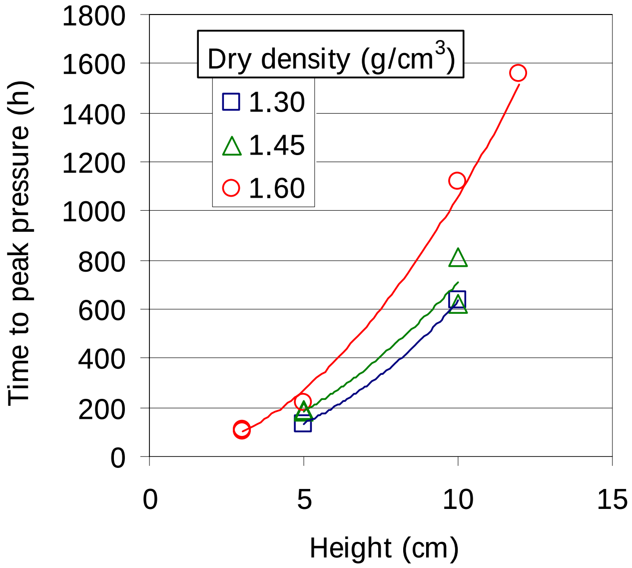

Figure 3-19: Time needed to reach the initial peak pressure in the infiltration tests with mixtures.

The swelling pressure curves obtained have been normalised with respect to the time to reach the peak pressure and to the maximum swelling pressure value (Imbert *et al*. 2004), in order to have a dimensionless representation. The curves thus obtained for the tests of dry density 1.60 g/cm^3 are plotted in Figure 3-20. In this way the kinetics of the tests becomes identical, irrespective of the height of the sample. Hence, there is not a scale effect on the results obtained, and samples of 5 or 12-cm height seem to be equally representative. Only test RS2F, in which the hydration pressure was 60 times higher, deviates from the common pattern. This is due to the fact that the injection pressure has non-linear effects on the mechanical behaviour, since it has an influence on the coefficients κ and κ(*s*), both dependent on suction. On the other hand, the relation between the time to reach the final swelling pressure and the time to reach the peak pressure depends on dry density, being higher for the lower densities (Figure 3-21). For this reason, the dimensionless curves for dry densities 1.30 and 1.45 g/cm^3 are plotted separately in Figure 3-22. The comparison between this Figure and Figure 3-20 shows the influence of the initial dry density on the kinetics of swelling pressure evolution, and the existence of two distinct behaviours for low and high densities. Since the dry density of the pellets is always the same, the different dry densities of the mixture are caused by differences in powder density. The low dry densities of the powder result in higher initial permeability along the powder paths, which become preferential hydration channels, giving place to faster initial hydration and development of swelling pressure.

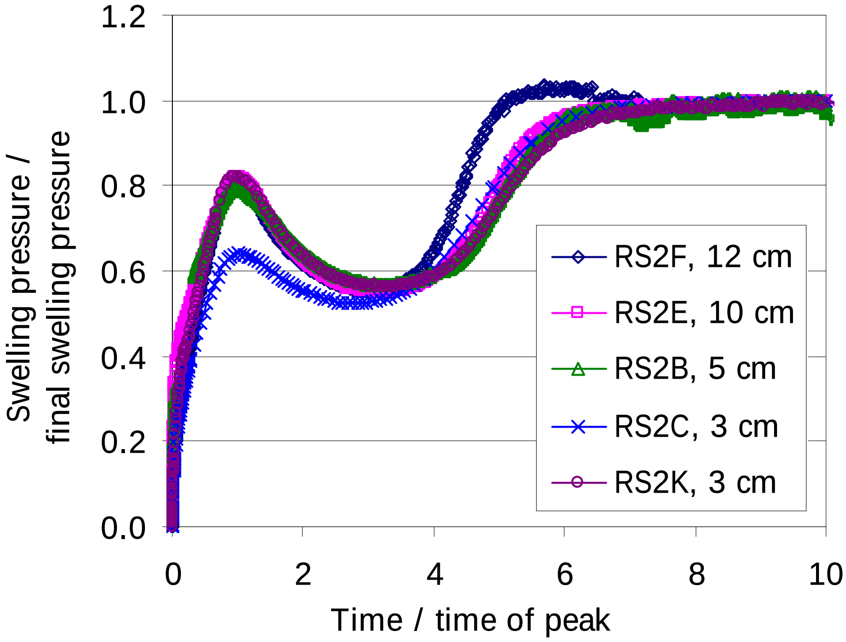

Figure 3-20: Dimensionless evolution of swelling pressure in the infiltration tests performed with mixtures (50/50) compacted at ρ_d *1.60 g/cm*^{3}*.*

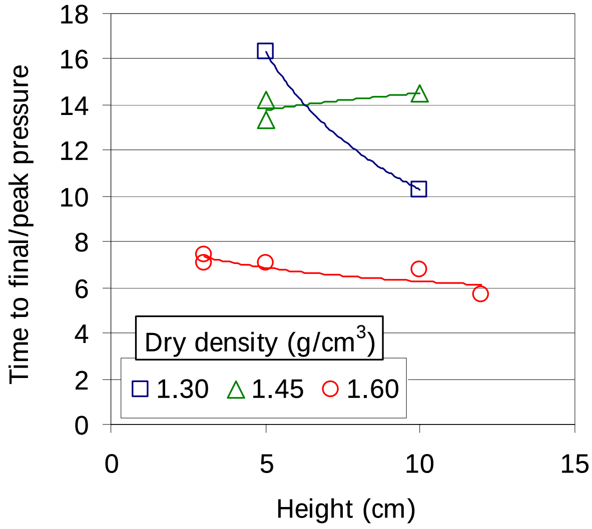

Figure 3-21: Relation between the time needed to reach final and peak swelling pressures for the infiltration tests with mixtures.

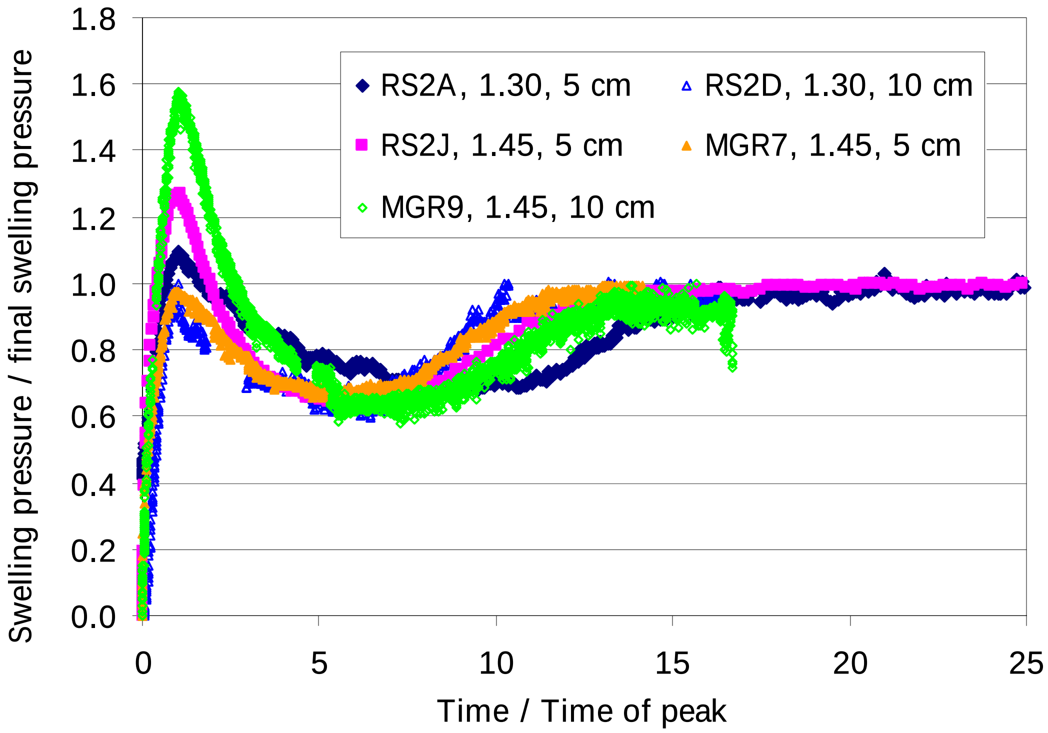

Figure 3-22: Dimensionless evolution of swelling pressure in the infiltration tests performed with mixtures (50/50) compacted at low dry densities (indicated in g/cm^3).

It must be pointed out that this same pattern has been observed in the tests performed with compacted FoCa7 powder MGR10 and MGR11 (Figure 3-15). In fact, if the results obtained for compacted powder and for pellets/powder mixtures in samples of the same dry density and height are compared (Figure 3-23, Figure 3-24), not only the swelling evolution pattern, but also the actual swelling pressure values are similar. Concerning the water intake, the comparison of tests MGR7 (mixture) and MGR10 (compacted powder) points to a faster initial intake of the mixture, although the same trend is found for both materials in the remainder of the tests. However, this does not translate into a quicker development of swelling pressure in the mixture, on the contrary, the kinetics of swelling pressure development is slightly quicker for compacted samples than for mixtures. Gatabin *et al.* (2000) found also the same pattern of behaviour on compacted samples of another batch of FoCa powder (Figure 3-26).

Summing up the observations concerning the swelling pressure evolution pattern, it can be concluded that the increase/decrease/increase pattern has been found irrespective of:

- the size of the sample, either height or diameter, for analogous results have been found by laboratories using different experimental setups: EGC (Pasquiou 1999, 2001), SCK·CEN (Volckaert *et al.* 2000);
- the injection pressure, that simply hastens the process;
- or the initial fabric (compacted powder or mixtures).

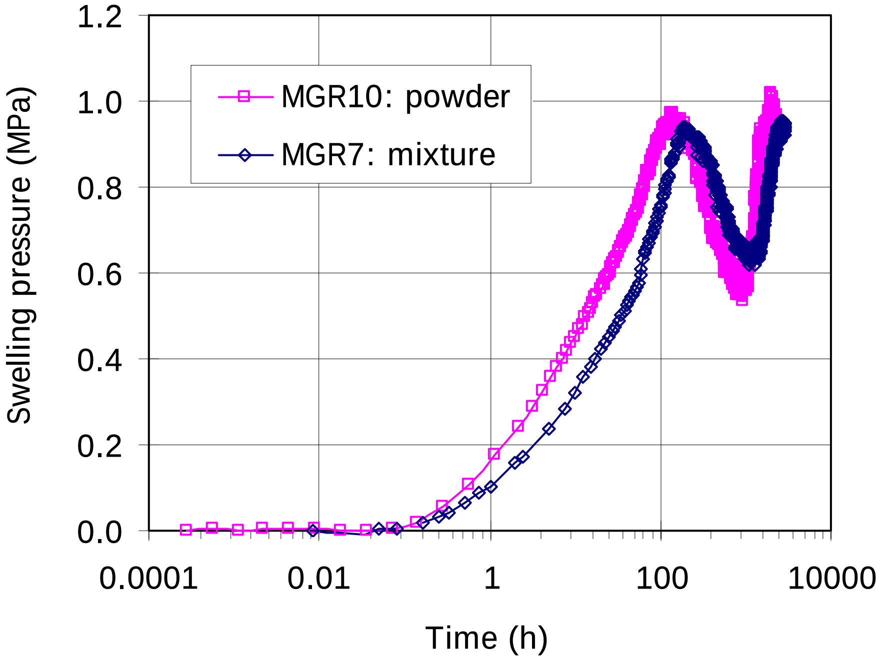

Figure 3-23: Evolution of swelling pressure in 5-cm height FoCa samples compacted at ρ_d *1.45 g/cm*^{3}*.*

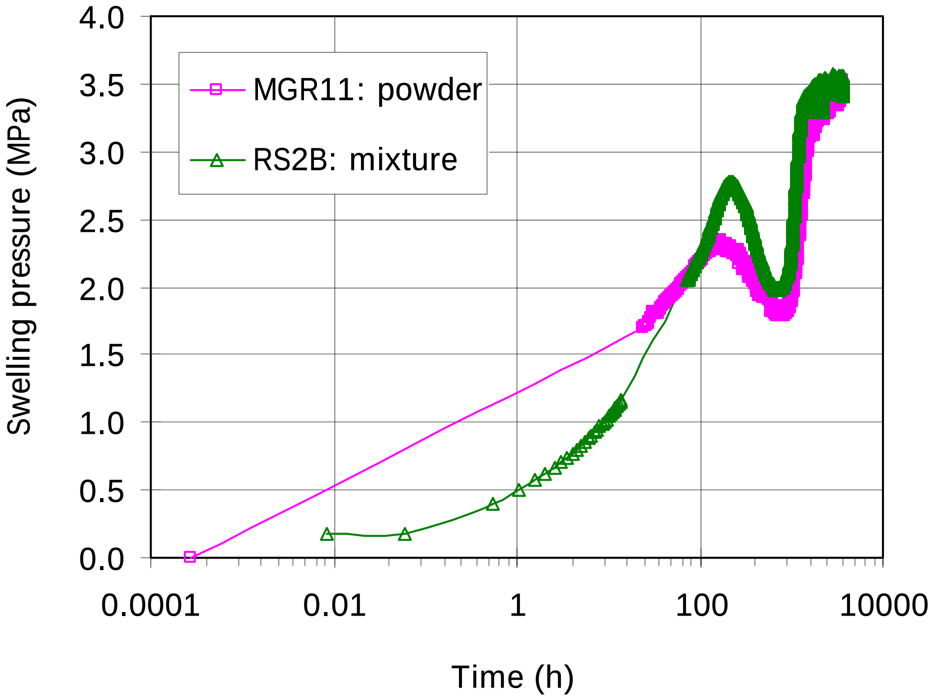

Figure 3-24: Evolution of swelling pressure in 5-cm height FoCa samples compacted at ρ_d 1.60 g/cm^3.

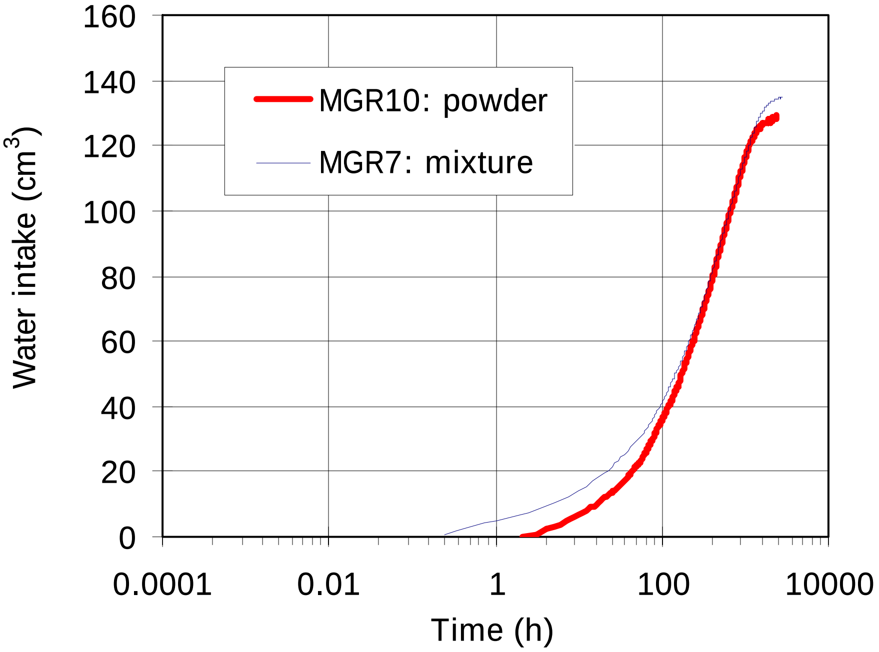

Figure 3-25: Evolution of water intake in 5-cm height FoCa samples compacted at ρ_d 1.45 g/cm^3.

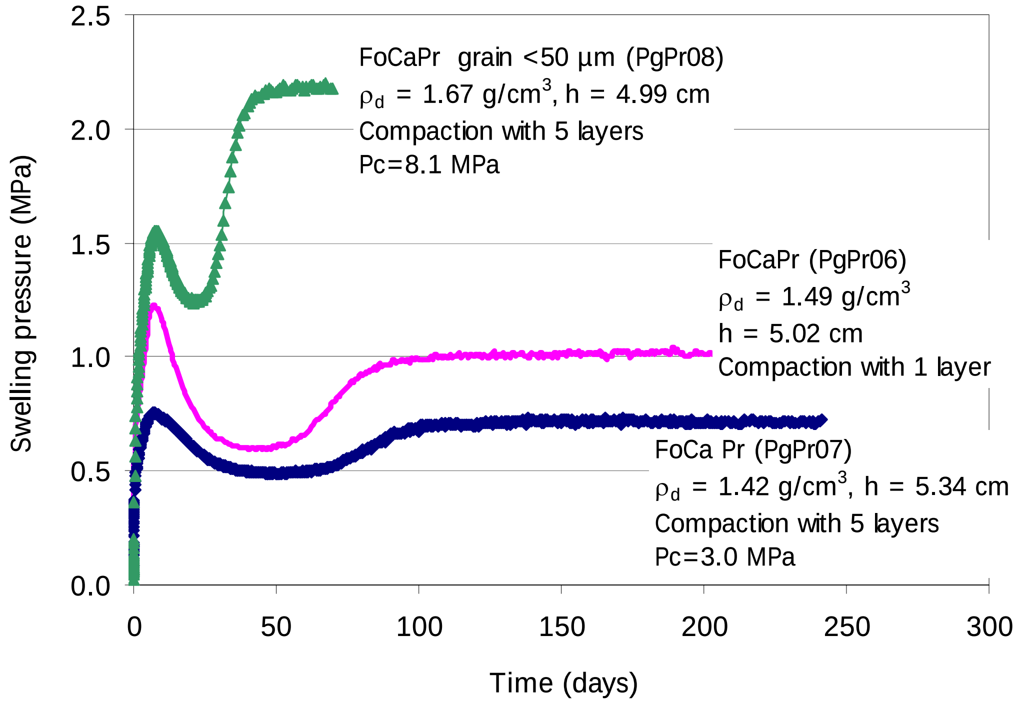

Figure 3-26: Evolution of swelling pressure in compacted samples of FoCa-Pr powder (Gatabin et al. *2000).*

The analysis of the results performed by CEA applying the code CASTEM, based on the model of Alonso *et al.* (1990), explain the non-monotone evolution of swelling pressure as a consequence of the plastification of the material upon saturation, the swelling pressure decrease being a result of the isotrope plastification induced by the radial confinement. Its magnitude depends on the initial characteristics of the material: overconsolidation, suction, water content (Imbert *et al.* 2004).

Brackley (1973) observed that the time/swelling pressure relationship of a soil was affected by the initial water content of the material, and that for low initial water contents, an initial peak followed by a decrease of swelling pressure was detected. This was explained by the high initial suction of the microstructure, whose swelling initially predominates over the collapses of the macrostructure that are observed afterwards. Komine & Ogata (1994) found that the evolution of swelling pressure of a compacted bentonite with low initial water content showed two peaks provided that the initial dry density was not too high, whereas the same material with higher initial water content displayed a constant swelling pressure increase. They consider that the initial pressure peak is due to the filling of the voids of the structure, that constitute a bigger volume in low density, low water content samples.

Hence, it seems that the initial water content may also have an influence on the swelling pressure development kinetics. Furthermore, in the infiltration tests performed by CIEMAT during the first phase of the project, the decrease of swelling pressure after the initial peak was not observed (Figure 3-27). These tests were performed with a 50/50 FoCa bentonite pellets/powder mixture following the same procedures and in the same equipment described in the previous section. The only difference between the first and the second phase tests has been the initial water content of the pellets and powder, that was higher in the earlier tests, for the material came from a different manufacturing batch. This could be the reason for the absence of the increase/decrease/increase pattern of swelling pressure development. However, an intermediate period of softer pressure increase is actually detected. This could indicate that the collapse of the macrostructure on saturation is more important when hydration starts from high suctions, whereas it is compensated by an overall swelling of the microstructure when the initial suction is lower.

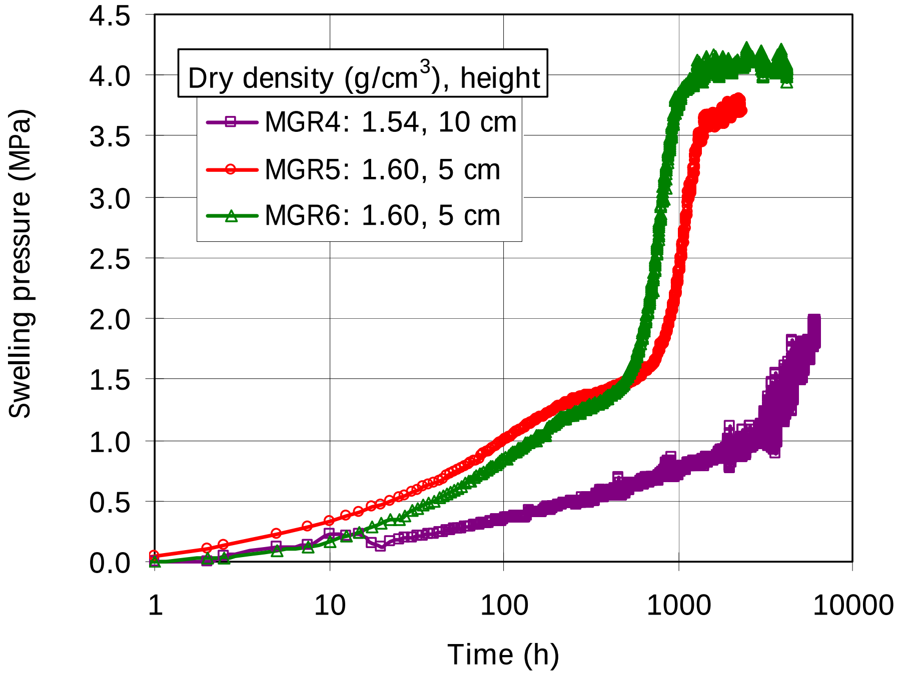

Figure 3-27: Evolution of swelling pressure in infiltration tests performed in 50/50 FoCa pellets/powder mixtures during RESEAL I.

Concerning the swelling pressure values obtained in the infiltration tests, the results of the tests performed with mixtures and with compacted powder in big oedometric cells are summarised in Table 3-10. The swelling pressure values recorded at the end of these tests are plotted as a function of the final dry density in Figure 3-28, in which the following fitting between swelling pressure (P_s, MPa) and final dry density (ρ_d, g/cm^3) is also drawn:

$$P_s = 0.0061\ \rho_d^{\ 13.272} \qquad [2.]$$

This curve can be compared with the curve obtained for compacted powder samples of small dimensions (Equation 1), also plotted in the Figure. The values obtained in big oedometers tend to be slightly higher than those obtained in small samples, both for the mixtures and for the compacted powder. Thus, the effect of scale on swelling pressure seems to be more important than the initial fabric. In any case, the difference is not significant and probably lies within the error bands. The coherence between swelling pressure measurements in mixtures and homogeneous samples had already been observed during RESEAL I (Volckaert *et al.* 2000, Dereeper *et al.* 2001).

Table 3-10: Swelling pressure obtained in the big oedometers.

Test	**Height (cm)**	**Initial ρ_d (g/cm^3)**	**Average initial *w* (%)**	**Final P_s (MPa)**	**Final ρ_d (g/cm^3)**	**Average final *w* (%)**	**Final S_r (%)**
RS2A	5	1.30	7.8	0.19	1.30	43.6	110
RS2D	10	1.30	8.2	0.22	1.30		
RS2G	12	1.30					
RS2J	5	1.45	4.8	0.80	1.45	32.5	103
MGR7	5	1.45		0.96	1.45	33.1	106
MGR8	10	1.45			1.44	30.3	95
MGR9	10	1.45		0.60	1.45	32.8	103
RS2C	3	1.60	8.2	2.36	1.59	28.6	112
RS2K	3	1.60	5.0	2.50	1.58		
RS2B	5	1.60	8.1	3.56	1.59		
RS2E	10	1.60	4.8	3.30	1.60	25.9	103
RS2F	12	1.60	4.8	3.30	1.60	25.8	103
MGR10	5	1.45	12.0	0.95	1.46	32.4	104
MGR11	5	1.60	12.0	3.39	1.59	27.4	107

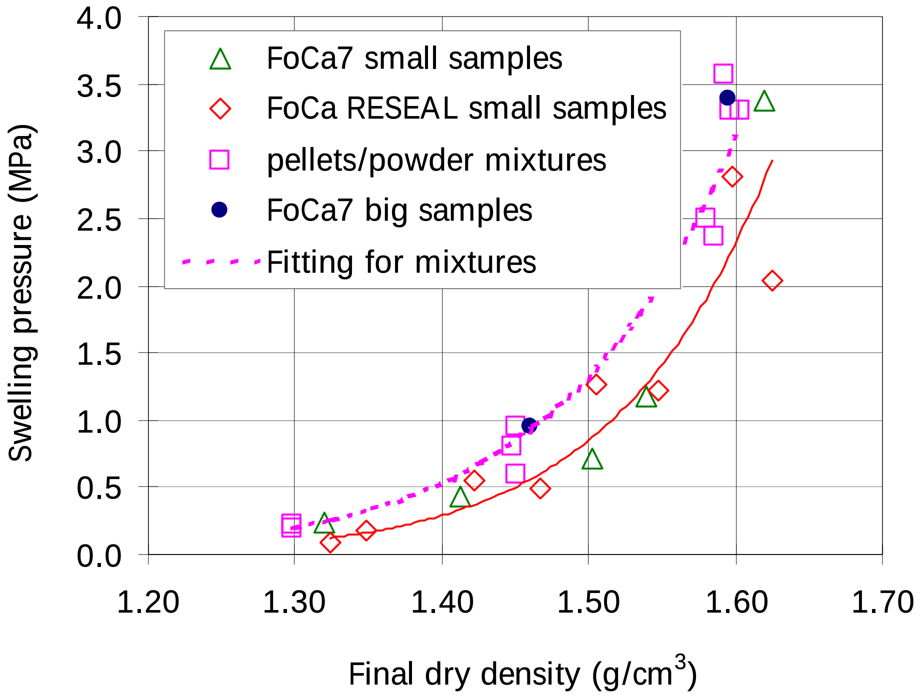

Figure 3-28: Swelling pressure of FoCa bentonite as determined in samples of different sizes and densities of compacted powder and pellets/powder mixtures.

3.2 *Dual-gamma rays attenuation (CEA)*

Two infiltration tests have been performed in a setup specially designed to follow online the evolution of water content and dry density along the sample. The method is based on dual-gamma ray attenuation, which allows the simultaneous measurement of liquid and solid phases concentration in a given location.

3.2.1 Methodology

Infiltration through an expansive soil modifies the distribution both of the liquid and of the solid phases, due to the swelling of the particles. Hence, to follow and characterise the process it is necessary to make use of a setup allowing the simultaneous measurement of the liquid and solid phases concentration. This is the dual-gamma ray absorptiometry, that has been previously used to analyse infiltration through porous media by Angulo-Jaramillo (1989), Moutier (1996) and Rolland (2002).

The measurements are made using two gamma radiation sources (^{241}Am and ^{137}Cs) and a detector that counts the number of photons passing through the soil specimen contained in a cell (Imbert *et al.* 2004, Figure 3-29). The radiation attenuation is linearly related to the amount of material within its path. To determine the attenuation of each gamma energy band through a porous media, Beer-Lambert type equations are used:

$$N^{Am} = N_0^{Am} \exp\left[-\left(\mu_s^{Am} \rho_s \theta_s + \mu_w^{Am} \rho_w \theta_w\right) x\right] \qquad [3.]$$

$$N^{Cs} = N_0^{Cs} \exp\left[-\left(\mu_s^{Cs} \rho_s \theta_s + \mu_w^{Cs} \rho_w \theta_w\right) x\right] \qquad [4.]$$

where N is the number of gamma photons having crossed the specimen counted in a given length of time (s^{-1}), N_0 is the number of gamma photons counted in the same length of time through the empty cell (s^{-1}), μ is the attenuation constant for the different phases (m^2/kg), ρ is the volumetric mass of each phase (kg/m^3), θ is the volumetric content of each phase, and x is the thickness of the porous medium (m). The subscripts stand for solid, s, and water, w. The effect of the air phase is neglected because it is insignificant with respect to the attenuations of the two other phases. The superscripts Cs and Am stand for the type of gamma source.

These two attenuation equations can be solved simultaneously if the measured intensities of the two gamma rays are independent.

The experimental setup consist of (Figure 3-30):

- a mobile platform holding both the radioactive sources and the detector;
- a gliding band that moves the cell from the preparation to the measurement area, so that to avoid the operator exposition;
- a fixed support for the cell between the source and the detector;
- a system to fix the location of the cell at a given position along *z* axis;
- a control and data acquisition system.

The sample is contained either in a cylindrical Plexiglas cell, for samples of density lower than 1.45 g/cm^3, or in a stainless steel cylinder with oblong Plexiglas apertures (Figure 3-31), for higher densities. Pistons on top and bottom of the cylinders keep constant the volume of the sample while allow its saturation through inlets. The activity of the sources employed, ^{241}Am and ^{137}Cs, limits the thickness of the porous material, that must be lower than 57 mm. For this thickness, the counting time is around 7200 s. The infiltration tests performed in oedometers (section 3.1.1) have shown the good representativity of samples of a thickness higher than 5 cm.

The pellets/powder mixtures have been hydrated from the bottom surface through a porous disc connected to a 1-m water column. Deionised, deaerated water has been used. The water intake has been measured as a function of time.

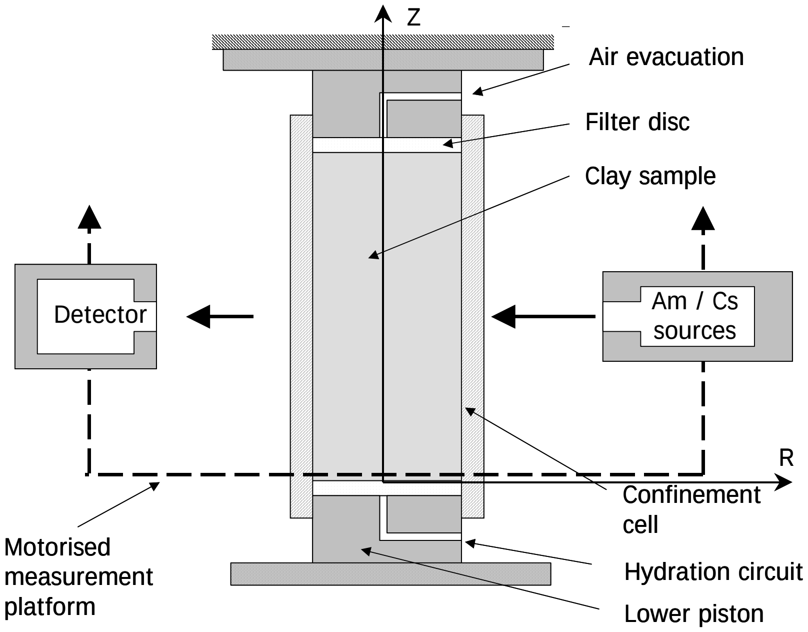

Figure 3-29: Schematic design of the setup to measure the gamma rays attenuation through bentonite.

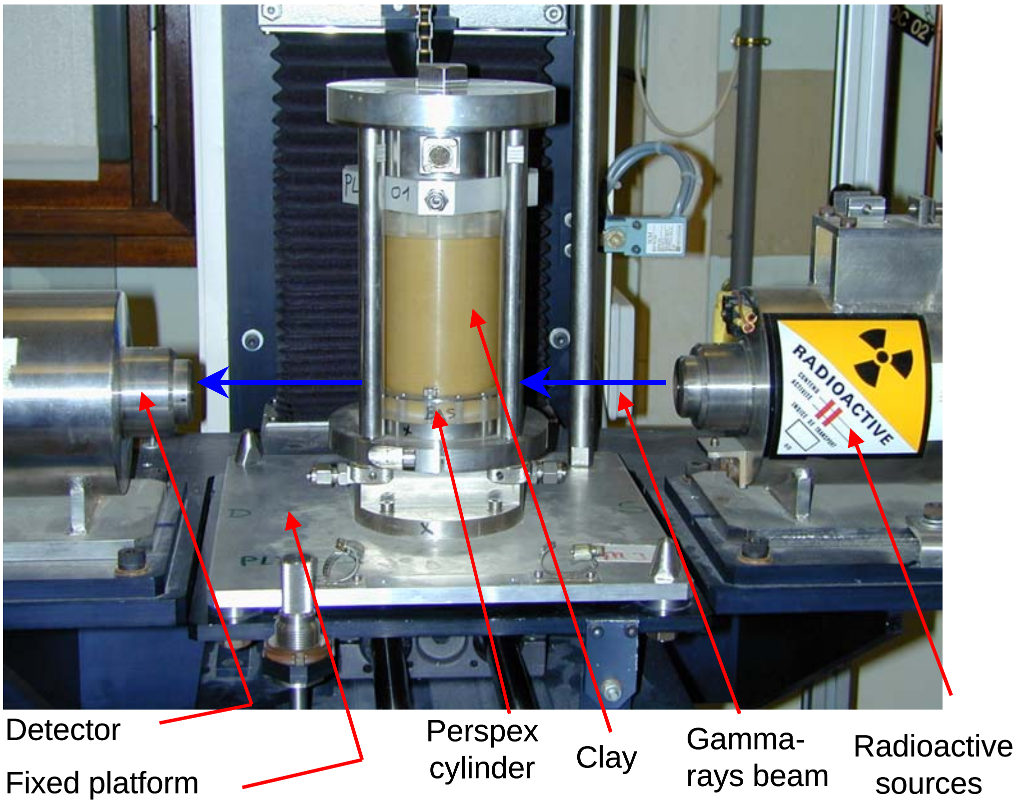

Figure 3-30: Experimental setup for infiltration tests with dual-gamma ray attenuation measurement.

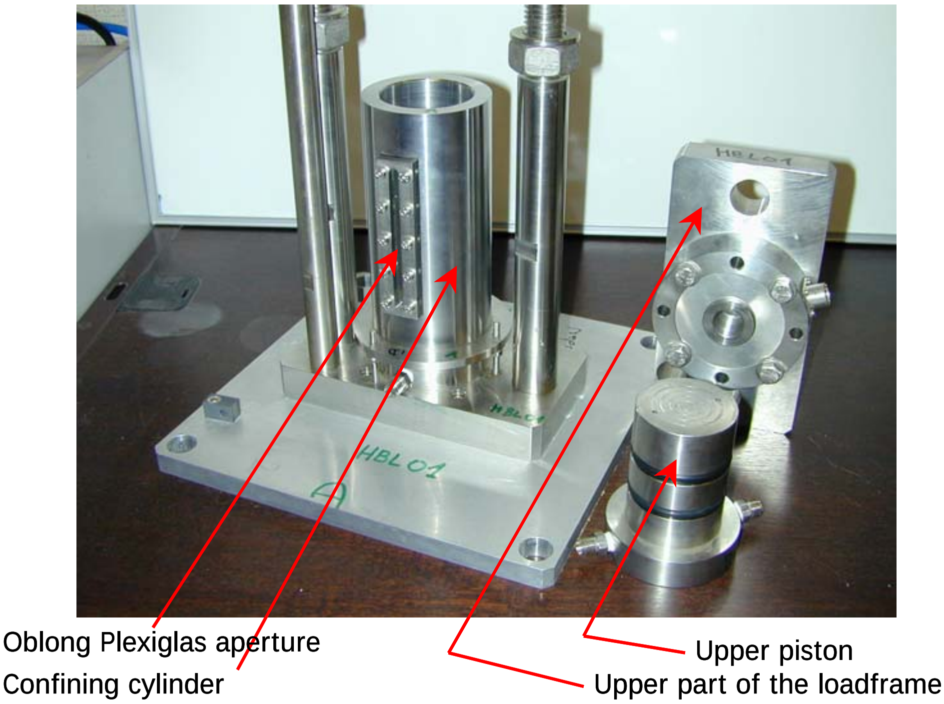

Figure 3-31: Infiltration cell for high-density samples

3.2.2 Results

Tests have been accomplished with 50/50 pellets/powder mixtures of dry density 1.30 (test BG2) and 1.60 g/cm^3 (test BG3).

3.2.2.1 Test with mixture of ρ_d 1.30 g/cm^3

The sample of dry density 1.30 g/cm^3 was manually manufactured by alternating powder and pellets layers up to a height of 11.3 cm. The periodic counting of photons has allowed the determination of water content and density along the sample at different times. The results are plotted in terms of water content, dry density and degree of saturation in Figure 3-32 to Figure 3-34. It can be observed that at the beginning of hydration, a sharp water front is developed. This front softens quickly, as the water content increase afffects the whole sample, although less intensely in the areas farther from the water source. That is, there is not a sharp limit between dry and wet areas. The sample reaches a homogeneous saturation after 221 days.

The dry density presents initially disparate values due to the natural heterogeneity of the mixture, which is accentuated by the small diameter of the cell. Nonetheless, hydration induces an equilibration of these values, reducing the higher densities and increasing the lower. The dismantling of the test after 491 days of hydration has allowed the visual checking of this homogeneity.

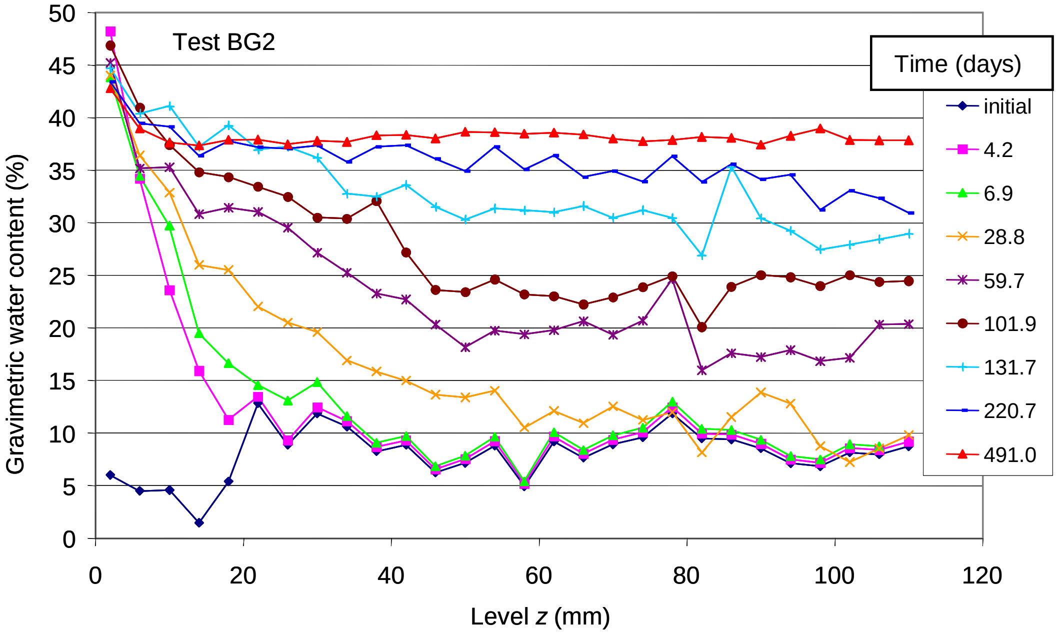

Figure 3-32: Evolution of water content at different levels of a sample of ρ_d 1.30 g/cm^3 during infiltration.

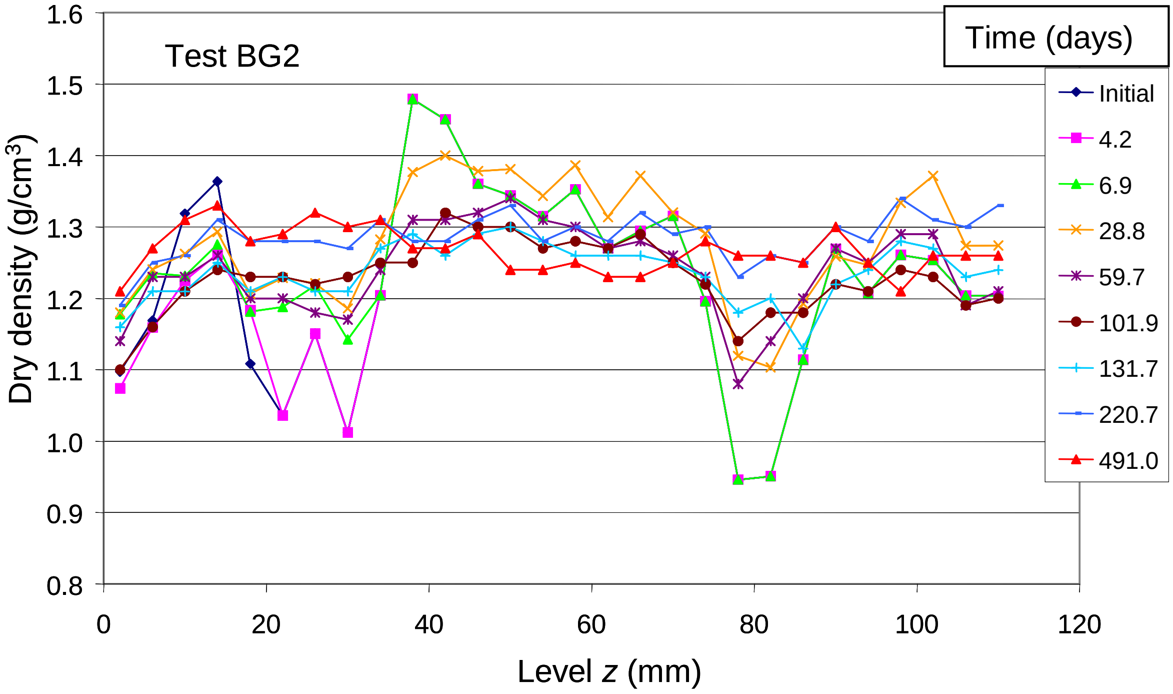

Figure 3-33: Evolution of dry density at different levels of a sample of ρ_d 1.30 g/cm^3 during infiltration.

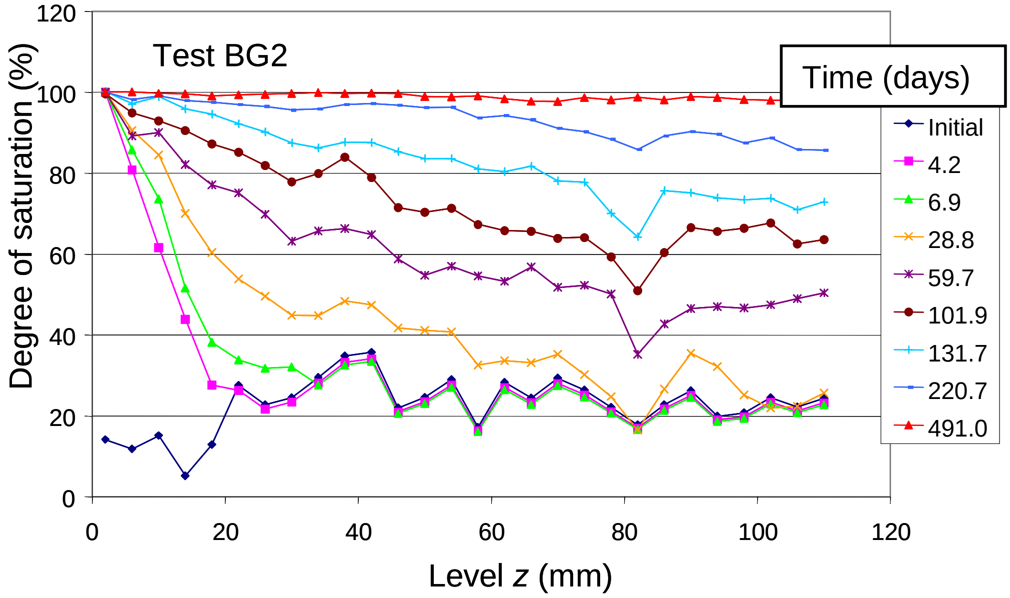

Figure 3-34: Evolution of degree of saturation at different levels of a sample of ρ_d 1.30 g/cm^3 during infiltration.

3.2.2.2 Test with mixture of ρ_d 1.60 g/cm^3

Test BG3 was performed with a sample of dry density 1.60 g/cm^3 obtained by compaction of the pellets/powder mixture (arranged in alternating layers) with a uniaxial pressure of 8.9 MPa. The height of the sample obtained was 8 cm. Due to an acquisition problem, it was not possible to translate the counts into density or water content values. However, the counts profiles along the sample for different times (Figure 3-35 and Figure 3-36) give information on the kinetics of the mixture homogenisation. From these curves, the following conclusions can be drawn:

- Hydration gives place to the homogenisation of the material, as revealed by the attenuation of the differences in gamma rays absorption.
- Hydration modifies very quickly the characteristics of the material all along the sample.
- The sample is almost saturated after 192 days of infiltration.
- From 276 days on, the homogenisation can be considered as rather good.

At the end of the tests the appearance of the material was homogeneous and no pellets could be distinguished. The blocks were sampled to determine the water content at eight levels by oven drying at 105°C. The average value was 27.7 ± 0.6 percent, being slightly higher near the hydration front.

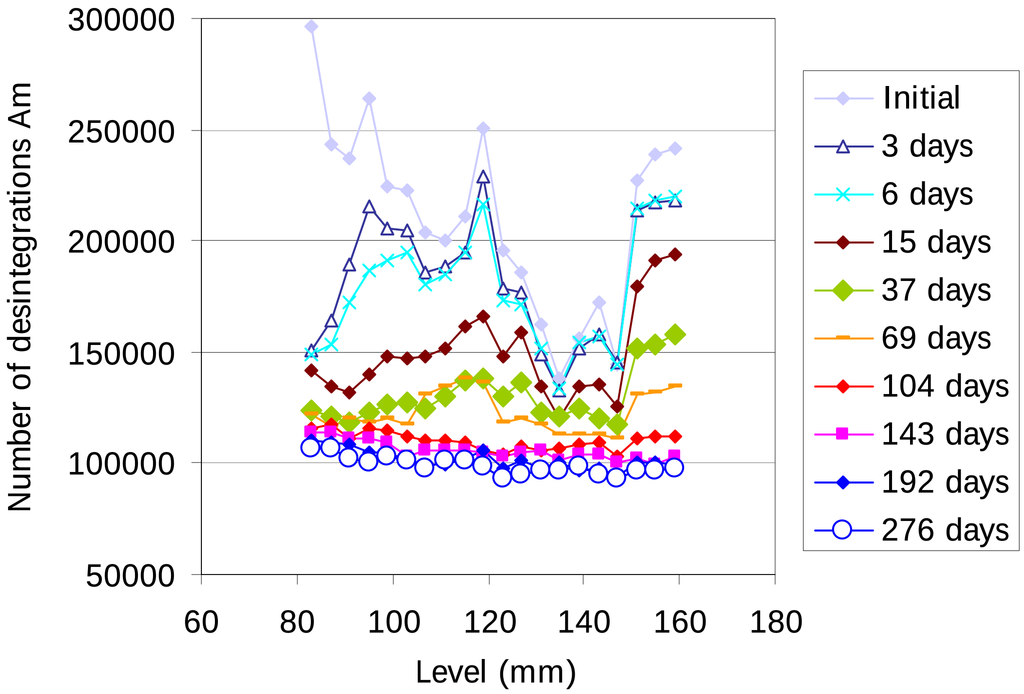

Figure 3-35: Absorption profiles of Am gamma rays in test BG3 (ρ_d 1.60 g/cm^3).

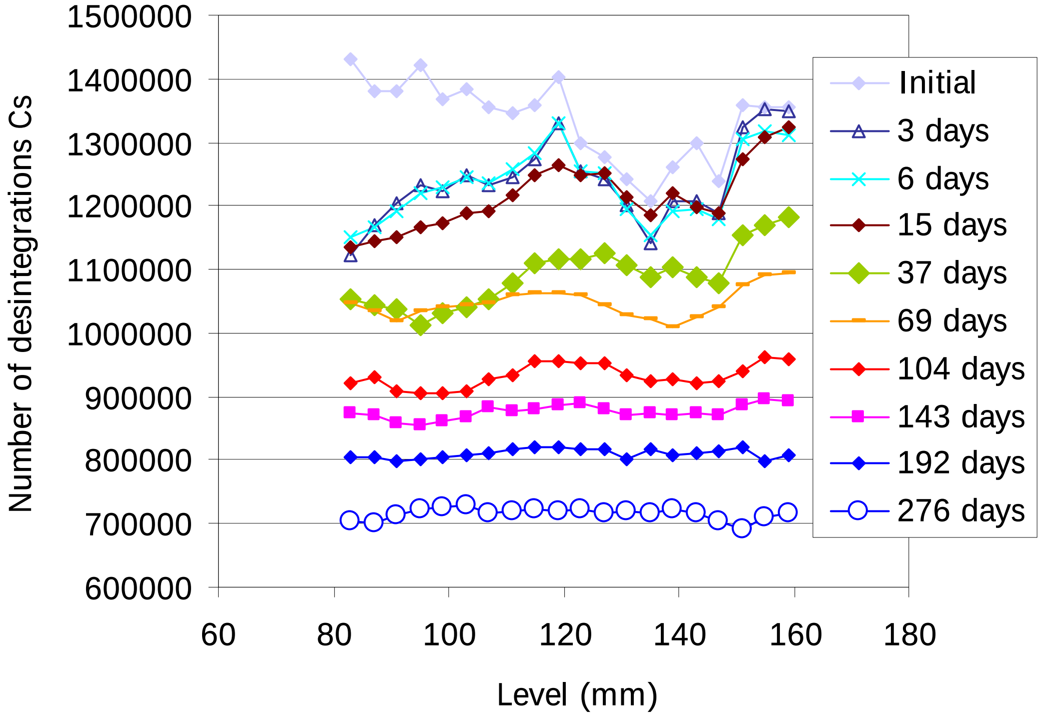

Figure 3-36: Absorption profiles of Cs gamma rays in test BG3 (ρ_d 1.60 g/cm^3).

3.3 Microfocus X-ray computer tomography (SCK·CEN)

Microfocus X-ray computer tomography (µCT) has been used to characterise the evolution of the FoCa clay pellets and powder mixture during hydration. This technique allows reconstructing a three-dimensional view of the sample in terms of density variations, which is very useful in order to follow the homogenisation of the mixture.

3.3.1 Methodology

3.3.1.1 Experimental setup

A Plexiglas, cylindrical cell (88 mm outer and 38 mm inner diameter) was designed with quick connectors at the bottom for water injection and gas escape routes at the top. A special holder was produced, allowing to move the cell for hydration and place it at exactly the same position within the microfocus X-ray tomography system at specified time intervals. A metal bar through the cell wall and plug ensured the constant volume of the cell.

The cell was filled with a mixture of 50 percent of pellets and 50 percent of powder (on a dry weight basis) and compacted to a dry density of 1.36 g/cm^3. The clay plug was 7.0 cm high and 3.8 cm in diameter. The water content of the 50/50 powder/pellet mixture was determined by drying samples in an oven at 105°C for 24 hours. The average water content was 5.7 percent. The expected swelling pressure for such a mixture is about 0.3 to 0.6 MPa (Equation 2). Assuming a solid particle density of 2.67 g/cm³ for FoCa clay, a theoretical porosity of 49 percent can be calculated. Consequently, the sample should have a bulk density of 1.85 g/cm³ at complete saturation.

The cell was filled in a well defined way to have a good control of the position of the pellets during the experiment. Figure 3-37 gives a schematic view of the position of the pellets within the Plexiglas cell.

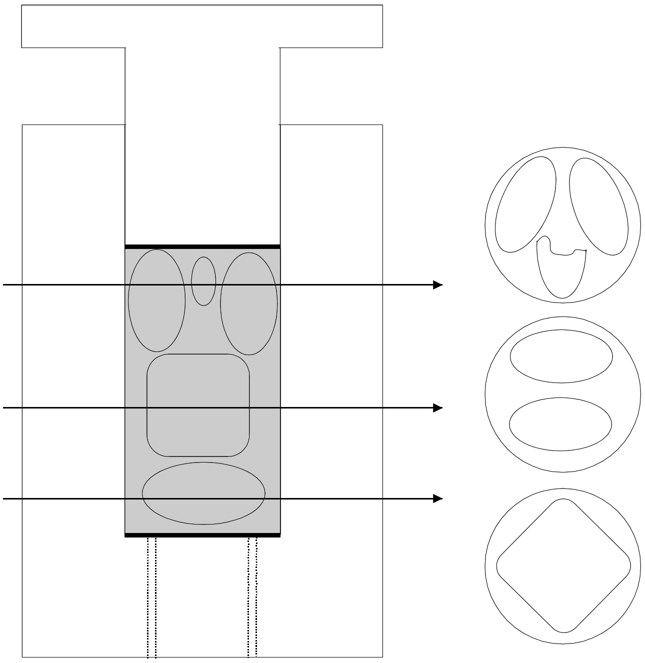

Figure 3-37: Schematic view of the Plexiglas cell with the orientation of the pellets. The grey colour corresponds to the position of FoCa clay (powder and pellets), whereas the black colour represents the position of filters.

3.3.1.2 Hydration scheme

The hydration was performed by connecting the quick-connectors to a bottle of EG/BS water. EG/BS is natural clay water collected from the Boom Clay and is believed to have a representative mean chemical composition of Boom Clay pore water (Table 3-11, De Craen *et al*. 2004). The cell containing the FoCa mixture was scanned in a dry state as a reference image. In the beginning the water was injected at a very low pressure, so that suction of the water by the clay was the dominant process. After two weeks of suction the sample was scanned. Afterwards the sample was injected once again at a very low pressure for one month and the sample was scanned a second time. Hereafter, the sample was injected at a pressure of 0.5 MPa. After one month of such an injection, the sample was scanned once more. The cell was then injected at a pressure of 0.5 MPa during three months. Finally, a permeability test under an injection pressure of 0.6 MPa was performed during two months. After reaching a constant flow it was concluded that the sample was fully saturated. Finally, the cell was dismantled, the bentonite mixture dried and scanned once again.

Table 3-11: Mean chemical composition of Boom Clay porewater (in mg/L), collected from the EG/BS piezometer, for major elements (concentrations above 1 mg/L) and pH

TOC [1]	TIC [2]	B	Ca	Fe	Mg	K	Si	Na	F	Cl	pH
89	187	7	4	1	3	9	2	410	3	26	9.4

[1] Total organic carbon
[2] Total inorganic carbon

3.3.1.3 Microfocus computer tomography instrument

To characterise this mixture of FoCa clay pellets and powder, the technique of microfocus X-ray computer tomography (μCT) is used. The technique has proven its potential for characterisation of mineralogy (Van Geet *et al*. 2000), fractures (Van Geet & Swennen 2001) and fluid flow (Roels *et al*. 2002). The technique uses X-ray projections of the same object at many different angles. All lines from such projections at a constant level through the object can be used to make a virtual slice through the object. Stacking several sequential slices allows reconstructing a three-dimensional view of the object. This principle is similar to the one used in medical CT instruments. However, a much better resolution can be achieved with microfocus X-ray computer tomography. These microfocus instruments have a very small focal spot size of the X-ray source, allowing to place the object near the X-ray source and capture X-ray radiographs of the object with a primary magnification. Consequently, the obtained resolution depends on the object size. Currently, the optimal resolution for objects of a few millimetres equals about 10 μm in three dimensions.

For the reconstruction it is necessary that the object always stays in the field of view, so that the borders of the radiographs are only passing air. These constant values are needed for a good reconstruction.

The visualised parameter with (micro) computer tomography is the linear X-ray attenuation coefficient. This parameter depends on the density and the atomic number of the object. In this study, a mixture of pellets and powder of the same bentonite is analysed. Since the pellets are produced by compacting the powder, the only difference between the components of the mixture is the density. As a rather constant value of atomic number can be assumed, the visualised parameter is actually related to density differences. Moreover, the linear attenuation coefficient depends on the used X-ray energy. As a whole spectrum of X-ray energies is used and as low X-ray energies are more attenuated, artefacts, especially beam hardening, may arise (Joseph 1981, Van Geet 2001). However, using metal foils that attenuate the low X-ray energies before they reach the object can minimise these artefacts (Van Geet 2001). In this study a foil of stainless steel of 1 mm thickness was used as filter. The effect of this filter was tested and revealed that the beam hardening artefact was negligible with this setup.

The reconstruction is based on calculating the attenuation out of the X-ray radiographs as

$$\mu=-\log(I/I_0) \qquad [5.]$$

with μ, the linear attenuation coefficient, I the measured X-ray intensity after passing through the object, and I_0 the measured X-ray intensity of unimpeded X-rays.

As mentioned, the object should always stay in the field of view to measure I_0 at any projection. Our Plexiglas cell has an outer diameter of 88 mm what would result in an optimal voxel (three-dimensional pixel) size of about 100 µm. The region of interest of the object, however, only has a diameter of 38 mm. Consequently, it was tested if we could zoom in on this internal diameter of the Plexiglas cell without losing any information. This would result in an adapted equation as follows:

$$\mu=-\log (I/I_m) \qquad [6.]$$

with I_m the measured X-ray intensity after passing through a fixed thickness of Plexiglas.

The reconstruction of this region of interest scanning was not a problem, as will be illustrated in the obtained images. The optimal voxel size was now about 55 µm. For quantification, however, it is necessary to have a good idea of I_m at any projection during any reconstruction. Therefore, an adapted reconstruction algorithm was developed to measure I_m at a fixed distance from the internal diameter and use this value instead of I_0.

The instrument used is a Philips X-ray radiograph with adapted tomography hard- and software of AEA technologies. During this study over longer time periods, the instrumental setup was kept constant. All used instrument parameters are given in Table 3-12. It should be noted that with the used instrument it is difficult to keep a constant distance between object and X-ray source and thus, it is difficult to achieve exactly the same pixelsizes within the reconstructed images. However, as the internal diameter within the object is constant at 38 mm, it was possible to correct any reconstruction image for small errors in resolution.

Table 3-12: Parameter settings used during every acquisition of the experiment.

Parameter	**Used during experiment**
Voltage	95 kV
Intensity	0.35 mA
Pixel size during acquisition	~55 µm
Centre of rotation	430-456 mm
Reconstruction algorithm	Filtered back projection
Reconstruction filter	Bracewell-Riddle filter
Size of reconstructed images	~800*800 pixels
Pixel size in reconstructed images	~55 µm

3.3.2 Results

3.3.2.1 Qualitative visualisation

First of all a μCT scan was made of the cell filled with the dry FoCa pellet/powder mixture to test the use of the technique. Figure 3-38 shows a slice through this sample. This illustrates that the difference between the pellets and the powder is clearly visible, due to a higher density of the pellets. Within the pellets, many fractures and microfractures are observed, probably related to the fabrication process. Within the mixture many high-density features are observed as well. These probably relate to iron oxy-hydroxides, which are identified within the FoCa clay (Gatabin & Rodrigues 1999). Within the powder surrounding the pellets, a lot of porosity, even macroporosity, is observed. The distribution of the porosity is not homogeneous, which is related to the sample preparation. Indeed, during filling of the cylinder with powder, the largest fragments tumbled in first, causing more macroporosity at the bottom of the sample.

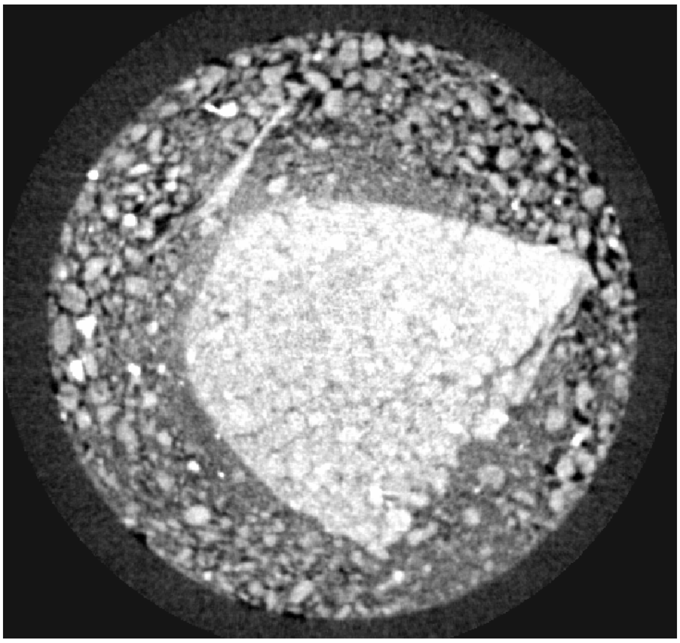

Figure 3-38: μCT slice through the cylindrical cell filled with a FoCa clay pellet/powder mixture. The high dense pellet is shown with a light grey to white colour, whereas air-filled porosity is shown black. At the border of the sample some macroporosity is visible, whereas in the pellet some fractures are seen.

3.3.2.2 Density calibration

For a quantitative analysis of the images, real density images would be much easier to interpret. For this purpose a good calibration has to be set up to convert the measured linear attenuation coefficients into density values. The measured linear attenuation coefficient depends on the density (ρ) and atomic number (*Z*) of the object and on the used X-ray energy (*E*) as

$$\mu = \rho\left(a + b\frac{Z^{3.8}}{E^{3.2}}\right) \qquad [7.]$$

with *a* and *b* instrument-dependent parameters (Van Geet *et al*. 2005).

When the whole sample is considered, the only change during hydration is the replacement of air originally present in the pores by water. From the density and atomic number of air and water (Table 3-13), it is clear that the difference in atomic number is negligible. Thus, when considering the whole sample, attenuation depends almost only on density. However, it should be noted that on a voxel scale, due to swelling of the clay, a calibration between attenuation and density is only valid when the calibration for dry clay and wet clay is very similar.

Table 3-13: Material constants and composition assumed for evaluation of X-ray mass attenuation coefficients (data from Hubbell & Seltzer 1996.)

Compound	**Atomic number**	**Density (g/cm^3)**	**Composition (*Z*: fraction by weight)**	
Dry air (near sea level)	7.37	$1.205.10^{-3}$	6:	0.000124
			7:	0.755268
			8:	0.231781
			18:	0.012827
Water	7.22	1	1:	0.111898
			8:	0.888102

For the calibration, FoCa clay powder was compacted to different dry densities and scanned within the same setup used for the hydration of the FoCa pellet/powder mixture. Next, these mixtures were hydrated and scanned again after saturation. Table 3-14 summarises the parameters of the calibration data used. Figure 3-39 illustrates the linear correlation obtained between measured attenuation coefficient and density (Van Geet *et al*. 2005). It is clear that a similar linear relation for dry and saturated samples can be applied.

Table 3-14: Calibration data of the linear attenuation coefficient versus total density.

Mass of clay (g)	**Dry density (g/cm^3)**	**Porosity**	**Status**	**Total density (g/cm^3)**	**Attenuation (cm^{-1})**	**Standard deviation (cm^{-1}·10^{-5})**
12.56	1.01	0.64	Dry	1.01	0.000968	22.90
15.01	1.20	0.57	Dry	1.20	0.001154	12.08
16.23	1.30	0.54	Dry	1.30	0.001262	18.35
17.41	1.40	0.50	Dry	1.40	0.001286	10.36

Mass of clay (g)	Dry density (g/cm^3)	Porosity	Status	Total density (g/cm^3)	Attenuation (cm^{-1})	Standard deviation (cm^{-1}·10^{-5})
19.92	1.60	0.43	Dry	1.60	0.001431	4.88
22.55	1.81	0.35	Dry	1.81	0.001574	5.69
24.70	1.98	0.29	Dry	1.98	0.001682	5.50
12.51	1.00	0.64	Saturated	1.64	0.001375	4.11
14.97	1.20	0.57	Saturated	1.77	0.001525	3.39
19.94	1.60	0.43	Saturated	2.03	0.001640	3.60
22.43	1.80	0.36	Saturated	2.16	0.001763	3.27
24.92	2.00	0.29	Saturated	2.28	0.001889	3.02

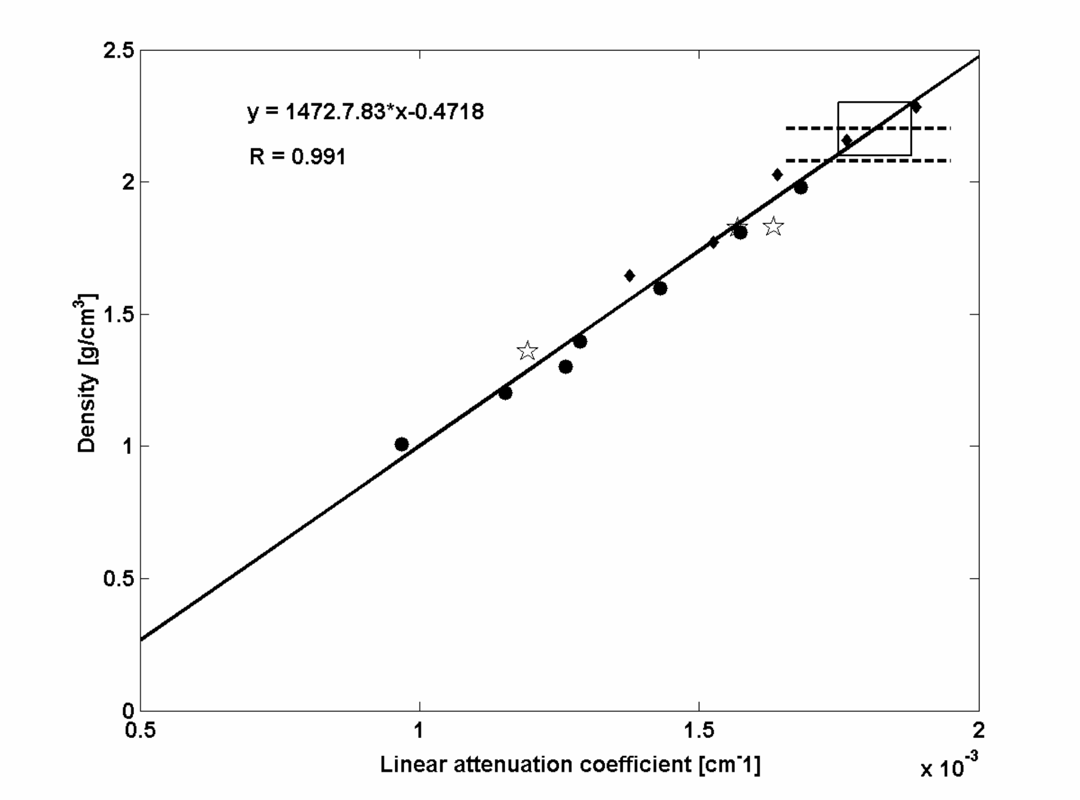

Figure 3-39: Correlation plot between linear X-ray attenuation coefficient and density for several calibration points of dry FoCa powder (circles) and saturated FoCa powder (diamonds) and the linear extrapolation (continuous line). Additional data points from the hydration experiment (Table 3-15) are also added (stars). The rectangle gives the range of measured attenuation coefficients of a dry pellet and the corresponding densities, based on the linear trend. The dashed horizontal lines give the range of experimentally determined densities of a dry pellet (Volckaert et al. *2000).*

As we are dealing with heterogeneous material, the standard deviation caused by the instrumental setup cannot be measured within one slice. However, assuming that one slice is representative for the mixture, the standard deviation between the mean attenuation of different slices can be used. However, there is a clear effect of heterogeneity for the sample of lowest density (see Table 3-14). For densities above 1.5 g/cm^3, the maximum variation in attenuation is $5 \cdot 10^{-5}$ cm^{-1}, corresponding with a standard deviation of about 0.08 g/cm^3. The 95 percent confidence interval of the linear fit between density and linear attenuation coefficient is also 0.1 g/cm^3. All calculated densities from µCT analyses will be rounded to 0.1 g/cm^3, which is good enough for the purpose of studying the macroscale homogenisation. Additionally, four data points with known densities from the hydration experiment of FoCa pellet/powder mixture are also plotted on the calibration curve (Figure 3-39). These points are:

- total density of the whole dry sample,
- total density of the whole sample before the permeability test,
- total density of the whole sample after the permeability test, and
- total density of a dry pellet.

Table 3-15 and Figure 3-39 summarise the characteristics of these points, indicating the good fit between our experimental points and the calibration curve.

Table 3-15: Characteristics of additional points used in the calibration density – linear attenuation coefficient

Description	**Attenuation (cm^{-1})**	**Density (g/cm^3)**
Whole dry sample	0.00121	1.44
Whole sample before the permeability test	0.00158	1.83
Whole sample after permeability test	0.00164	1.83
Dry pellet	0.00175 – 0.00188	2.08 – 2.20 [1]

[1] Volckaert *et al.* 2000

3.3.2.3 Quantitative visualisation

Figure 3-40 illustrates the changes observed after all hydration steps by the visualisation of one vertical slice through the centre of the cell. After two weeks of hydration at very low pressures (implying especially suction) a distinction between the pellets and the powder could still be made. However, the bottom pellet had a more diffuse border compared with the surrounding powder, illustrating that the density difference between both had decreased. The density images show that all pellets have lower density as a consequence of swelling. In the dry state mean densities of the pellets in this slice are between 1.9 and 2.1 g/cm^3, whereas after the hydration all pellets have density of about 1.85 g/cm^3. Despite this density decrease of all pellets, macroporosity is still present in the powder surrounding the top pellets. The mean density of the powder at the bottom has increased from about 1.0 g/cm^3 to 1.6 g/cm^3. The mean density of the powder at the top of the sample has not changed and is still around 1.3 g/cm^3.

The results of the second hydration phase, one month at a very low pressure, show that the pellets can still be distinguished. Now the mean density of the pellets has not changed, but the mean density of the powder at the bottom of the sample has increased from 1.6 to 1.7 g/cm^3 and the powder at the top of the sample has increased from 1.3 to 1.4 g/cm^3.

After these two phases of hydration at low pressure, an injection of water at about 0.5 MPa was performed. After one month of this injection, a homogenisation of the powder/pellet mixture was revealed. At first, the difference between pellet and powder has completely disappeared and the whole sample seems homogeneous. The whole sample now has a mean density of 1.8 g/cm^3. In the corners at the bottom of the sample, lower values are found around 1.63 g/cm^3. The rest of the sample shows variations between 1.7 and 1.9 g/cm^3. However, homogenisation is not complete, as at the bottom of the sample fractures within the mixture can be delineated (see section 3.3.2.4 and Figure 3-43).

The fourth hydration (second hydration phase at a pressure of 0.5 MPa) has not really changed the observations. The sample seems homogeneous. The whole sample now has a mean density of 1.8 g/cm^3. Apart from the corners at the bottom of the sample, this mean value only changes between 1.8 and 1.9 g/cm^3. At the bottom of the sample, the fracture outline is still present.

After the permeability test under an injection pressure of 0.6 MPa, a new scan was made. No structural change has been noticed, as the sample still seems homogeneous. The whole sample now has a mean density of 1.9 g/cm^3. Regions can be found with densities between 1.8 and 1.9 g/cm^3. The bottom corners of the sample are still somewhat lower in density (around 1.7 g/cm^3). However, the fracture outline at the bottom was no longer observed.

By subtracting the obtained images of Figure 3-40, it is possible to emphasise some of the features revealed as shown in Figure 3-41. After the first hydration, especially the bottom part of the sample is affected. However, all the pellets, even the top ones, seem to be affected as well. Around all pellets a rim of density decrease is noticed. Consequently, all pellets show some swelling, causing a general density decrease of the pellets as a result. After the second stage of hydration, especially a small increase of the density of the powder is noticed. After the first injection of water at 0.5 MPa, a more important density increase of the powder at the top of the sample can be seen, causing a homogenisation of the sample. The last stage of hydration and the permeability test have no geometrical effect on the sample, but result in some minor density increase of the whole sample.

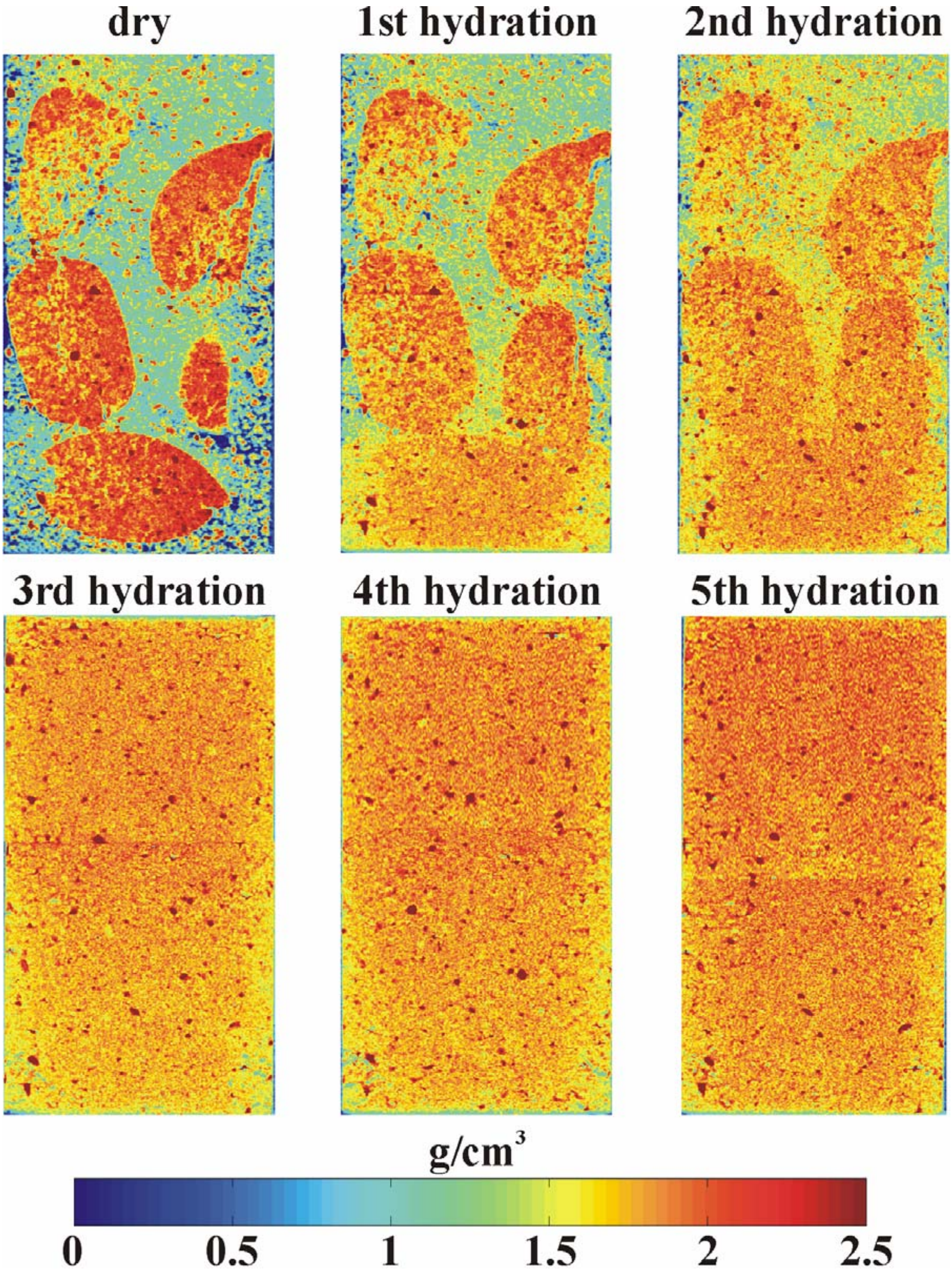

Figure 3-40: Recomputed vertical slices through the centre of the cell at every stage of hydration. By means of the correlation given in Figure 3-39, the attenuation coefficients are transformed into densities, made visible as colours. Width of the images is 38 mm.

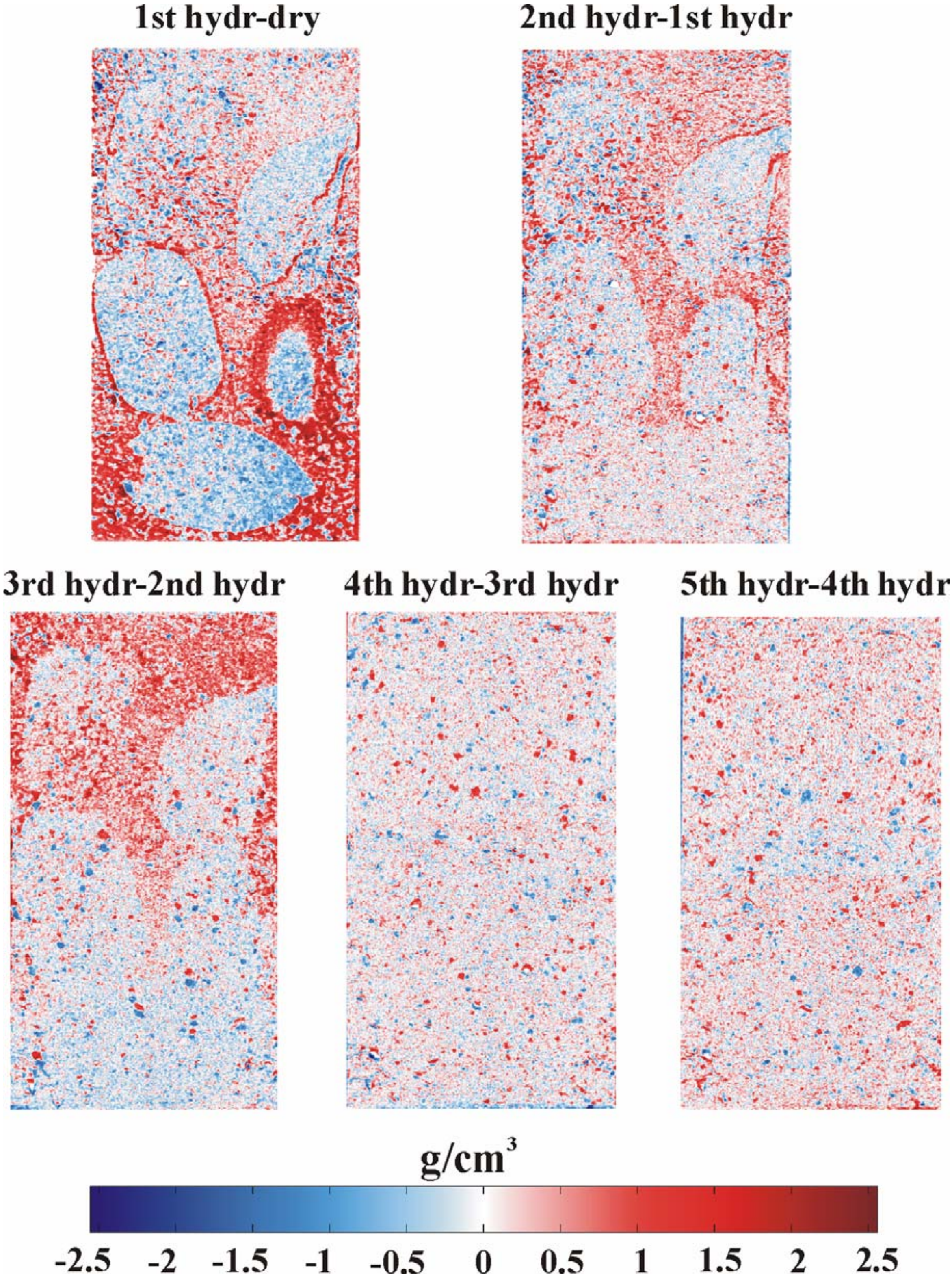

Figure 3-41: Images obtained after substracting the images given in Figure 3-40. In this figure the density changes can be clearly visualised as different colours. Note the red rims around all the pellets in the top left image, illustrating the swelling of the pellets from the beginning.

3.3.2.4 Swelling of pellets

After the first stage of hydration, fractures were noticed at the bottom of the sample. The question raised whether these fractures are related to the original position of a pellet. This was checked by manually delineating the fractures and the pellet in the same sequential slices. Next, the centroids of both features were measured in every slice and compared. The result is plotted in Figure 3-42 and shows that the centroid of both features follows the same trend. Consequently, it is concluded that these fractures occurred at the pellet/powder interface. This is visually confirmed by plotting the outline of the fractures on a vertical slice through the original dry sample (Figure 3-43). It is clear that the fractures are bordering the pellet, although they are always encompassing a larger volume of material. This is due to the swelling of the pellet during the hydration. Consequently, the swelling of the pellet can be visualised. The pellet/powder mixture of FoCa clay, thus, seems to have a memory of the original position of the pellets and the outline of the pellets is a weak point within the mixture, along which fractures are more easily developed. Since a distinction of the pellet is still possible, but the outline is larger than the original pellet, the technique allows to exactly measure the swelling of the pellets. Within 37 sequential slices the fractures were visible and the outline could be easily drawn. This part of the data was used for the measurement of volume increase due to swelling.

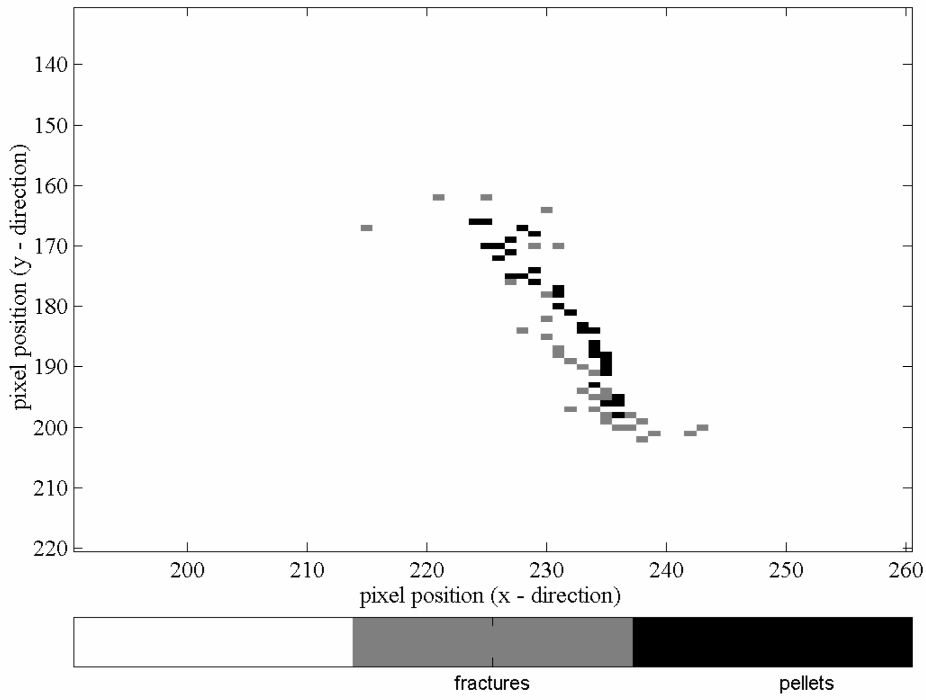

Figure 3-42: Evolution of the centroid in 37 sequential slices for the pictures illustrating the dry pellet and the pictures illustrating the fractures. The x *and* y *pixel position of both features are plotted. The evolution of the manually outlined features follows the same trend for both, indicating that the fractures are probably the outline of the swollen pellet.*

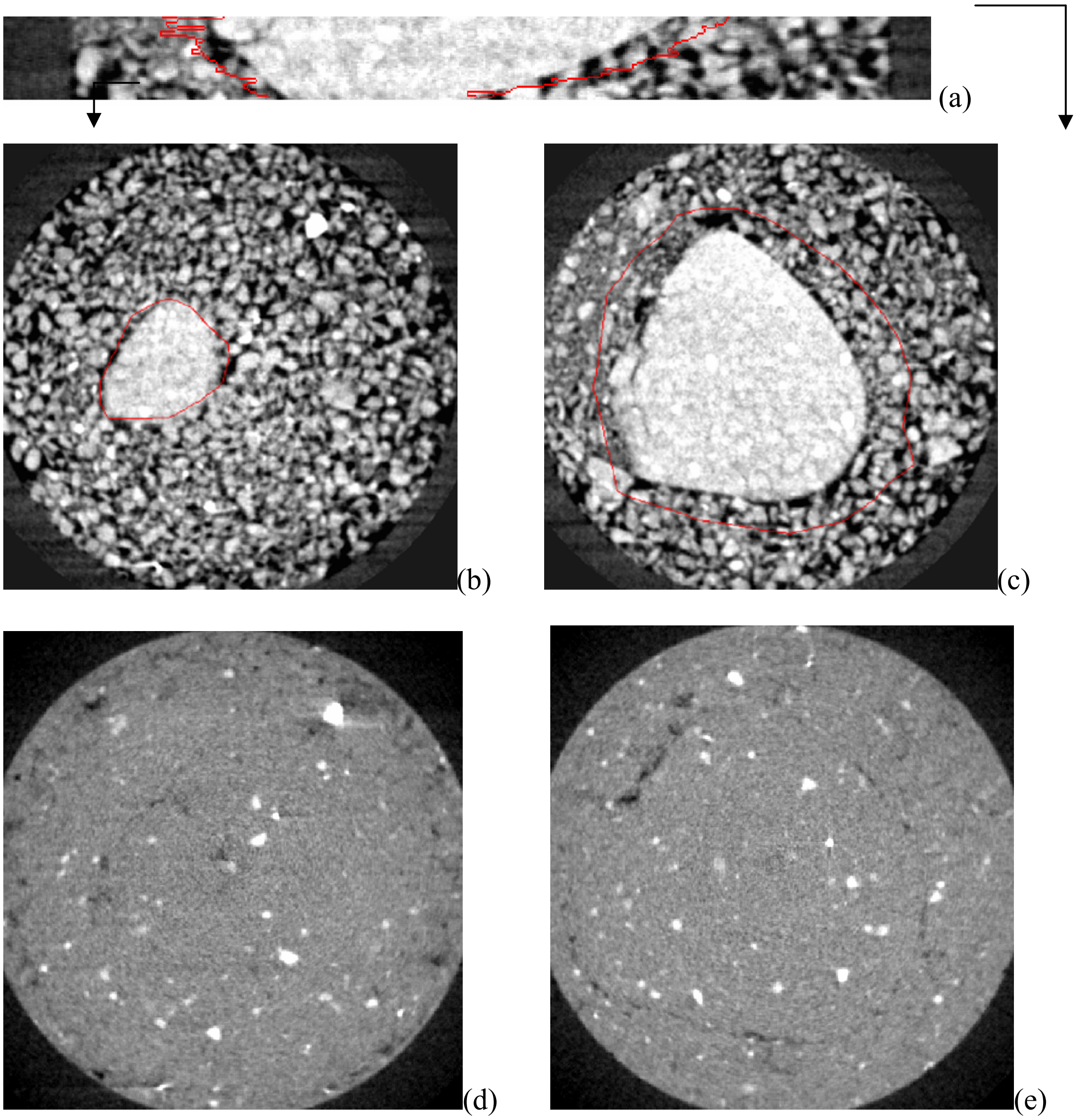

Figure 3-43: Recomputed vertical slice through the bottom pellet with the outline of the fractures noticed after an injection of water at 0.5 MPa in red colour. The bottom and top slice through this vertical profile are given in (b) and (c), respectively. The original slices used for the manual delineation of the red line in (b) and (c) are given in (d) and (e), respectively. Note that the fracture outline closely follows the pellet position, but is slightly larger, probably due to swelling.

Figure 3-44 shows the surface increase for each slice. A mean surface increase of 55 percent can be deduced. The analysed part of pellet had a volume of 631 mm^3, whereas the fracture encloses a volume of 972 mm^3, corresponding to a volume increase of 54 percent. It should be noted that only part of the pellet (where fractures were present) has been used to calculate the volume increase. This certainly is only an estimate of the volume increase, since volume increase is not constant over the whole volume analysed (Figure 3-44). However, to our opinion this is the only technique to directly measure the volume increase. Future research might try to link these results to pressure evolution measurements. A possible explanation of the creation of this fracture might be due to experimental handling. Before performing the µCT scanning, the sample is disconnected from the water injection system. In practice, this occurred about 16 hours before scanning. As saturation is not yet complete, suction of the higher density pellets is still going on, creating a flux of water from the wettest zone towards drier zones. This might explain the fact that fractures are only found in the bottom of the sample and the fact that the fractures were only found before the complete saturation.

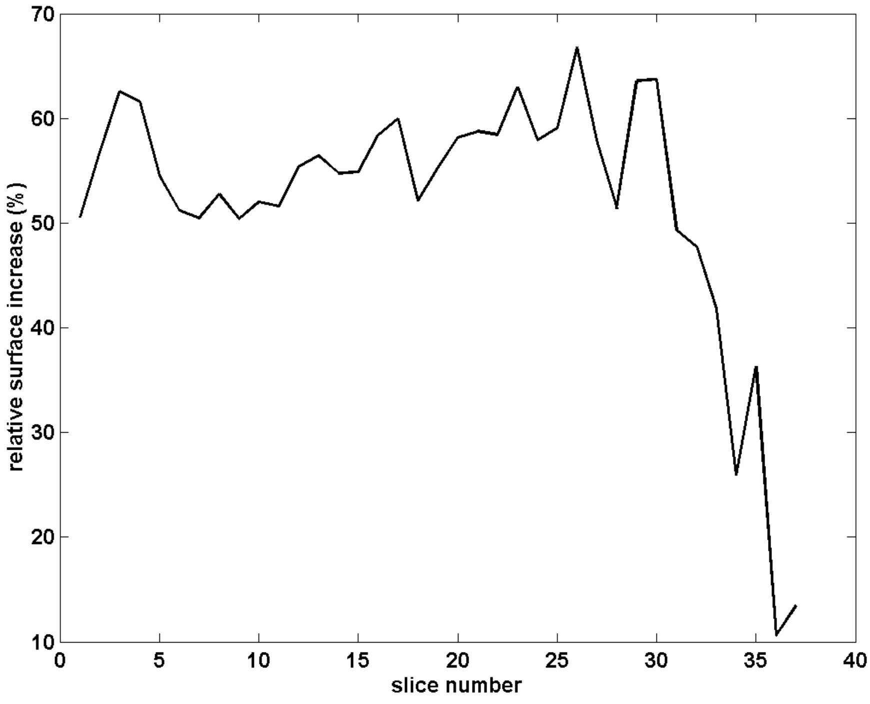

Figure 3-44: Measured surface increase in 37 sequential slices, corresponding to a mean volume increase of 55 percent.

3.3.2.5 Destructive tests

After all non-destructive measurements, the cell was dismantled. The extracted sample and also a small subsample of the bottom pellet were measured for their water contents by means of oven-drying. Water contents of 37.9 and 41.2 percent were measured in the whole sample and pellet, respectively. Assuming a solid particle density of the FoCa material of 2.67 g/cm^3 and a water density of 1.00 g/cm^3, a theoretical water content for full saturation of 36 percent is calculated. This is coherent with the water content measured in the whole sample if we take into account the higher density of the water adsorbed in the bentonite (see section Material).

After drying, the whole sample was broken in two half cylinders and showed several fractures. Both parts were scanned once again to visualise the 3D-distribution of the fracture pattern and to compare this with the original position of the pellets. However, all fractures seemed to be oriented randomly and no correlation with the original pellet position was found by visual inspection (Figure 3-45).

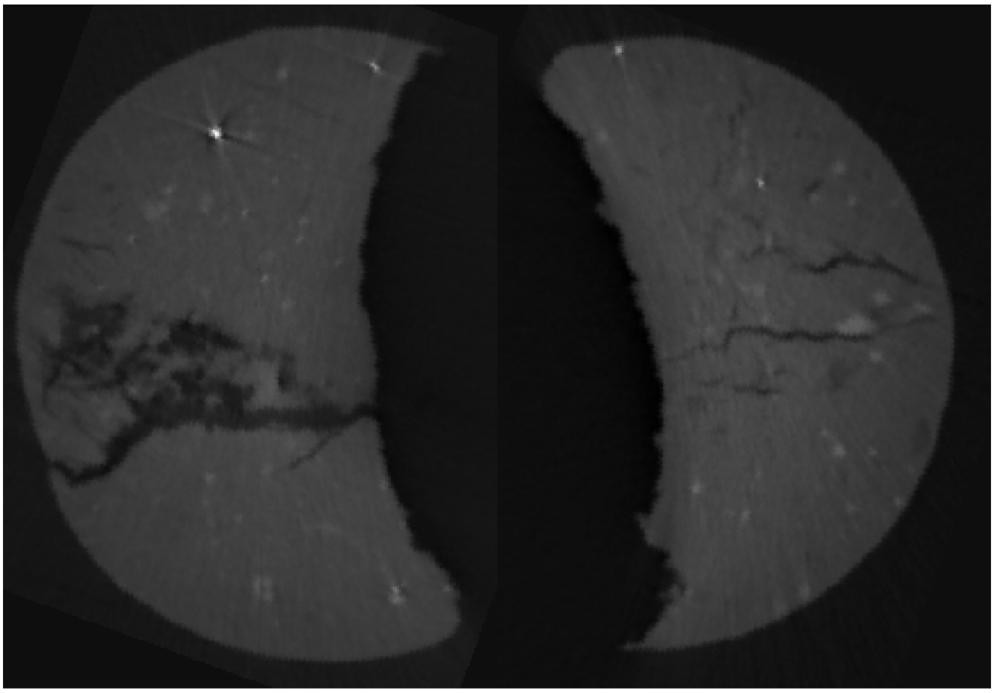

Figure 3-45: µCT slice through the object after drying the saturated object. As the object was split into two parts, both parts were scanned separately.

3.3.3 Discussion

The µCT results show that during the first hydration step the macropores present within the object at a dry state have disappeared. However, some macroporosity is still present within the powder. Moreover, it is clear that water affected the mixture especially in the neighbourhood of the pellets compared to the zones with only powder. The preferential suction of the pellets might be attributed to the capillary active pores in the pellets (see pore size distribution in Figure 2-2), which are not present in the FoCa-powder. The low compaction of the FoCa powder results in macropores for which capillary suction is negligible. Consequently, the pellets are first affected by the hydration. After the first injection at 0.5 MPa, a homogenisation took place. Also in the subtraction images we can notice a slight density loss of the pellets and a density increase of the powder. The last stages up to saturation only have an effect on the density, but do not cause any structural changes.

Apart from the density changes, the µCT images also revealed the occurrence of fractures at the bottom of the sample. The fractures are probably related to the suction of high-density zones, while the sample is disconnected from the water injection system during scanning. The occurrence of the fractures, however, gave the unique opportunity to measure the swelling of a pellet, due to the hydration.

The images do show lower densities at the bottom corners of the sample. Probably, the injection of water through the filter plate cannot be assumed as a straight front injection. Consequently, whenever modelling such experimental data, the boundary conditions need to be carefully chosen, to avoid large inconsistencies.

4 MIGRATION PARAMETERS OF SEALING MATERIALS

The migration of radionuclides in clays is controlled by diffusion, what makes necessary the determination of radionuclides diffusion coefficients, as well as of their accessible porosity. This has been undertaken at CIEMAT and SCK·CEN laboratories. The behaviour of the neutral and conservative tritium and of the conservative anionic species iodide has been analysed in pellets/powder mixtures and in compacted powder.

4.1 Diffusion tests by CIEMAT

CIEMAT has performed through-diffusion and saturation tests with tritium and iodide in pellets/powder mixtures of different dry density and in compacted powder, in order to determine the effective diffusion coefficients and the accessible porosity for these species. To deepen in the understanding of the anionic exclusion phenomena, some saturation tests were performed also with chloride.

4.1.1 Methodology

The experiments have been performed in stainless steel cells that have to resist the swelling pressure of the confined clay and guarantee the correct density of the compacted clay (Figure 4-1). The diffusion cells have a cylindrical body where the clay is compacted. The cells are assembled by attaching a plate on top and bottom of the cell, tightened with bolts to seal the cell. Each cell plate is connected with tubes to reservoirs through a peristaltic pump. Figure 4-2 shows the body and plates of a disassembled diffusion cell. Polyethylene porous filters of average pore diameter 40µm are placed between the compacted clay plug and the steel plates.

A 50/50 pellets/powder mixture of FoCa clay was used in the experiments, being prepared by placing alternated layers (three layers of powder and two of pellets) inside a stainless steel ring. The process of sample preparation can be seen in Figure 4-3.

The mixture was uniaxially compacted inside this ring at different clay densities between 1.33 and 1.50 g/cm^3. Other tests were carried out using only the FoCa powder compacted at different densities. After the compaction, the clay plugs (diameter 10 cm and thickness approximately 3 cm) were sandwiched between porous filters.
The water used for the clay saturation was synthesised on the basis of the composition of the Boom clay pore water, in order to have the same conditions of the *in situ* experiment (Volckaert *et al.* 2000). The water chemical composition is shown in Table 4-1. When the water saturation process finished, the cells were used for diffusion or saturation experiments. The experiments were done at room temperature, 20-25ºC.

Water from the reservoir is passed over both sides of the cell, across the filters, and circulated slowly to the reservoir using a peristaltic pump. The clay takes up the water by suction through the filters. The mass of the water in the reservoir was periodically checked until a constant mass with time was obtained. For powder/pellets mixture plugs the full saturation was reached in about three months.

To know if the dissolution of salts from FoCa clay could have modified the water composition, the chemical composition of the water after finishing the saturation was analysed (Table 4-1). The minor dissolution of salts observed should not modify the diffusion processes of conservative tracers.

Figure 4-1: Diffusion cell.

Figure 4-2: Disassembled diffusion cell. The clay plug is between the polyethylene filters.

Figure 4-3: Preparation of powder/pellet clay plug (second pellets layer).

Table 4-1: Chemical composition of synthetic Boom clay water (initial and after three months of contact with the FoCa clay).

Constituent	**Synthetic Boom clay water (mmol/L)**	
	Initial composition	**Final composition**
F^-	0.26	0.27
Cl^-	0.73	0.73
I^-	<0.02	<0.02
SO_4^{2-}	0.002	0.029
B	0.74	0.79
Na^+	13.5	14.4
K^+	0.36	0.33
Mg^{2+}	0.13	0.12
Ca^{2+}	0.06	0.05
Total alkalinity (mg HCO_3^-/L)	868	865
Conductivity (mS/cm)	1.20	1.25
pH	8.6	9.0

Once saturation reached, the through-diffusion experiments started. The tracers used were tritium HTO (0.9 nCi/mL), selected as tracer in order to investigate the behaviour of a conservative (that do not present retention or interactions with the solid phase) and neutral species tracer, and iodide as NaI (0.01 *M*), to study the behaviour of conservative and anionic species. Diffusion of anionic species in compacted clays can be affected by electrostatic forces between the negatively charged clay surface and the anions, this phenomenon being called anionic exclusion, since it results in a smaller volume of pore water available for their transport. $^{36}Cl^-$ has been used in a test of saturation to demonstrate that anionic exclusion effects actually exist in the bentonite. HTO and $^{36}Cl^-$ were measured using a Packard 2700 TR liquid scintillation counter, and the iodide by means of an ion selective electrode technique (detection limit: 20 μg/L).

The data from HTO ($t_{1/2}$ = 12.3 years) samples must be corrected for radioactive decay. This correction is not necessary for ^{36}Cl samples because its half-life ($3.01 \cdot 10^5$ years) is lengthy in comparison with the experimental time.

4.1.1.1 Through-diffusion experiments

Through-diffusion experiments with constant concentration gradient were used for the determination of the effective diffusion coefficients. The compacted and saturated clay plugs are placed between two reservoirs: the in reservoir, where the tracer is added, and the outlet reservoir, where the measurements are carried out. The water in both reservoirs is continuously stirred, by means of a peristaltic pump, to obtain a homogeneous solution. Figure 4-4 shows a schematic representation of the through-diffusion setup.

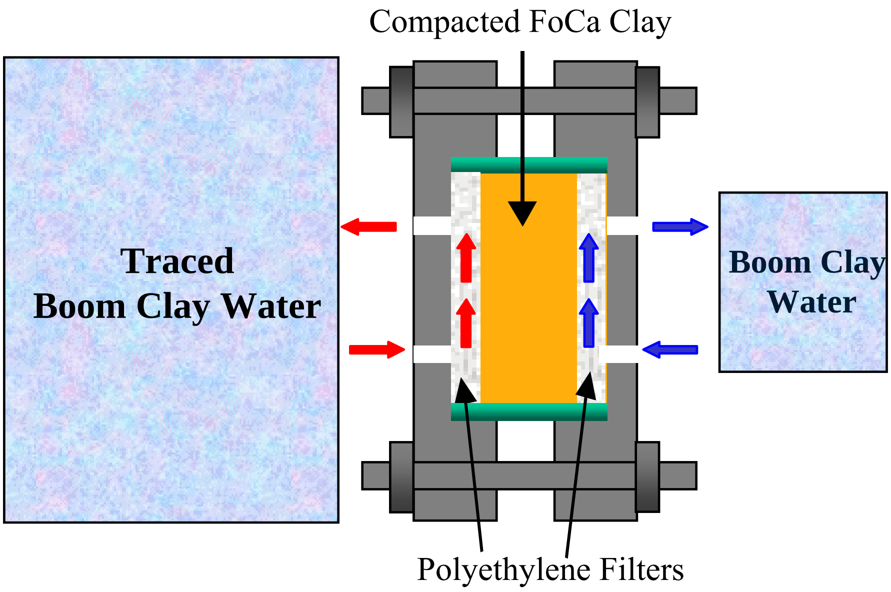

Figure 4-4: Schematic representation of through-diffusion test.

Experimentally, the constant gradient is obtained using a high volume in the in reservoir (1 L) and smaller volume in the measurement reservoir (100 mL), which is periodically replaced. This configuration ensures that concentration in the in reservoir remains practically constant and the concentration in the outlet reservoir close to zero. Figure 4-5 shows the actual aspect of the diffusion experiments, the big bottles correspond to the traced reservoir (in this form the concentration remains constant) and the small bottles to the measurement reservoir.

Figure 4-5: Diffusion experiments in progress: diffusion cells connected to the reservoirs.

For this experimental setup the following initial and boundary conditions exist:

$t > 0$ $C\,(x = 0, y, z, t) = C_0$ (C_0= constant)

$C\,(x = L, y, z, t) = 0$ (L = sample thickness)

$C\,(\mathrm{x}, y, z, t = 0) = 0$

An analytical solution for the diffusion equation with the above mentioned conditions is given by Crank (1975):

$$Q = A \cdot L \cdot C_0 \left[\frac{D_e}{L^2} t - \frac{\alpha}{6} - \frac{2\alpha}{\pi^2} \sum_1^{\infty} \frac{(-1)^n}{n^2} \exp\left(\frac{-D_e n^2 \pi^2 t}{L^2 \alpha} \right) \right] \qquad [8.]$$

where Q is the cumulative mass of tracer that has reached the outlet reservoir, A the cross sectional area of the clay plug, L the sample thickness, C_0 the tracer concentration in the in reservoir, D_e the effective diffusion coefficient, α is the capacity factor, $\alpha = \phi + \rho_d K_d$, equivalent to the accessible porosity, ϕ, for non-sorbing (conservative) tracers ($K_d = 0$), and ρ_d the clay dry density. For long times a steady-state condition is reached, the exponential terms tend to zero and the Equation 8 becomes:

$$Q = A \cdot L \cdot C_0 \left[\frac{D_e}{L^2} t - \frac{\alpha}{6} \right] \qquad [9.]$$

The diffusion process is initially characterised by a transient period, which develops gradually with time, until the tracer flux through the sample becomes constant and reaches the steady state. The curve of the cumulative solute recovery in the outlet reservoir *vs.* time, at the steady state, is a straight line. The slope of this straight line provides the effective diffusion coefficient, and from the intercept of this straight line with the time axis the accessible porosity can be calculated ("time-lag" method).

4.1.1.2 Saturation experiments

Saturation experiments provide an alternative, and more precise, method to measure the accessible porosity for a tracer in a porous media. Saturation experiments were performed using the same setup design than in through-diffusion experiment, except that both sides of the clay plug were left in contact with a single, continuously stirred, reservoir. The tracer (HTO) was added to the reservoir, and the concentration in the water was periodically measured. These experiments are intended to obtain a constant concentration profile in the clay plug. In order to ensure that the concentration profile into the plug is effectively constant, the concentration in the saturation solution is periodically monitored until a constant concentration is measured. After the experiment, the plug is sliced and each slice weighted to determine its volume. The clay slice is then introduced in centrifuge tube and a volume of water is added. The tubes are kept in continuous stirring during three days and then the sample is centrifuged (12000 rpm, 15 min). After centrifugation, the activity in the supernatant is measured. When the experiment finishes, tracer concentration in the saturation solution is equal to the tracer concentration in the pore water of the bentonite plug, and the following equation can be used:

$$A_F = V \cdot C_R \cdot \phi \qquad [10.]$$

where A_F is the activity in the bentonite slice, V the volume of the slice, C_R the concentration in the reservoir, and ϕ the accessible porosity. Each slice provides a value of the accessible porosity, which allows calculating a mean value and its error from a single experiment.

As will be shown in the next section, the accessible porosity for the anionic iodine was found to be significantly smaller than that of HTO at the same clay density. For this reason, anionic exclusion effects were also investigated by means of experiments in which $^{36}Cl^-$ was placed in the hydration water in contact with a non saturated sample of powdered FoCa bentonite compacted at dry density of 1.26 g/cm^3. The initial water content of the FoCa clay was 7.3 percent. The clay suctioned the $^{36}Cl^-$ - traced water and periodically, the volume of the saturation water and the $^{36}Cl^-$ concentration were measured in the reservoir.

4.1.2 Results and discussion

4.1.2.1 Through-diffusion

Several experiments have been performed in order to obtain the diffusion coefficient of powder/pellets clay mixtures, and to study the accessible porosity and the anionic exclusion phenomena. Table 4-2 summarises the test performed.

Table 4-2: Summary of the through-diffusion tests performed.

Test	**Material**	ρ_d (g/cm^3)	**Test**	**Tracer**	**Experimental time (days)**		
					Hydration	**Diffusion**	**Saturation**
C-65	Mixture	1.37	Diffusion	HTO	105	100	-
C-66	Mixture	1.33	Diffusion + Saturation	HTO	105	100	123
C-67	Mixture	1.43	Diffusion	HTO	105	100	-
C-68	Mixture	1.46	Diffusion + Saturation	HTO	105	100	123
C-69	Mixture	1.34	Diffusion	Iodide	105	200	-
C-70	Mixture	1.43	Diffusion	Iodide	105	200	-
C-71	Mixture	1.49	Diffusion	Iodide	105	200	-
C-72	Mixture	1.49	Diffusion	Iodide	105	200	-
C-73	Mixture	1.34	Check Saturation	-	90	-	-
C-74	Mixture	1.49	Check Saturation	-	100	-	-
C-75	Mixture	1.41	Diffusion	HTO	180	87	-
C-76	Mixture	1.50	Diffusion	HTO	180	87	-
C-99	Powder	1.25	Diffusion + Saturation	HTO	72	94	69
C-100	Powder	1.26	Diffusion + Saturation	HTO	72	94	69
C-101	Powder	1.38	Diffusion + Saturation	HTO	72	98	69
C-102	Powder	1.39	Diffusion + Saturation	HTO	72	98	69
C-113	Powder	1.26	Saturation	^{36}Cl	-	-	30

Before beginning the diffusion experiments with clay pellet/power mixtures, in order to confirm a correct saturation, two clay plugs (C-73 and C-74), with dry density of 1.34 and 1.49 g/cm^3, were sliced and the water content was determined, by oven drying. These plugs showed a full saturation, with water content of 37.0 percent (1.34 g/cm^3) and 29.5 percent (1.49 g/cm^3), and the pellets were not visually discernible. A picture of the plug after saturation can be seen in Figure 4-6.

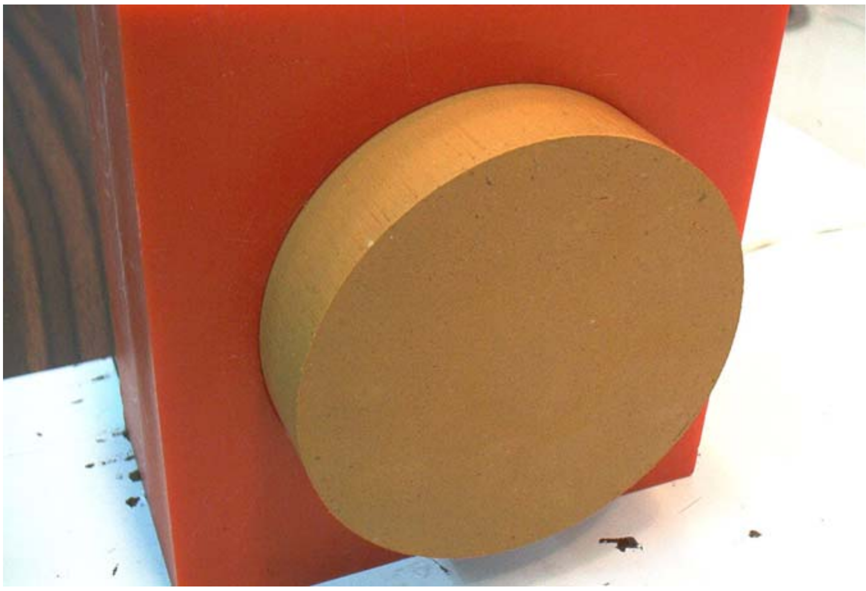

Figure 4-6: Homogeneous aspect of the powder/pellets clay plug after hydration.

Figure 4-7 shows an example of the experimental results in through-diffusion experiments with powder/pellets clay mixtures for HTO and Figure 4-8 for iodide. The lower figures present the flux entering the outlet reservoir, and the upper figures present the cumulative amount of tracer (time integral of the flux) that passed to the outlet reservoir. The linear fit in the steady state region, from which the effective diffusion coefficient and the time lag can be obtained, is shown. As mentioned before, the effective diffusion coefficient is derived from the slope of the straight-line obtained by linear regression of those data collected under the steady-state conditions, *i.e*. when the flux is constant. The figures clearly show that for iodine it takes longer than for HTO to reach the steady state regime.

Figure 4-9, Figure 4-10 and Table 4-3 summarise all the HTO and iodide diffusion tests carried out with compacted powder/pellets clay mixtures at different densities. HTO experiments (Figure 4-9) were carried out at 1.33, 1.37, 1.43 and 1.46 g/cm^3, whereas iodide experiments (Figure 4-10) were carried out at 1.34, 1.43 and 1.49 g/cm^3. The effective diffusion coefficient for HTO varied between $5.0 \cdot 10^{-11}$ and $2.0 \cdot 10^{-11}$ m^2/s decreasing when the dry density increased. This behaviour is associated with changes in the porous structure of the clay plugs and a decrease in the total porosity. In fact an increase in the density produce higher tortuosity and, for this reason, lower tracer mobility (Sato *et al*. 1993).

The effective diffusion coefficient for iodide varied between $3.0 \cdot 10^{-12}$ and $5.8 \cdot 10^{-13}$ m^2/s from lower (1.34 g/cm^3) to higher dry densities (1.49 g/cm^3). Later, two new experiments were carried out with HTO, C-75 and C-76, and similar results were obtained.

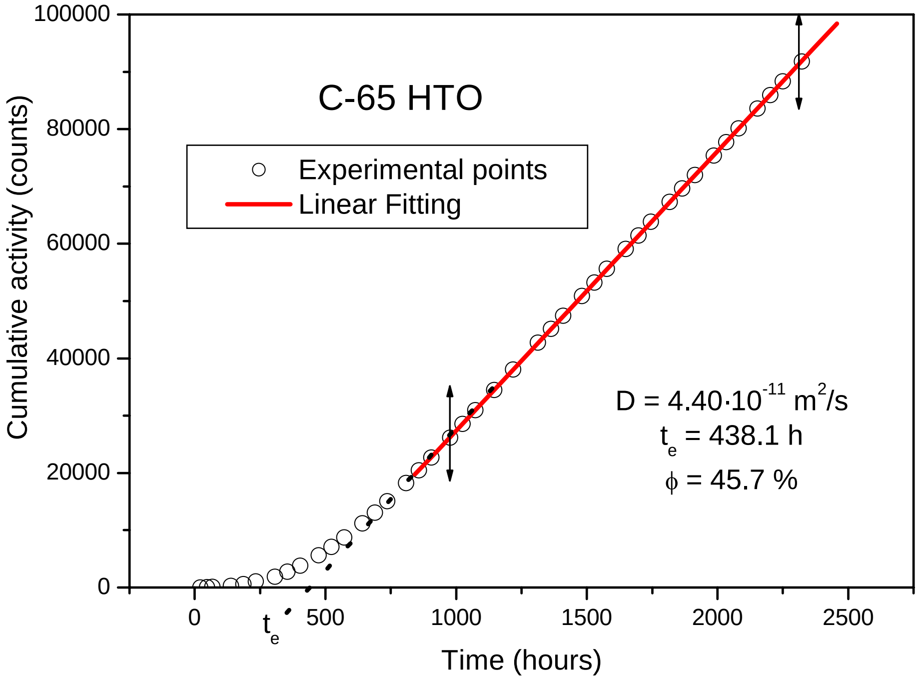

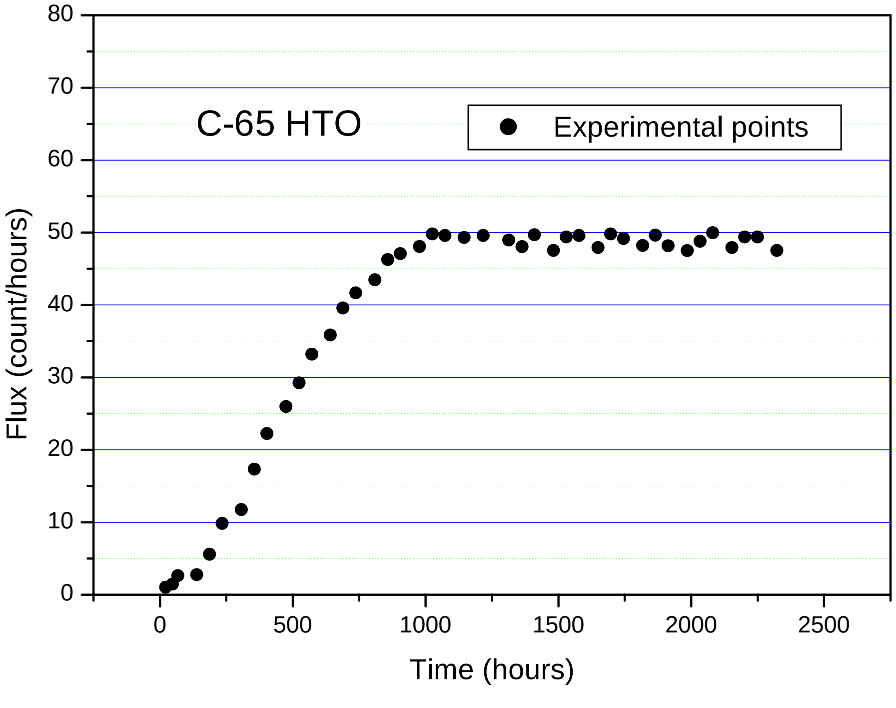

Figure 4-7: Experimental results of C-65 cell (FoCa plug ρ_d *1.37 g/cm*^{3}*, HTO): cumulative tracer recovery and linear fit in the steady-state region (up) and tracer flux entering the outlet reservoir (down).*

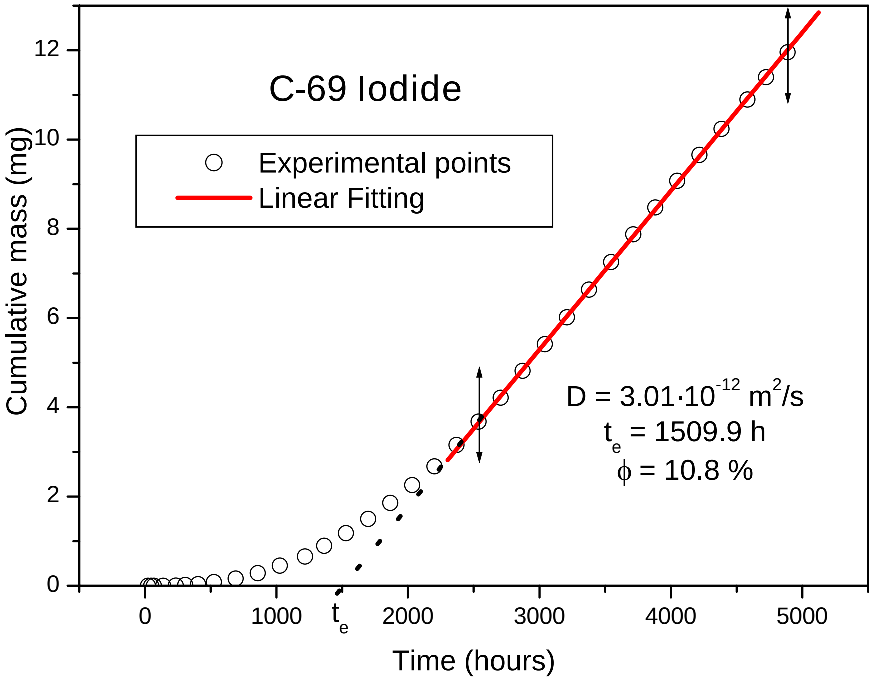

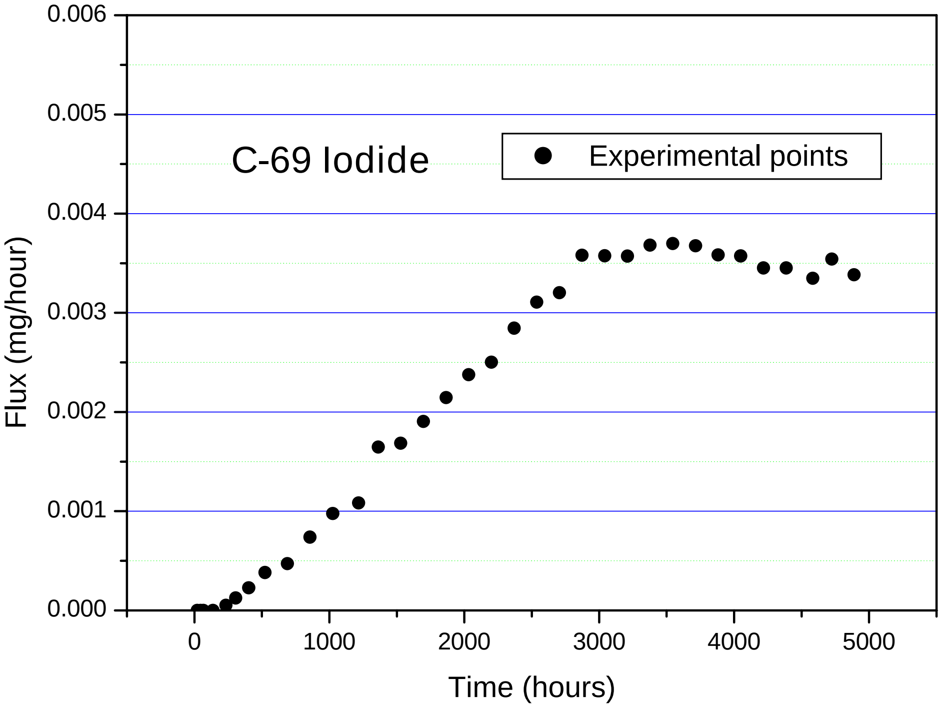

Figure 4-8: Experimental results of C-69 cell (FoCa plug ρ_d 1.34 g/cm^3, iodide): cumulative tracer recovery and linear fit in the steady-state region (up) and tracer flux entering the outlet reservoir (down).

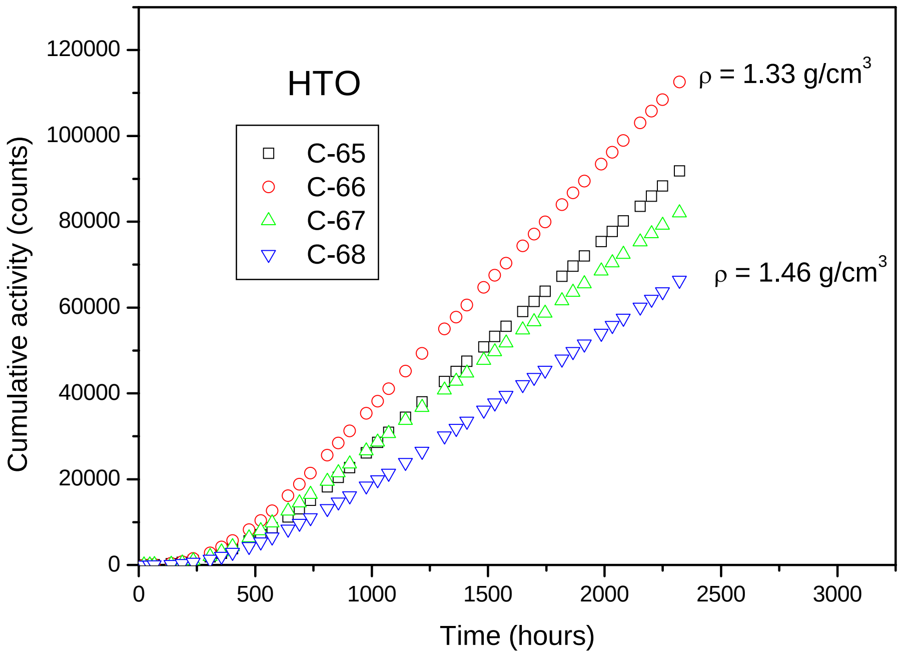

Figure 4-9: Results of the HTO experiments with powder/pellets mixture.

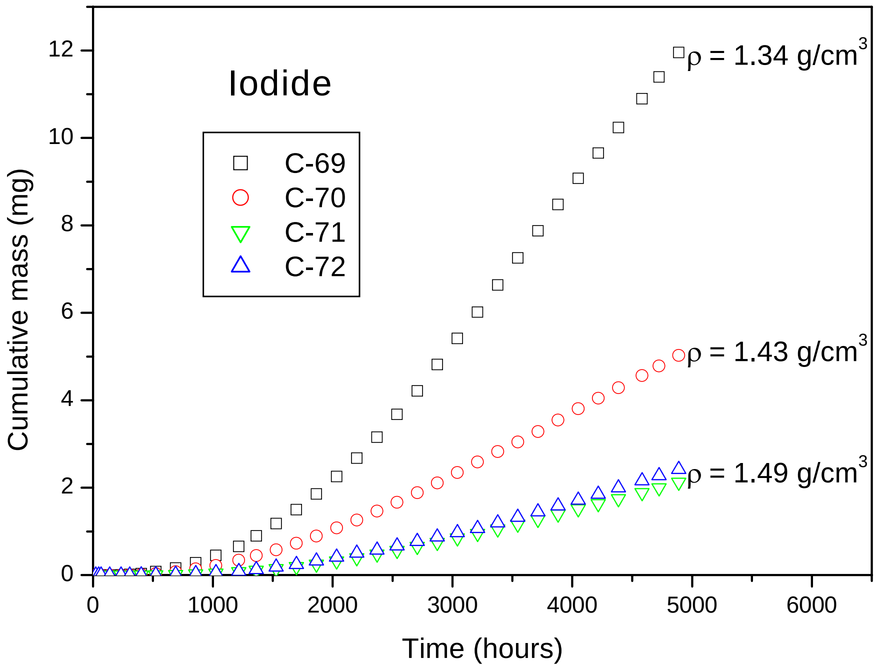

Figure 4-10: Results of the iodide experiments with powder/pellets mixture.

Table 4-3: Summary of the results obtained in the powder/pellet plugs for HTO and iodide.

Cell number and tracer used	ρ_d (g/cm^3)	D_e (m^2/s)	ϕ (%)	**Theoretical total porosity (%)**
C-65 HTO	1.37	$4.4 \cdot 10^{-11}$	46	49
C-66 HTO	1.33	$5.0 \cdot 10^{-11}$	45	50
C-67 HTO	1.43	$3.9 \cdot 10^{-11}$	28	46
C-68 HTO	1.46	$3.3 \cdot 10^{-11}$	35	45
C-75 HTO	1.41	$2.5 \cdot 10^{-11}$	46	47
C-76 HTO	1.50	$2.0 \cdot 10^{-11}$	39	44
C-69 Iodide	1.34	$3.0 \cdot 10^{-12}$	11	50
C-70 Iodide	1.43	$7.6 \cdot 10^{-13}$	3	46
C-71 Iodide	1.49	$5.8 \cdot 10^{-13}$	2	44
C-72 Iodide	1.49	$6.8 \cdot 10^{-13}$	3	44

After dismounting the cells, the specimen surface seemed to the naked eye completely homogeneous and no pellets could be distinguished (Figure 4-6). However, preferential pathways for tracer diffusion along the powder could exist if the clay sample has not become homogeneous. In order to know if the behaviour of the powder/pellet mixture differs significantly from the behaviour of the powder alone, it was necessary to perform tests with plugs made out of powder compacted at similar dry densities. Four additional diffusion experiments with HTO in clay samples of compacted powder were carried out. The results obtained for these compacted powder cells are summarised in Table 4-4 and the cumulative tracer curves obtained from these experiments are shown in Figure 4-11.

Table 4-4: Summary of the results obtained in the powder clay plugs for HTO.

Cell number	ρ_d (g/cm^3)	D_e (m^2/s)
C-99	1.25	$7.2 \cdot 10^{-11}$
C-100	1.26	$7.7 \cdot 10^{-11}$
C-101	1.38	$6.9 \cdot 10^{-11}$
C-102	1.39	$6.5 \cdot 10^{-11}$

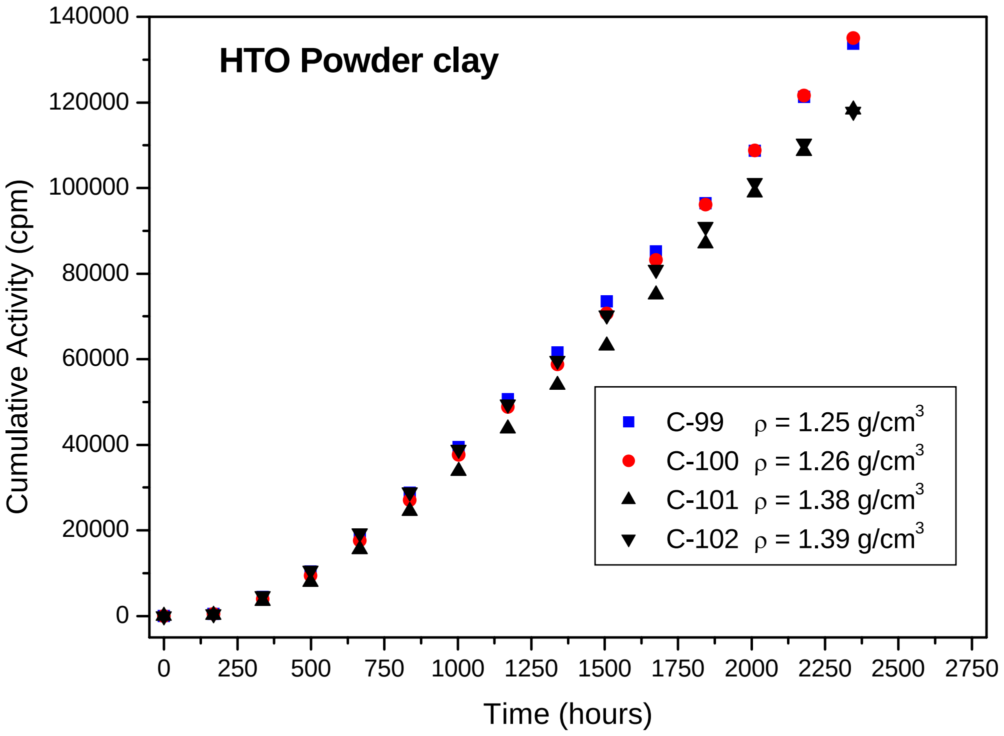

Figure 4-11: Cumulative mass recovery of HTO experiments with powder clay.

Figure 4-12 shows a summary of the effective diffusion coefficients obtained at different dry densities in both powder and powder/pellets mixtures for HTO and iodide. It can be observed that when the HTO data in the powder (circles) are compared with those of the powder/clay mixture (squares), no significant differences are appreciated and the deviations fall within the experimental error. This result indicated that, within the experimental time (three months for the hydration plus three months for the diffusion experiments), a complete homogenisation of the powder/pellets clay mixture is reached.

The effective diffusion coefficients for iodide were at least one order of magnitude lower than those for HTO for similar dry densities.

As can be seen in Figure 4-12 the effective diffusion coefficients show an exponential decrease when the clay density increases. The decrease is significantly more pronounced in the case of iodide. The experimental values can be adjusted using exponential functions of the form $D_e = A \cdot e^{-B\rho}$, where A and B are constants and ρ is the bentonite dry density.

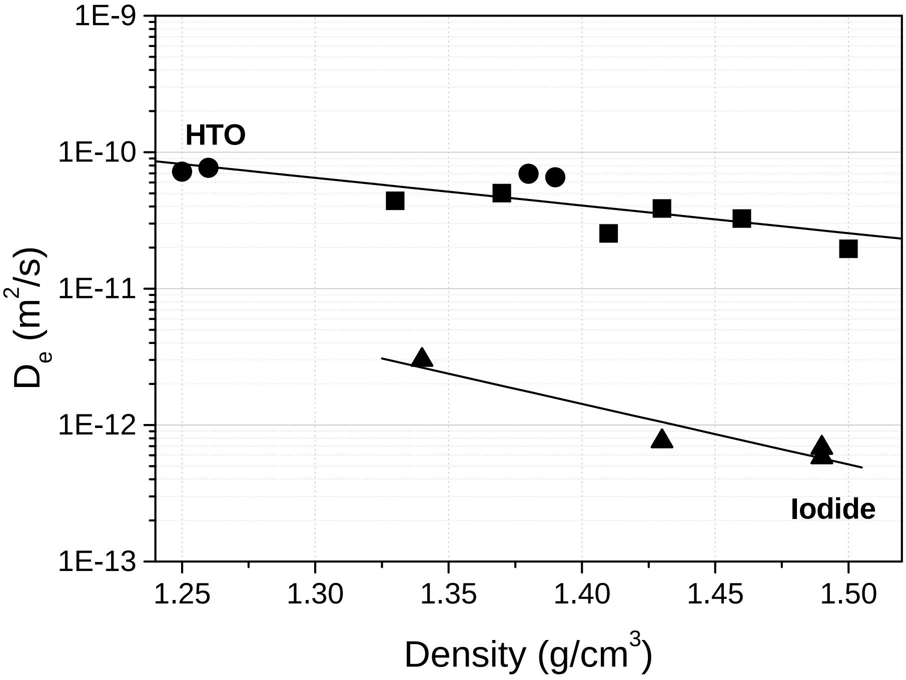

Figure 4-12: Summary of the effective diffusion coefficients obtained for HTO and iodide as a function of the dry densities of the pellets/powder mixture. The circles correspond to results obtained in compacted powder. The continuous lines correspond to the lineal fits obtained.

4.1.2.2 Accessible porosity

The accessible porosity for HTO calculated using the time-lag method presents a large range of variation with respect to the theoretical total porosity calculated considering the clay specific weight of 2.67 g/cm^3. This variation is small for cell C-75 (46 instead of 47 percent) but very large for cell C-67 (27 instead of 46 percent). It has to be remarked that in previous works it was shown that the constant gradient concentration through-diffusion method is very precise for the determination of effective diffusion coefficients, but the time-lag method is much less precise for the evaluation of the accessible porosity (García-Gutiérrez *et al.* 2000).

The constant concentration gradient method, that has been largely used because an analytical solution can be used for the determination of transport parameters, allows determining quite precisely the effective diffusion coefficient. Small variations in the slope of the tracer cumulative mass recovery *vs.* time curve, in fact, do not lead to significant changes in the calculated diffusion coefficients. On the contrary, it is very sensitive to the possible errors in the estimation of the intercept of this straight line with the time axis, and small variations can lead to very different accessible porosity estimations.

Nevertheless, it is clear that the accessible porosity values for iodide are always much smaller than those for HTO. A value of 11 percent is obtained at a density of 1.34 g/cm^3

(theoretical porosity 50 percent) and an average value of 3 percent for a density of 1.49 g/cm^3 (theoretical porosity 44 percent). This result indicates the presence of anion exclusion processes.

Since, as mentioned before, the time-lag technique is not very precise for the determination of the accessible porosity, saturation experiments were additionally carried out using HTO. In this case, the tracer diffused into the clay through both sides and the experiment continued until tracer concentration in the reservoir became constant (Figure 4-13). At the end of the experiment, the HTO concentration in the pore water was constant too, and equal to the concentration in reservoir water and this was verified when the plug was sliced and the activity in each slice measured (Figure 4-14). Table 4-5 summarises the results obtained in saturation experiments after the corrections made for the filter plates effect.

Total HTO activity in the clay sample always agreed fairly well to the theoretical values of the total porosity of the sample (± 3%). With this result it can be concluded that, for HTO, all the porosity is accessible by diffusion.

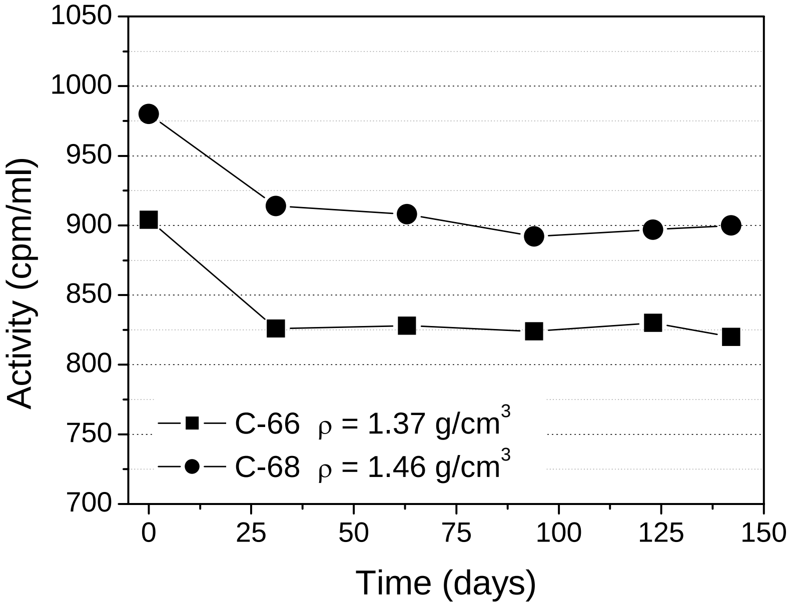

Figure 4-13: Reservoir tracer (HTO) concentration evolution during tracer saturation.

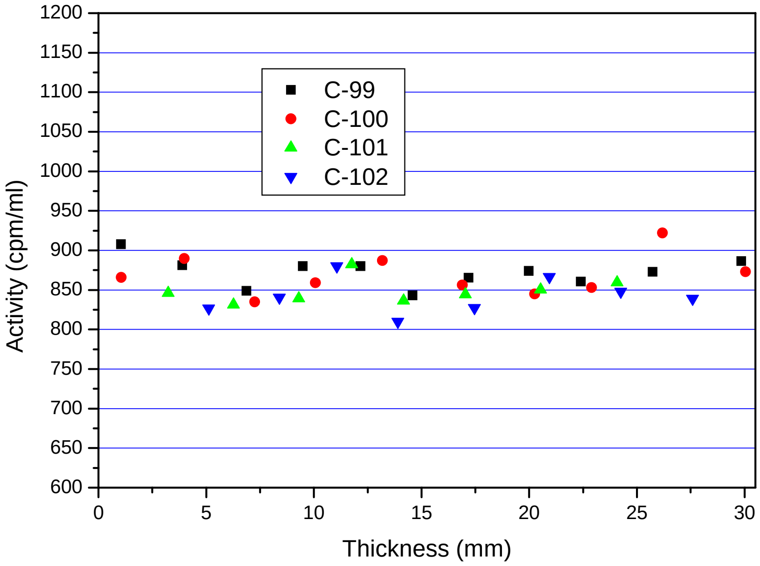

Figure 4-14: Tracer (HTO) concentration profile in the compacted clay.

Table 4-5: Summary of the results obtained in saturation experiments.

Cell reference	**HTO concentration (cpm/mL)**		**Porosity (%)**	
	Final saturation water	**Pore water**	**Accessible**	**Total**
C-66	820 ± 26	866 ± 26	51 ± 3	48
C-68	900 ± 12	913 ± 27	46 ± 2	45
C-99	818 ± 20	867 ± 28	56 ± 2	53
C-100	812 ± 24	868 ± 58	56 ± 4	53
C-101	828 ± 22	848 ± 32	49 ± 2	48
C-102	825 ± 20	841 ± 50	49 ± 3	48

4.1.2.3 The experiment with $^{36}Cl^-$

In order to demonstrate that anionic exclusion effects actually exist in the bentonite, an experiment using $^{36}Cl^-$ was also carried out. In this experiment $^{36}Cl^-$ was placed into the hydration water of initially dry, compacted FoCa clay powder (1.26 g/cm^3). The initial water content was 7.3 percent. The traced water was progressively suctioned by the clay, and after 30 days and 108 mL of water intake full saturation was reached (Figure 4-15). The initial $^{36}Cl^-$ concentration in the reservoir was 1976 cpm/mL and at the end of the experiment was 2516 cpm/mL, a 27 percent increase (Figure 4-16).

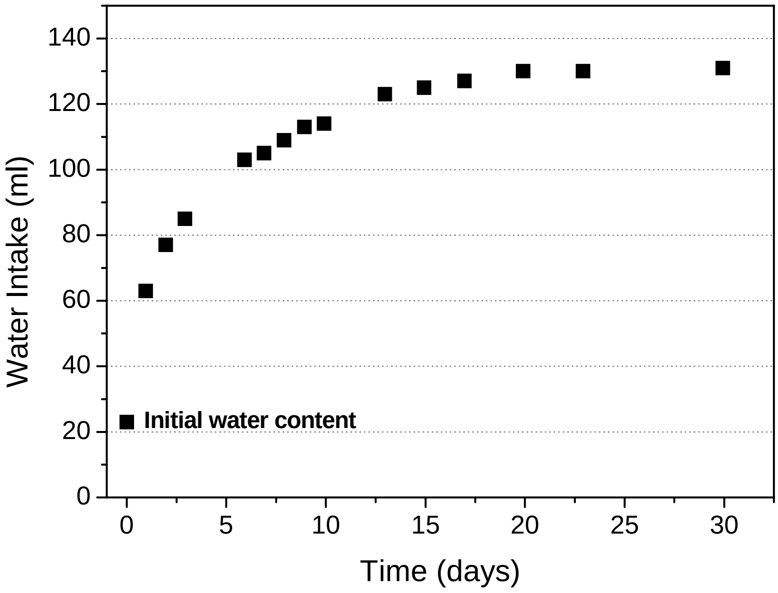

Figure 4-15: Hydration experiment with $^{36}Cl^{-}$, water intake evolution in the clay plug.

Since saturation was reached, it could be concluded that the accessible porosity for $^{36}Cl^{-}$ is less than half of the total porosity (about 24 *vs*. 50 percent). However, the diffusion accessible porosity might be even lower, in agreement with the previous diffusion experiments, because in this experiment there was a significant advection due to the suction capacity of the clay.

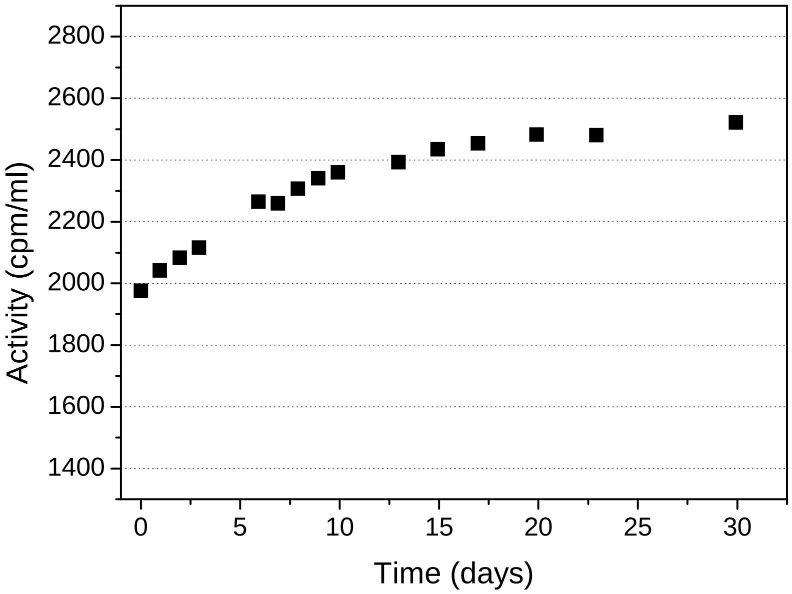

Figure 4-16: Evolution of the $^{36}Cl^{-}$ concentration in the hydration solution vs. *time.*

4.1.3 Conclusions

Effective diffusion coefficients for HTO measured in powder/pellets FoCa bentonite samples are very similar to those measured in powder FoCa samples compacted at the same density. This can be an indication that, within the experimental time of 6 months, a complete homogenisation of the powder/pellets clay mixture is reached.

Effective diffusion coefficients for HTO varied between $5.0{\cdot}10^{-11}$ and $2.0{\cdot}10^{-11}$ m^2/s decreasing with the increase of the dry density, from 1.33 to 1.50 g/cm^3. The effective diffusion coefficient for iodide is more than one order of magnitude lower than for HTO at similar densities, and varied between $3.0{\cdot}10^{-12}$ and $5.8{\cdot}10^{-13}$ m^2/s from lower to higher densities. The experimental values can be adjusted using exponential functions of the form $D_e = A{\cdot}e^{-B\rho}$, where A and B are constants and ρ is the bentonite dry density.

The values of the porosity accessible to HTO obtained by means of saturation experiments agreed satisfactorily with the total theoretical porosity of the clay for all the densities studied. The porosity accessible to HTO determined by means of through-diffusion experiments is similar to the total porosity, although the agreement is not as good as in saturation experiments, because of the high experimental variation due to the analytical approximation used (time-lag method).

The accessible porosities for iodide obtained using the time-lag method varied between 11 and 2 percent. These porosities were always clearly smaller than the accessible porosities for HTO at any density, and this is an evidence of anion exclusion of iodide in FoCa bentonite. Further evidence for anion exclusion was found in an experiment of simultaneous hydration of a bentonite sample and diffusion of $^{36}Cl^-$.

4.2 Diffusion tests by SCK·CEN

SCK·CEN has performed pulse-injection tests with a cocktail of iodide and tritium on pellets/powder mixtures compacted at dry density 1.60 g/cm^3. The modelling of the results obtained allows the calculation of the apparent diffusion coefficients and the different accessible porosities.

4.2.1 Methodology

4.2.1.1 Preparation of the clay plugs

Three stainless steel diffusion cells were prepared with clay plugs made of 50/50 powder/pellets mixture of FoCa clay compacted to a target dry density of 1.60 g/cm^3. The plugs are 5 cm high and 8 cm in diameter. The water content of the 50/50 powder/pellets mixture was determined by drying samples in an oven at 105°C for 24 hours. The average water content was 4 percent. The composition of the three FoCa mixtures used for the experiments is given in Table 4-6.

Table 4-6: Composition of the three FoCa clay plugs for migration experiments.

Test	Mass pellets (g)	Mass powder (g)
FoCa-Cel1	211.23	204.02
FoCa-Cel2	211.75	206.42
FoCa-Cel3	210.91	207.20

The inlet flange is attached to the bottom of the diffusion cell (5.5 cm in height). At the bottom of the cell a 2.5-mm thick stainless steel filter is placed (Krebsoge, 40 percent porosity). At the top-side of the cell, a piston chamber is placed. The cells are then filled in a layered fashion: first a layer of powder, followed by a layer of pellets and so on, ending with a layer of powder (similar to the procedure of CIEMAT). Then, the piston is placed into the piston chamber and the mixtures are compressed by a hydraulic press to the desired plug dimensions. Then the piston and piston chamber are removed, a second stainless steel filter is placed on top and the cell is sealed by an outlet flange. The inlet flange is equipped with stainless steel tubing with a quick connector to enable connection to a manifold containing pressurised water. The outlet flange is equipped with a stainless steel tubing and is perched through the plastic cap of a recipient to enable collection of water which percolates through the diffusion cell.

4.2.1.2 Hydration of the clay plugs

The clay plugs were hydrated with RBCW (Real Boom Clay Water, similar chemical composition as Synthetic Boom Clay water as reported by CIEMAT, but containing natural organic matter) sampled from the EG/BS piezometer in the SCK•CEN underground laboratory HADES. The diffusion cells are placed in a vertical position and the clay plugs are hydrated from the bottom.

The three cells are connected, by means of a quick connection, to a manifold which is linked to a pressure vessel containing the RBCW. All samples are therefore hydrated with the same water at the same pressure. This pressure is continuously monitored. The whole setup is placed in a temperature-controlled laboratory. Figure 4-17 gives a picture of the setup.

Figure 4-17: Overview and detail of the FoCa diffusion cells mounted on a manifold system.

At the beginning, the hydration was started with RBCW pressurized at 0.1 MPa, but immediately after connection, water breakthrough was noticed due to preferential flow through the clay plug. Therefore the pressure was decreased to 0.05 MPa. The water pressure was gradually increased to speed up the hydration until a final pressure of 1 MPa (Figure 4-18). The cell was weighed twice a day to follow the hydration and to calculate the net water uptake.

After a period of 90 days, water was expelled from the top of the clay plugs, which was taken as indication of complete hydration. The total water uptake (Figure 4-18) was about 78 mL (accounting for the dead volume of the filters and tubings at top and bottom, which is approximately 11 mL) and is slightly less than the water volume necessary to fully hydrate a clay plug of this dry density, 82.9 mL. This indicates that hydration was not fully completed yet.

The porosity of the fully hydrated plug can be calculated, using a density of the solid particles of 2.67 g/cm^3: $n = 1- \rho_d/\rho_g = 0.40$. This corresponds with a volume of 99 mL of water necessary to saturate a dry plug of 8 cm diamater and 5 cm high, or 82.9 mL to saturate a plug with an initial water content of 4 percent. This further corresponds to a water content at full saturation of 24.5 percent.

All three experiments behave exactly the same.

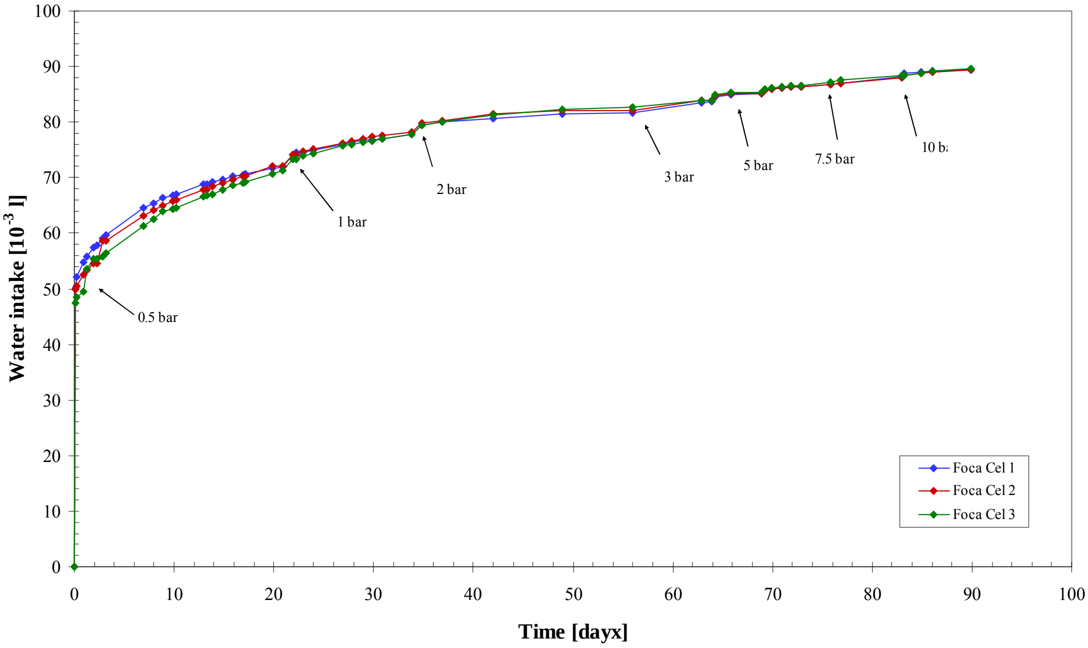

Figure 4-18: Hydration of the FoCa clay plugs prior to the diffusion test.

4.2.1.3 Percolation of the FoCa clay plugs until constant hydraulic conductivity

After hydration, the clay plugs were further conditioned by percolating Boom Clay water at 1 MPa until constant hydraulic conductivity prior to the migration experiment. Figure 4-19 gives an overview of the hydraulic conductivity before the start of the migration experiment. The fluctuations at the beginning are due to temperature changes since the experiments were moved form one temperature-controlled lab to another.

After a percolation period of ~230 days (corresponding to a percolated volume of ~45 mL of clay water) the migration experiment was started, since the hydraulic conductivity for all three cells fluctuated only between 2.2-2.4·10^{-13} m/s.

All three experiments behave exactly the same and exhibit the same and a very constant hydraulic conductivity.

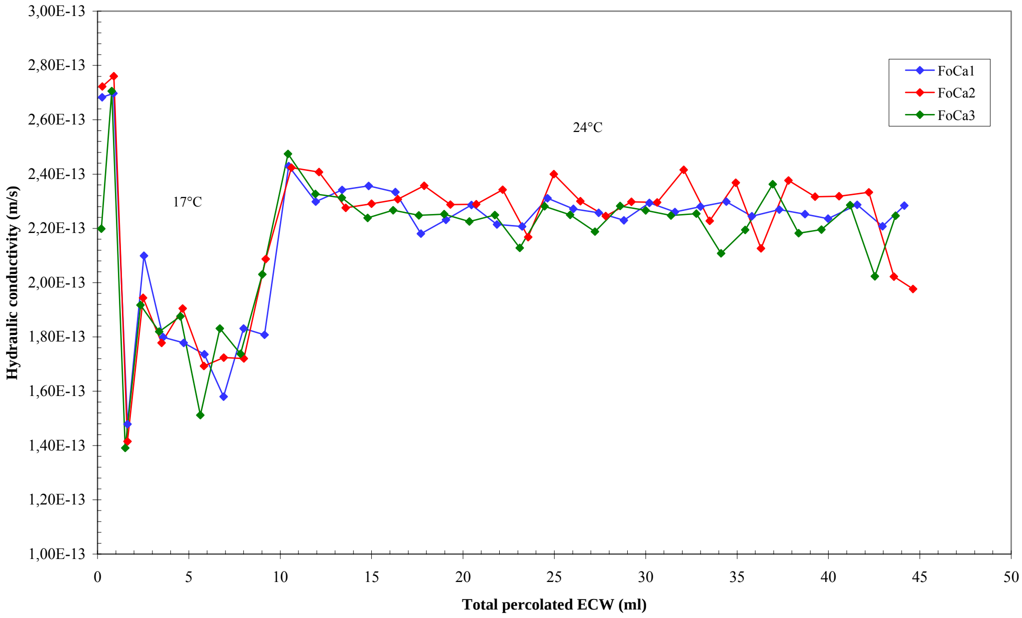

Figure 4-19: Evolution of the hydraulic conductivity for the percolation diffusion tests on FoCa plugs with dry density of 1.6 g/cm³.

4.2.1.4 Diffusion experiments: "Pulse-injection" type percolation experiments

A cocktail of H^3HO and $^{125}I^-$ was injected in three percolation/migration cells containing FoCa powder/pellet mixtures of dry density 1.60 g/cm³. The cocktail was injected in the feed water (RBCW) by means of a HPLC injection valve equipped with a 20-µL injection loop (Figure 4-20).

The initial activity injected was 5.1 10^5 Bq $^{125}I^-$ and 3.1 10^5 Bq H^3HO.

These experiments are set up in a thermostatic laboratory at 25°C, the pressure of the feed water is continuously monitored and is about 1 MPa. The water that percolates out of the clay core (approximately 0.2 mL/day) is sampled at regular time intervals and its activity is measured.

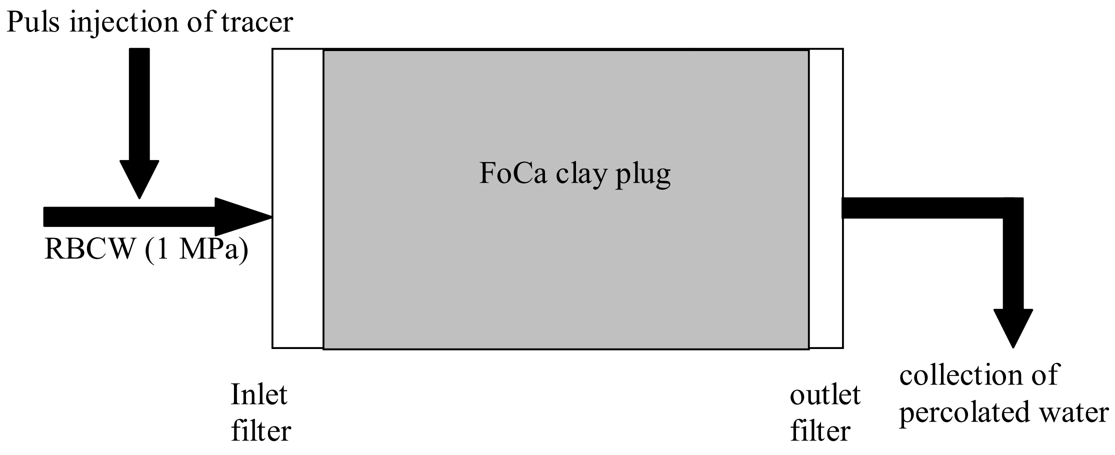

Figure 4-20: Schematic representation of a percolation diffusion setup.

The total activity due to the $^{125}I^-$ and H^3HO is determined by liquid scintillation counting. Separately, the gamma activity of the $^{125}I^-$ is determined using a NaI gamma counter. After applying corrections, the activity of both isotopes is obtained.

4.2.2 Model description

In order to derive migration parameters from the experiments, an analytical solution of the transport equation incorporated in a Fortran code is used.

4.2.2.1 Description

The behaviour of a substance diffusing in water percolated through a clay core, is described by the equation

$$\frac{\partial C}{\partial t} = D_{app}\frac{\partial^2 \mathrm{C}}{\partial \mathrm{x}^2} - V_{app}\frac{\partial C}{\partial x} \qquad [11.]$$

with D_{app} the diffusion coefficient of the substance in the pore water accessible for diffusion, V_{app} the apparent velocity of the diffusing substance, x the position, t the time and C the concentration of the diffusing substance in the pore water of the clay. The apparent velocity V_{app} is related to the Darcy velocity, V_{Darcy}, by $V_{\mathrm{Darcy}} = \eta R V_{\mathrm{app}}$ with η the diffusion accessible porosity in the clay and R the retardation coefficient. To avoid possible confusion, strictly spoken the diffusion coefficient D_{app} is an apparent hydrodynamic dispersion coefficient. It is the ratio of (a) the sum of molecular diffusion and mechanical dispersion, and (b) the retardation factor.

The configuration of the experiment we want to model is schematically shown in Figure 4-21. A clay core with length L is sandwiched between two water volumes. Each water volume has a length L_1. In an experiment, such a water volume can be the water in a very connected porous medium like a filter. Both water volumes are connected to a small tube, which allows water to flow in (at the inlet) and out (at the outlet) of the system. Both the inlet and the outlet tubes have the same cross section S_1. Due to a pressure difference, water flows from the inlet tube into the in volume.

The experiment consists on injecting a (dissolved) quantity Q_0 of the studied tracer in the in volume. The moment of injection is chosen as zero time. The injected tracer is not naturally present in the clay and in the out volume. After the injection, pure water (without tracer) flows from the inlet tube into the system. This results in the percolation and diffusion of the injected tracer through the clay. The water flowing out of the out filter is collected. The concentration of the injected tracer in the water leaving the system between time t_i and t_{i+1} is measured.

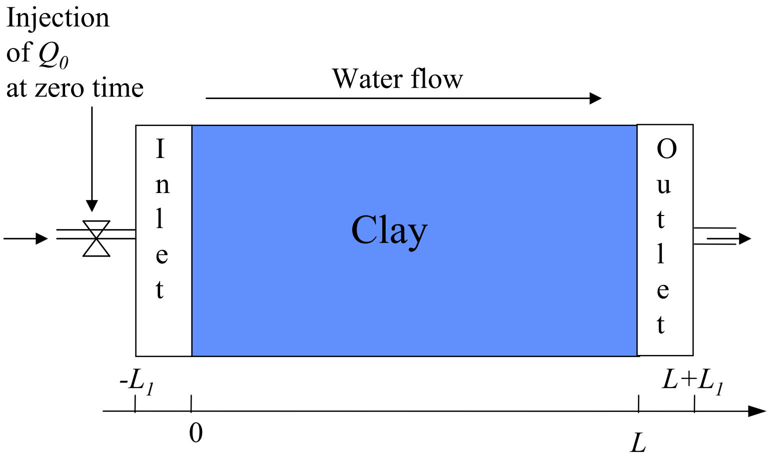

Figure 4-21: Configuration of model D2_fit and D2_fit_V2.

We now derive the boundary condition of the diffusion Equation 11 at the in volume. First, we choose an origin at the interface between the in volume and the clay core (see Figure 4-21). Since diffusion will be much faster in water than in clay, we assume that there are no concentration gradients in both (in and out) water volumes. Another approximation is that no substance will diffuse back from the in volume to the inlet tube. This approximation is especially good if the cross section (surface) S of the clay core (and thus also the in volume) is much larger than the cross section S_1 of the tubes. Indeed, since both water volumes remain unchanged, the water velocity in the tube, V_{tube}, is related to the Darcy velocity, V_{Darcy}, by:

$$S \cdot V_{\text{Darcy}} = S_1 \cdot V_{\text{tube}} \qquad [12.]$$

Thus $S >> S_1$ leads to $V_{\text{tube}} >> V_{\text{Darcy}}$, making it hard to diffuse from the in volume to the tube. The boundary condition itself is derived by expressing that the change of concentration (per unit surface) in the in volume is equal to the flux into the clay. This leads to

$$-L_1\left(\frac{\partial C}{\partial t}\right)_{x=0} = -\eta R D_{app}\left(\frac{\partial C}{\partial x}\right)_{x=0} + V_{Darcy} C(x=0) \qquad [13.]$$

with η the diffusion accessible porosity and R the retardation coefficient.

For the boundary condition at the outlet volume, we make the same assumptions as for the in volume. The change of concentration (per unit surface) in the outlet volume is equal to the difference between the flux from the clay and the flux into the outlet tube. This leads to:

$$SL_1\left(\frac{\partial C}{\partial t}\right)_{x=L} = S\left(-\eta R D_{app}\left(\frac{\partial C}{\partial x}\right)_{x=L} + V_{Darcy}C(x=L)\right) - S_1 V_{Tube} C(x=L) \qquad [14.]$$

Substituting Equation 12 in Equation 14 leads to

$$L_1\left(\frac{\partial C}{\partial t}\right)_{x=L} = -\eta R D_{app}\left(\frac{\partial C}{\partial x}\right)_{x=L} \qquad [15.]$$

The initial condition is:

$C(0 < x \leq L, t = 0) = 0$

$C(-L_1 \leq x \leq 0, t = 0) = C_0$

with the concentration C_0 given by the ratio $Q_0/(SL_1)$, where Q_0 is the injected quantity of tracer.

The solution and details on the model are given in Annex I.

4.2.2.2 Practical implementation of the model

Two fit programs (D2_fit and D2_fit_V2) use the mathematical model described in the previous section and Annex I.

Before explaining the difference between both fit programs, we first recall how the input data are gathered. Experimentally, one collects the water percolated during a time interval $(t_i, t_i+\Delta t_i)$. In this water, one measures the concentration C_i of the injected substance. The amount of percolated substance in the time interval $(t_i, t_i+\Delta t_i)$ is $\Delta Q_i = C_i \cdot V_i$ with V_i the (measured) volume of water percolated during $(t_i, t_i+\Delta t_i)$. The total percolated amount of substance between zero time and time $t_i+\Delta t_i$ is $Q_i = \sum_{j=1}^{i} \Delta Q_j$.

Both fit programs D2_fit and D2_fit_V2 use the data set (t_i, Q_i) as input data. From this data set, they try to calculate again the measured concentration C_i. It is straightforward to obtain from (t_i, Q_i) the values of Δt_i and ΔQ_i. However, because $\Delta Q_i = C_i V_i$, it is not possible to calculate C_i, unless one knows V_i. Here lies the difference between both fit programs. In D2_fit, one approximates V_i by $V_i = S\, V_{Darcy}\, \Delta t_i$, with S the outlet surface and V_{Darcy} the Darcy velocity. Averaged over all data points, this relation is exact. However due to fluctuations (*e.g.* surface tension makes water flow out in the form of small droplets), the exact and approximate values for V_i can differ considerably. Evidently, this also leads to differences between the approximated value for C_i (by $\Delta Q_i = C_i \cdot V_i$, with V_i the approximated value) and the measured value C_i. Therefore, in

D2_fit_V2, we also insert the values V_i, in the input data file, which allows recalculating the exact, experimental values for C_i.

Both fit programs D2_fit and D2_fit_V2 allow to fit (1) the total percolated quantity Q_i, or (2) the concentration C_i. When fitting the total percolated quantity, both fit programs lead to exactly the same values of the fit parameters. This is not anymore the case when one fits the concentration C_i. Here the program D2_fit_V2 should be considered more reliable. But, when the fluctuations in the flow rate are very small, both D2_fit and D2_fit_V2 will lead to nearly identical values for the fit parameters.

4.2.3 Results and discussion

The $^{125}I^-$ and H^3HO concentration profiles (activity corrected for decay and back-calculated to the time of injection) obtained from the percolating water through the FoCa plugs are followed now for more than 700 days and are given in Figure 4-22, Figure 4-23 represents the recovery for both tracers.

The reproducibility of the three FoCa plugs is remarkable. The three cells behave exactly the same.

For $^{125}I^-$ the recovery passes 100 percent, which is probably due to the increasing errors on the $^{125}I^-$ activity measurements in the tail (large correction for decay on a low measured concentration with as consequence a large relative error.)

For H^3HO a large tailing is observed and as a result, the breakthrough curve is not yet complete even after more than 700 days of percolation.

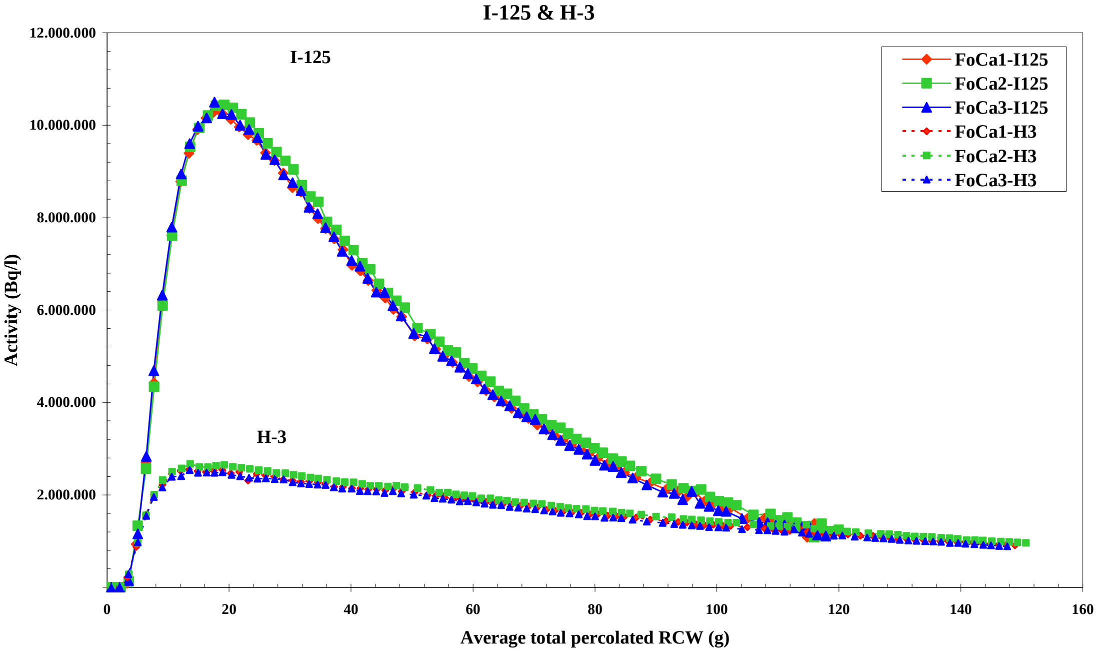

Figure 4-22: $^{125}I^-$ and H^3HO breakthrough curves for the percolation migration tests on FoCa plugs with a dry density of 1.6 g/cm³ (activity back-calculated to $t_{\text{injection}}$).

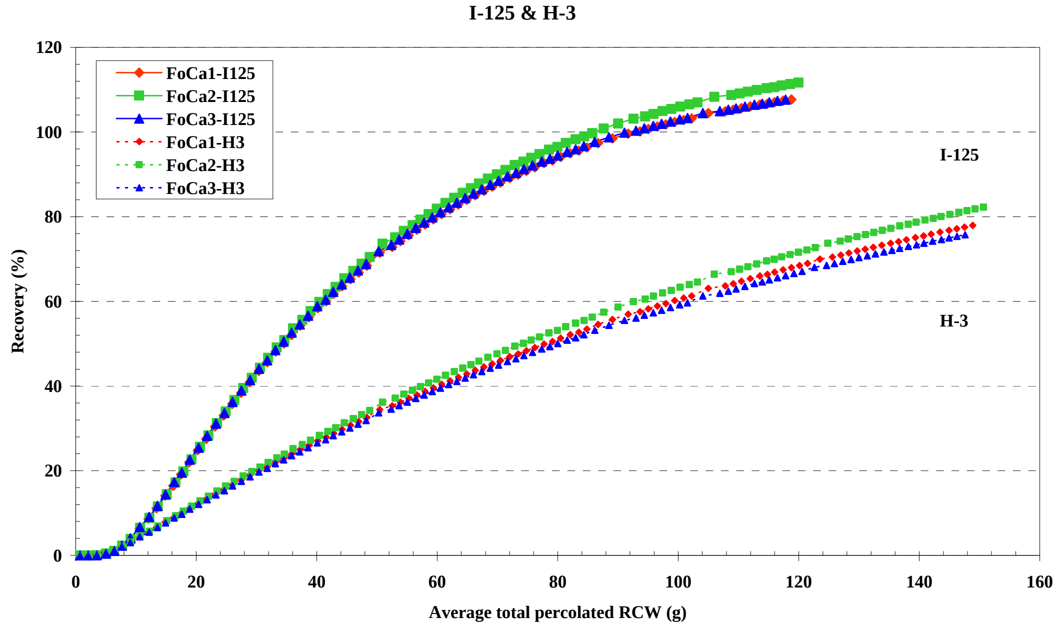

Figure 4-23: Recovery of $^{125}I^{-}$ and $H^{3}HO$ for the percolation migration tests on FoCa plugs with a dry density of 1.6 g/cm³ (activity back-calculated to $t_{injection}$).

The modelling results are shown in Figure 4-24 to Figure 4-26 and Table 4-7 and Table 4-8.

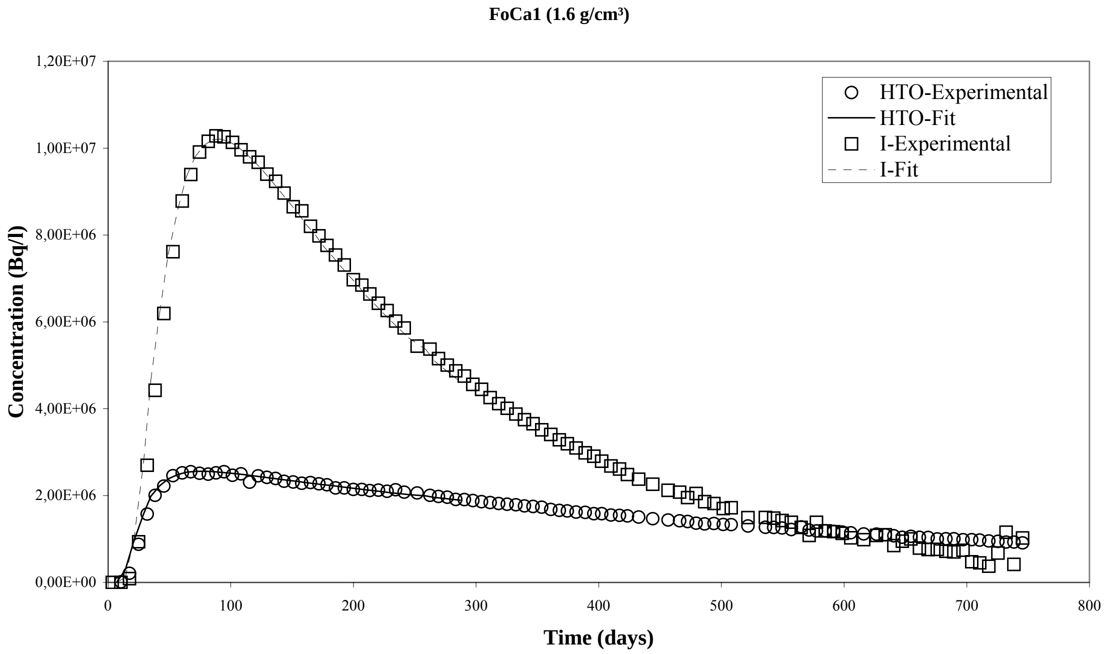

Figure 4-24: Modelled breakthrough curves for $^{125}I^{-}$ and $H^{3}HO$ for FoCa1 plug (activity back-calculated to $t_{injection}$).

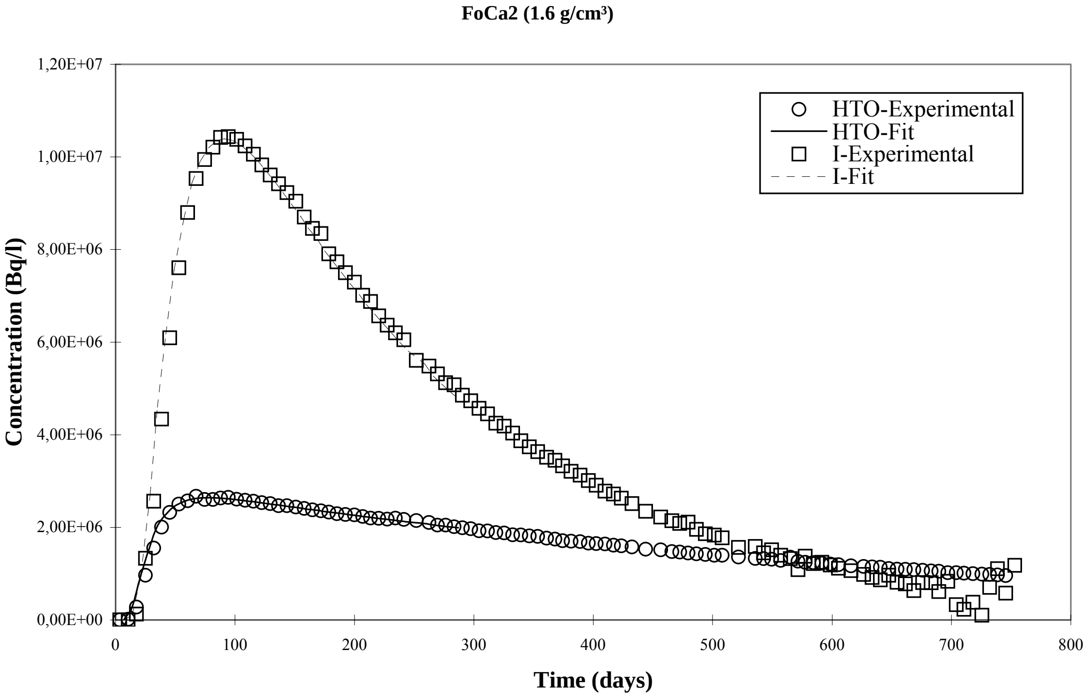

Figure 4-25: Modelled breakthrough curves for $^{125}I^-$ and H^3HO for FoCa2 plug (activity back-calculated to $t_{\text{injection}}$).

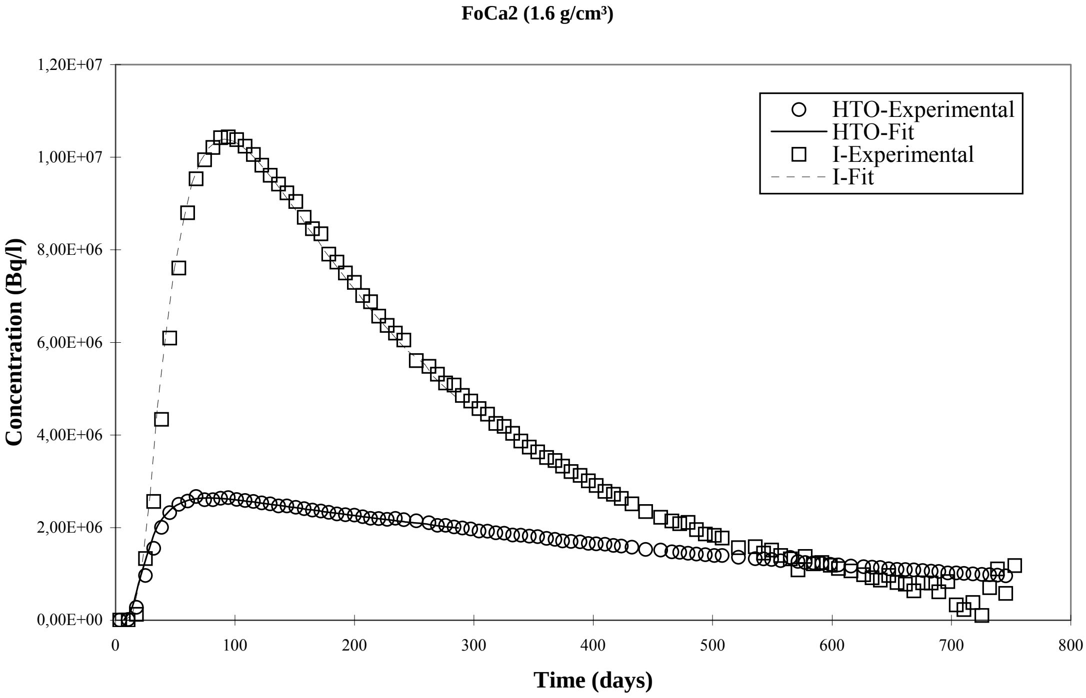

Figure 4-26: Modelled breakthrough curves for $^{125}I^-$ and H^3HO for FoCa3 plug (activity back-calculated to $t_{\text{injection}}$).

Table 4-7: Summary of the modelling parameters for tritium.

Test	**Fitted parameters**				**Derived parameter**	**Control**	**Correlation**
	D_{app} (m^2/s)	V_{app} (m/s)	Q_{tot} (Bq)	V_{darcy} (m/s)	$\eta R(=V_d/V_{app})$	Q_{inj} (Bq)	Q-V_{app}
FoCa-1	$1.97 \cdot 10^{-10}$	$9.14 \cdot 10^{-10}$	$3.64 \cdot 10^{5}$	$4.60 \cdot 10^{-10}$	0.50	$3.10 \cdot 10^{5}$	0.9992
FoCa-2	$1.93 \cdot 10^{-10}$	$8.65 \cdot 10^{-10}$	$3.98 \cdot 10^{5}$	$4.63 \cdot 10^{-10}$	0.54	$3.10 \cdot 10^{5}$	0.9944
FoCa-3	$2.01 \cdot 10^{-10}$	$8.56 \cdot 10^{-10}$	$3.73 \cdot 10^{5}$	$4.58 \cdot 10^{-10}$	0.54	$3.10 \cdot 10^{5}$	0.9944

Table 4-8: Summary of the modelling parameters for iodide.

Test	**Fitted parameters**				**Derived parameter**	**Control**	**Correlation**
	D_{app} (m^2/s)	V_{app} (m/s)	Q_{tot} (Bq)	V_{darcy} (m/s)	$\eta R(=V_d/V_{app})$	Q_{inj} (Bq)	Q
FoCa-1	$1.17 \cdot 10^{-10}$	$2.64 \cdot 10^{-9}$	$5.90 \cdot 10^{5}$	$4.60 \cdot 10^{-10}$	0.17	$5.10 \cdot 10^{5}$	0.9450
FoCa-2	$1.15 \cdot 10^{-10}$	$2.61 \cdot 10^{-9}$	$6.11 \cdot 10^{5}$	$4.63 \cdot 10^{-10}$	0.18	$5.10 \cdot 10^{5}$	0.9466
FoCa-3	$1.20 \cdot 10^{-10}$	$2.63 \cdot 10^{-9}$	$5.96 \cdot 10^{5}$	$4.58 \cdot 10^{-10}$	0.17	$5.10 \cdot 10^{5}$	0.9455

The fitting programme (D2fit-V2), fits three parameters: D_{app}, V_{app}, and Q_{tot}. From the fitted V_{app} and the experimentally measured $V_{Darcy,}$ the product ηR (porosity times retardation, but R=1 for conservative tracers) is obtained: $\eta R = V_{Darcy}/V_{app}$. And specifically, the correlation between Q and V_{app} is given.

As a control, the fitted Q_{tot} should be comparable with Q_{inj}.

Strictly spoken, the D_{app} fitted from the curve is the apparent dispersion coefficient (D^{i}_{app}), which is the sum of the apparent diffusion coefficient plus a hydrodynamic dispersion term:

$$D^{i}_{app} = D_{app} + \alpha V_{app} \qquad [16.]$$

Alpha is the dispersion length (expressed in m). However considering a dispersion length of $1 \cdot 10^{-3}$ m (which is approximately the dispersion length for Boom Clay, having a similar dry density, Maes *et al.* 1999, Aertsens *et al.* 1999). With the low V_{app} observed in the experiments, this convective term is two orders of magnitude lower than the apparent dispersion coefficient and therefore neglected.

The D_{app} is a robust parameter, but due to the high correlation between Q_{tot} and V_{app} for H^3HO, the values for ηR are less reliable. The values for ηR for H^3HO (considering H^3HO as a conservative tracer, R=1) result in very high porosities, which are higher than the calculated total porosity of 0.40.

Also the long tailing for H^3HO is very puzzling. This tailing points to a process that somehow slows down the migration, hence a retardation. As a result, the product ηR fitted from the experiment becomes higher than expected. Currently we do not know if this tailing is due to experimental artefacts, or due to a real retardation effect.

As a possible retardation mechanism, we think of isotopic exchange. If one considers that isotopic exchange is a kinetic controlled process, and if the migration of H^3HO is fast compared to the kinetics of exchange, no isotopic exchange takes place. However, if the migration of H^3HO becomes slow enough, exchange might occur. This remains a hypothesis, and we have currently no means to prove or disapprove it.

4.3 Discussion

Ranges of diffusion coefficients for iodide and H^3HO in compacted bentonites covering two orders of magnitude for comparable dry densities are reported in the literature (Yu & Neretnieks 1997, García-Gutiérrez *et al.* 2001, Kozaki *et al.* 2001, Bradbury & Baeyens 2003, Ochs *et al.* 2001). This wide range reflects the different materials used, the different ionic strengths of the background waters, the different techniques (through-diffusion, in-diffusion...), the different interpretation methods (corrections for filter plates, etc.). On average, the values obtained by SCK-CEN by the pulse-injection technique for iodide are at the high end of this range.

When comparing to parameters obtained by SCK·CEN for Boom Clay (similar tests performed on clay cores of dry density 1.7 g/cm³ sampled over the entire thickness of the Boom Formation, Aertsens *et al.* 2005) the values obtained by SCK·CEN for the FoCa mixtures are similar:

D_{app} (H^3HO in BC) = $2.3\ 10^{-10}$ m²/s

η (H^3HO in BC) = 0.37

D_{app} (I in BC) = $1.4\ 10^{-10}$ m²/s

η (I in BC) = 0.16

However, when comparing to the values obtained by CIEMAT for FoCa mixtures of lower dry densities using the through-diffusion setup, the values seem not consistent (Table 4-9).

In order to compare the values, one needs to convert the D_{app} to D_{eff} according to the following relationship:

$$\eta R D_{app} = D_{eff} \qquad [17.]$$

For both tracers $R = 1$. The problem is that, from the through-diffusion tests, the D_{eff} can be obtained as a robust parameter, but the porosities obtained by the "time-lag" method are not so robust. And as mentioned above, for the pulse-injection tests, the D_{app} is a robust parameter, but due to the high correlation between Q and V_{app}, the porosity values should be evaluated very carefully.

As can be seen, the diffusion parameter values obtained by the through-diffusion tests are systematically lower and this for lower dry densities. As a result, the values obtained by the pulse-injection technique for the higher dry densities do not fit in the exponential relationship between the D_{eff} and dry density as observed by CIEMAT. A possible explanation for this discrepancy could be the differences in the experimental methodologies employed and their sensitivity for the determination of parameters.

Table 4-9: Comparison of the obtained diffusion parameters for iodide and H^3HO on FoCa clay plugs compacted at different dry densities by different methodologies. Values in italics are calculated parameters based on the measured parameters.

	H^3HO			**Iodide**		
SCK-CEN	**D_{app}**	η	**D_{eff}**	**D_{app}**	η	**D_{eff}**
1: 1.6 g/cm^3	$1.97\cdot10^{-10}$	0.50	*$0.99\cdot10^{-10}$*	$1.17\cdot10^{-10}$	0.17	*$1.99\cdot10^{-11}$*
2: 1.6 g/cm^3	$1.93\cdot10^{-10}$	0.54	*$1.04\cdot10^{-10}$*	$1.15\cdot10^{-10}$	0.18	*$2.07\cdot10^{-11}$*
3: 1.6 g/cm^3	$2.01\cdot10^{-10}$	0.54	*$1.09\cdot10^{-10}$*	$1.20\cdot10^{-10}$	0.17	*$2.04\cdot10^{-11}$*
CIEMAT	**D_{app}**	η	**D_{eff}**	**D_{app}**	η	**D_{eff}**
1.34-1.49 g/cm^3	*$0.5\text{-}1.0\cdot10^{-10}$*	0.28-0.46	$2.0\text{-}5.0\cdot10^{-11}$	*$2.2\text{-}2.8\cdot10^{-11}$*	0.02-0.11	$0.6\text{-}3.0\cdot10^{-12}$

5 SUMMARY AND CONCLUSIONS

The laboratory work of the second phase of the RESEAL Project has aimed at the hydro-mechanical characterisation and the determination of diffusion properties of the sealing material that is being used in the shaft sealing *in situ* test performed at the HADES URF. This material is a mixture of 50/50 dry weight percent of pellets and powder of FoCa bentonite that has been compacted to various dry densities, between 1.30 and 1.60 g/cm^3.

Several techniques have been used to study the hydro-mechanical behaviour of the material upon infiltration: measurement of swelling pressure and water intake in oedometer cells; dual-gamma ray attenuation, to follow the local evolution of dry density and water content; and microfocus computer tomography, to qualitatively analyse the process of density homogenisation inside the mixture.

The combination of these techniques has allowed a better understanding of the hydration process. The pellets seem to be affected first by hydration, due to their higher suction, and this leads to a quick development of swelling pressure. The whole sample is soon involved in the process of hydration, and there is not a sharp limit between dry and wet areas. As hydration proceeds, the density of the pellets decreases, and their expansion gives place to the compaction of the powder, whose dry density increases, causing the density homogenisation. The increase of water content may produce a collapse of the macropores and a plastification of the material, translated into a diminution of the initial swelling pressure. When the degree of saturation is higher, swelling affects all the material and predominates over the collapses, for which swelling pressure increases again and reaches a stable value. In fact, the volume of micropores increases upon hydration, probably as a consequence of the collapse of the macrostructure.

The increase/decrease/increase pattern of swelling pressure development seems independent of the dry density of the material, the size of the sample and the water injection pressure. However, the kinetics of the process and the actual values of swelling pressure are affected by the boundary conditions. For example, the final swelling pressure value is higher than the initial peak for samples of high density (around 1.6 g/cm^3), whereas this is not so for samples of lower dry density. On the other hand, the same pattern has been observed in samples of compacted powder, what suggest that the process is more influenced by the microstructure of the material than by its initial fabric. As well, the initial water content of the mixture seems to have an influence on the swelling pressure development, and samples of initial high water content would develop swelling pressure in a more uniform way.

At the end of the saturation process, the mixture has become a completely homogeneous material, as shown by visual observation and by the results of the microfocus computer tomography and the dual-gamma rays attenuation. Besides, some properties determined on the saturated sample, such as the swelling pressure or the diffusion coefficients, are similar for mixtures and for samples of compacted powder.

Concerning the effective diffusion coefficients, they depend on the dry density of the material and on the kind of tracer, being lower for iodide than for tritium. The accessible porosity for tritium, a neutral and conservative tracer, is equivalent to the total porosity of the material, whereas the accessible porosities for the anionic species iodide and chloride are considerably lower, what is attributed to anion exclusion.

6 REFERENCES

Aertsens M., Put M., Dierckx A. (1999). An analytical model for pulse injection experiments. In: Feyen J., Wiyo K. (Eds.). Modelling of transport processes in soils at various scales in time and space. Int. Workshop of EurAgEng’s Field of Interest on Soil and Water. Wageningen Pers, Wageningen. 67 pp.

Aertesens, M., Dierckx A., De Cannière P., Janssen K., Moors H., Van Ravestyn L., Van Gompel M., Put M. (2005). Study of the vertical spatial variability of the transport parameters of the Boom Clay and the Neogene glauconite sands at the Mol site – Determination of the hydraulic conductivity, nR, D_{app} on Boom Clay cores and on glauconite containing sands from the Mol-1 drilling, Final report on task 2.7 for NIRAS-ONDRAF, Draft.

Alonso E.E., Gens A., Josa A. (1990). Constitutive model for partially saturated soils. Géotechnique 40: 405-430.

Angulo-Jaramillo, R. (1989). Caractérisation hydrodynamique de sols déformables partiellement saturés. Etude expérimentale à l’aide de la spectrométrie gamma double-source. PhD Thesis. Institut Polytechnique de Grenoble. (In French).

Brackley, I.J.A. (1973). Swell pressure and free swell in a compacted clay. Proc. 3rd Int. Conf. Expansive Soils. Haifa. Vol. 1: 169-179.

Bradbury, B., Baeyens, B. (2003). A comparison of apparent diffusion coefficients measured in compacted Kunigel V1 bentonite with those calculated from batch sorption measurements and De (HTO) data: a case study for Cs(I), Ni(II), Sm(III), Am(III), Zr(IV) and Np(V). PSI-Bericht 03-02, PSI, Villigen.

Crank, J. (1975). The mathematics of diffusion. 2nd ed. Clarendon Press, Oxford.

De Craen, M., Wang, L., Van Geet, M. & Moors, H. (2004). Geochemistry of Boom Clay pore water at the Mol site. SCK·CEN report BLG-990, 179 pp. Mol.

Dereeper B., Volckaert G., Imbert C., Villar M.V. (2001). Pellets/powder mixture of bentonite for backfill or sealing of HLW repositories. In: Adachi & Fukue (Eds.). Clay Science for Engineering. Balkema, Rotterdam. pp. 487-490.

García-Gutiérrez, M., Yllera, A., Mingarro, M., Fernández, V., Missana T. (2000). Cuantificación de parámetros de sorción y difusión en granitos y arcillas españoles. Informe final. CIEMAT Technical Report CIEMAT/DIAE/54231/8/99. (In Spanish).

García-Gutiérrez M., Missana T., Mingarro M., Samper J., Dai Z., Molinero J. (2001). Solute transport properties of compacted Ca-bentonite used in FEBEX project. Journal of Contaminant Hydrology 47:127-137.

Gatabin, C., Rodrigues, (1999). Projet PRACLAY, Maquette OPHELIE: Données complémentaires concernant la barriere ouvragée. Note technique SESD 99-56, CEA, Direction du Cycle du Combustible, Département d'Entreposage et de Stockage des Déchets, Service d'études d'Entreposage et de Stockage des Déchets. (In French).

Gatabin, C., Marteau, M., Imbert, C. (2000). Matériaux argileux granulaires. Etude du comportement hydro-mécanique. Rapport d'avancement 2000. NT SESD 00-37. (In French).

Hubbell, J.H. & Seltzer, S.M. (1996). Tables of X-ray mass attenuation coefficients and mass energy absorption coefficients from 1 keV to 20 MeV for elements Z=1 to 92 and 48 additional substances of dosimetric interest, NIST, Physical laboratory, Physical reference data. http://www.physics.nist.gov/PhysRefData/XrayMassCoef/cover.html

Imbert, C., Marteau, M., Gatabin, C., Vandewalle, A., Khay, M. (1999). Projet Reseal. Mise en place et compactage in situ d'un matériau argileux hétérogène pour la réalisation d'un scellement de puits. Propriétés hydro-mécaniques de ce matériau déterminées en laboratoire. NT SESD 99-69. (In French).

Imbert, C., Billaud, P., Touzé, G. (2004). Caractérisation hydro-mécanique du matériau argileux utilisé dans l'essai de scellement de puits à échelle un « RESEAL ». Project européen « RESEAL Phase 2 ». Rapport final. Rapport Technique DPC/SCCME 04-694-A. Gif-sur-Yvette. 69 pp. (In French).

Joseph, P.M. (1981). Artifacts in computed tomography. In: Newton, T.H., Potts, D.G. (Eds.). Radiology of the skull and brain: Technical aspects of computed tomography. Vol. 5. The C.V. Mosby Company, St.-Louis (Ill): 4058-4095.

Komine, H., Ogata, N. (1994). Experimental study on swelling characteristics of compacted bentonite. Can. Geotech. J. 31: 478-490.

Kozaki, T., Inada, K., Sato, S., Oaci, H. (2001). Diffusion mechanism of chloride ions in sodium montmorillonite. J. Contaminant Hydrology 47: 159-170.

Maes, N., Moors, H., Dierckx, A., De Cannière, P., Put, M. (1999). The assessment of electromigration as a new technique to study diffusion of radionuclides in clayey soils. J. Contaminant Hydrology 36: 231-247.

Marcial, D. (2003). Comportement hydromécanique et microstructural des matériaux de barrière ouvragée. PhD Thesis. École Nationale des Ponts et Chausées, Paris. 316 pp. (In French).

Moutier M. (1996). Hydrodynamic properties of unsaturated porous media as affected by clay dispersion and migration induced by water quality. Thèse de Doctorat en sciences agronomiques et ingéniérie biologique, Louvain-la-Neuve. (In French).

Ochs, M., Lothenbach, B., Wanner, H., Sato, H., Yui, M. (2001). An integrated sorption–diffusion model for the calculation of consistent distribution and diffusion coefficients in compacted bentonite. J. Contaminant Hydrology 47: 283-296.

Pasquiou, A. (1999). Pellets d'argile : élaboration et caractérisation Thermo_Hydro-Mécanique. Deuxième rapport d'avancement de thèse. Rapport ANDRA C RP AMAT 99.077. (In French).

Pasquiou, A. (2001). Pellets d'argiles gonflantes. Elaboration et caractérisation hydro-mécanique. PhD Thesis. Université des Sciences et Techniques de Lille. (In French).

Roels, S., Vandersteen, K., Carmeliet, J. (2002). Measuring and simulating moisture uptake in a fractured porous medium. Advances in Water Resources 26: 237-246.

Rolland S. (2002). Transfert hydrique dans des sols argileux gonflants : Influence du confinement. Thèse de Doctorat en mécanique et énergétique. Institut Polytechnique de Lorraine. (In French).

Sato, H., Ashida, T., Kohara, Y., Yui, M., (1993). Study on retardation mechanism on ^{3}H, ^{99}Tc, ^{137}Cs, ^{237}Np and ^{241}Am in compacted sodium bentonite. Scientific Basis for Nuclear Waste Management XVI. Mat. Res. Soc. Symp. Proc. 294: 403-408.

Sing, K.S.W., Everett, D.H., Haul, R.A.W., Moscou, L., Pierotti, R.A., Rouquérol, J., Siemieniewska, T. (1985). Reporting physisorption data for gas/solid systems with special reference to the determination of surface area and porosity. Pure & Appl. Chem. 57(4): 603-619. IUPAC.

Van Geet, M. (2001). Optimisation of microfocus X-ray computer tomography for geological research with special emphasis on coal components (macerals) and fractures (cleats) characterisation. PhD Thesis. K.U.Leuven, Faculteit Wetenschappen, Departement Geografie-Geologie, Leuven, Belgium, 203 pp.

Van Geet, M., Swennen, R. (2001). Quantitative 3D-fracture analysis by means of microfocus X-ray computer tomography (μCT): an example from coal. Geophysical Research Letters 28(17): 3333-3336.

Van Geet, M., Swennen, R., Wevers, M. (2000). Quantitative analysis of reservoir rocks by means of microfocus X-ray computer tomography. Sedimentary Geology 132: 25-36.

Van Geet, M., Volckaert, G., Roels, S. (2005). The use of microfocus X-ray computed tomography in characterising the hydration of a clay pellet/powder mixture. Aplied Clay Science 29(2): 73-87.

Villar, M.V. (2000). Caracterización termo-hidro-mecánica de una bentonita de Cabo de Gata. PhD Thesis, Universidad Complutense de Madrid, Madrid. 396 pp. (In Spanish).

Villar, M.V. (2002). Thermo-hydro-mechanical characterisation of a bentonite from Cabo de Gata. A study applied to the use of bentonite as sealing material in high level radioactive waste repositories. Publicación Técnica ENRESA 01/2002. 258 pp. Madrid.

Villar, M.V., Lloret, A. (2004). Influence of temperature on the hydro-mechanical behaviour of a compacted bentonite. Applied Clay Science 26: 337-350.

Volckaert, G., Dereeper, B., Put, M., Ortiz, L., Gens, A., Vaunat, J., Villar, M.V., Martín, P.L., Imbert, C., Lassabatère, T., Mouche, E., Cany, F. (2000). A large-scale in situ demonstration test for repository sealing in an argillaceous host rock. Reseal project – Phase I. *EUR* 19612. Commission of the European Communities. 273 pp. Luxembourg.

Yu, J.-W., Neretnieks, I. (1997). Diffusion and sorption properties of radionuclides in compacted bentonite. SKB Technical Report 97-12, SKB, Stockholm, Sweden.

Annex 1

Solution of the model

The problem can be solved by using the inverse Laplace method. The calculations are given in the next section. Here, we only present the final solution, which is in general (in the following text, the subscript *app* for V_{app} and D_{app} were omitted to simplify the writing))

$$C(x,t) = 2C_0 \exp\left(\frac{V}{2D}x - \frac{V^2}{4D}t\right)\left(\sum_n S_n(x,t) + \sum_m T_m(x,t)\right) \tag{1}$$

with

$$S_n(x,t) = \frac{\alpha_n^* \left(\alpha_n^* \cos(\alpha_n x) + \left(g(z) - \alpha_n^{*2}\right)\sin(\alpha_n x)\right) \exp\left(-\alpha_n^2 Dt\right)}{L_{eff}\,\alpha_n^{*4} + \alpha_n^{*2}\left(L_{eff}\left(1 - 2g(z)\right) + 2\right) + g(z)\left(2 + g(z)L_{eff}\right)} \tag{2}$$

where

$$z = \frac{VL_1}{\eta RD} \tag{3}$$

$$g(z) = \frac{z}{4}(2 - z) \tag{4}$$

$$L_{eff} = \frac{\eta RL}{L_1} \tag{5}$$

$$\alpha_n = \frac{\eta R \alpha_n^*}{L_1} \tag{6}$$

and α_n^* the positive zeros ($\alpha_n^* > 0$) of

$$tg\left(\alpha_n^* L_{eff}\right) = \frac{-2\left(g(z) - \alpha_n^{*2}\right)\alpha_n^*}{\left(\alpha_n^{*2} - g(z)\right)^2 - \alpha_n^{*2}} \tag{7}$$

The term *$T_m(x,t)$* in (14) can be considered as an imaginary analogue of (8):

$$T_m(x,t) = -\frac{q_m^* \left(q_m^* \cosh(q_m x) + \left(g(z) + q_m^{*2}\right)\sinh(q_m x)\right) \exp\left(q_m^2 Dt\right)}{L_{eff}\,q_m^{*4} - q_m^{*2}\left(L_{eff}\left(1 - 2g(z)\right) + 2\right) + g(z)\left(2 + g(z)L_{eff}\right)} \tag{8}$$

where

$$q_m = \frac{\eta R q_m^*}{L_1} \tag{9}$$

and q_m^* the positive zeros ($q_m^* > 0$) of

$$\tanh\left(q_m^* L_{eff}\right) = \frac{-2\left(g(z)+q_m^{*2}\right)q_m^*}{\left(q_m^{*2}+g(z)\right)^2+q_m^{*2}} \tag{10}$$

Finally, the solution (7) is not valid for the special cases $z = 0$ and $z = 2$ (see section 1.5.3).

The expression (7) allows calculating the concentration of the tracer in the outlet filter at time t. Experimentally the average concentration in the water flowing out of the system is measured, between a time t_i, where water starts collecting, and time t_{i+1}, where water stops collecting. Assuming that the concentration at the exit of the outlet tube is the same as the concentration in the outlet filter (which seems a reasonable assumption for small, thin outlet tubes), this average concentration is given by

$$C_{av}\left(x = L, t_i, t_{i+1}\right) = \frac{\int_{t_i}^{t_{i+1}} C(x = L, t)\, dt}{t_{i+1} - t_i} \tag{11}$$

Substituting expression (7) in (17) leads after a simple integration to the average concentration $C_{av}(L, t_i, t_{i+1})$.

A similar integration allows calculating the quantity of substance $Q(t)$ that has percolated out of the outlet filter

$$Q(t) = S\, V_{Darcy} \int_0^t C(x = L, t')\, dt' \tag{12}$$

Details of the calculation

For finding the solution of the diffusion-advection equation (1), we use the substitution

$$C(x,t) = F(x,t)\exp(\alpha x - \beta t) \tag{13}$$

with

$$\alpha = \frac{V}{2D} \qquad \beta = \frac{V^2}{4D} \tag{14}$$

In this way, the diffusion-advection equation (1) reduces to

$$\frac{\partial F}{\partial t} = D\frac{\partial^2 F}{\partial \mathrm{x}^2} \tag{15}$$

Similarly, the boundary conditions (3) and (5) are transformed into expressions for $F(x,t)$ instead of $C(x,t)$:

$$\left(\frac{\partial F}{\partial t}\right)_{x=0} - \frac{\eta RD}{L_1}\left(\frac{\partial F}{\partial x}\right)_{x=0} = \left(\beta - \frac{V_{Darcy}}{2L_1}\right)F(x=0) \qquad (16)$$

$$\left(\frac{\partial F}{\partial t}\right)_{x=L} + \frac{\eta RD}{L_1}\left(\frac{\partial F}{\partial x}\right)_{x=L} = \left(\beta - \frac{V_{Darcy}}{2L_1}\right)F(x=L) \qquad (17)$$

The similar transformation for the initial condition (6) is trivial.

The Laplace transform of (21), taking into account the initial condition (6), is

$$\frac{\partial^2 \overline{F}}{\partial \mathrm{x}^2} - q^2\,\overline{F} = 0 \qquad (18)$$

with $\overline{F(x,p)}$ the Laplace transform of $F(x,t)$ and

$$q^2 = \frac{p}{D} \qquad (19)$$

The solution of the differential equation (24) is

$$\overline{F} = A\cosh(qx) + B\sinh(qx) \qquad (20)$$

where the integration constants A and B are determined by substituting the Laplace transforms of the boundary conditions (22) and (23) in (26). This leads to

$$\overline{F} = \frac{f(p)}{g(p)} \qquad (21)$$

with

$$f(p) = C_0\,\frac{L_1^2}{(\eta R)^2\,D}\left(q_*\cosh\big(q(L-x)\big) + \left(g(z)+q_*^2\right)\sinh\big(q(L-x)\big)\right) \qquad (22)$$

$$g_p(p) = 2\left(g(z)+q_*^2\right)q_*\cosh(qL) + \left(q_*^2 + \left(g(z)+q_*^2\right)^2\right)\sinh(qL) \qquad (23)$$

where the notations (9-10) are used as well as

$$q = \frac{\eta R q_*}{L_1} \qquad (24)$$

According to Crank (1975), the inverse Laplace transform of $\overline{F}$ is

$$F = \sum_n \frac{f(p_n)}{g_p{}'(p_n)}\exp(p_n\,t) \qquad (25)$$

where the sum goes over all zeros p_n of the function $g_p(p)$ and $g_p{}'(p_n)$ denotes the value of $dg_p(p)/dp$ in a zero p_n. This solution is only valid when both functions $f(p)$ and $g_p(p)$ do not have common factors. If $g(z) = 0$, both functions $f(p)$ and $g_p(p)$ have the common factor q^*. This special case will be handled later.

If $g(z) \neq 0$, the function $g_p(p)$ has two types of zeros: (A) zeros corresponding to (non-zero) positive p-values (and thus real q-values, see (25)), and (B) zeros corresponding to (non-zero) negative p-values (and thus imaginary q-values). This explains why the solution (7), which is obtained by the substitution of the solution (31) in (19) consists of two terms (see also the corresponding expressions for the zeros: eq. (13) and eq. (16)).

Since the details of the calculations for both terms are similar, further results are only mentioned for negative p-values (where the notation $q_n = i\,\alpha_n$ is used, see also (11-12)). The expressions (28) and (29) lead to

$$\frac{f(p_n)}{g_p'(p_n)} = \frac{2C_0\alpha_n^*\left(\alpha_n^{*2} + \left(g(z)-\alpha_n^{*2}\right)^2\right)\left(\alpha_n^*\cos(\alpha_n x) + \left(g(z)-\alpha_n^{*2}\right)\sin(\alpha_n x)\right)}{L_{eff}\,\alpha_n^{*8} - \alpha_n^{*6}\left(-2L_{eff} + 2L_{eff}\,g(z) - 2\right) + \alpha_n^{*4}\left(6g(z)^2 L_{eff} - 4g(z)L_{eff} - 2g(z) + 2 + L_{eff}\right) - \ldots}$$

$$\overline{\ldots - \alpha_n^{*2} g(z)\left(4g(z)^2 L_{eff} - 2g(z)L_{eff} + 2g(z) - 2\right) + g(z)^3\left(2 + g(z)L_{eff}\right)} \qquad (26)$$

The elimination of the common factor $\left(\alpha_n^{*2} + \left(g(z)-\alpha_n^{*2}\right)^2\right)$ in both the numerator and the denominator of (32) leads to (8).

For the special case $g(z) = 0$ (which occurs when $z = 0$ or $z = 2$), the function $g_p(p)$ has not only zeros corresponding to non-zero positive or negative p-values, but also a zero at $p = q = 0$. A series expansion for $p_n \rightarrow 0$ leads to the corresponding term in (31): $f(p_n)/\, g_p'(p_n) = C_0/(2+L_{eff})$. Because for $g(z) = 0$, there are no solutions to (16), the expression (7) is then given by

$$C(x,t) = 2C_0 \exp\left(\frac{V}{2D}x - \frac{V^2}{4D}t\right)\left(\sum_n S_n(x,t) + \frac{1}{2\left(2+L_{eff}\right)}\right) \qquad (27)$$

For $z = V = 0$, the present model does not describe a pulse injection experiment but a through diffusion experiment.

Note also that for $0 < z < 2$, the solution (7) never contains any T_n terms. Indeed, since in that interval the function $g(z)$ is positive, the expression in the right hand side of (16) is always negative. So, equation (16) does not have any solution, which means that there are no T_n terms in (7).